

AD-A218 516

ELECTED

EB 26 1990

2b. DECLASSIFICATION/DOWNGRADING SCHEDULE

4. PERFORMING ORGANIZATION REPORT NUMBER(S)

B
RF 4472396a. NAME OF PERFORMING ORGANIZATION
Department of Mech Eng.
The City College of NY6b. OFFICE SYMBOL
(if applicable)

6c. ADDRESS (City, State, and ZIP Code)

138th Street & Convent Ave.
New York, N.Y. 10031

1b. RESTRICTIVE MARKINGS

3. DISTRIBUTION/AVAILABILITY OF REPORT

Unrestricted

5. MONITORING ORGANIZATION REPORT NUMBER(S)

AFOSR - TR. 90-0209

7a. NAME OF MONITORING ORGANIZATION

AFOSR/NA

7b. ADDRESS (City, State, and ZIP Code)

Building 410
Bolling AFB DC 20332-6448

8a. NAME OF FUNDING/SPONSORING

AFOSR/NA
Bolling AFB DC 20332-64488b. OFFICE SYMBOL
(if applicable)

NA

9. PROCUREMENT INSTRUMENT IDENTIFICATION NUMBER

AFOSR-87-0288

8c. ADDRESS (City, State, and ZIP Code)

Building 410
Bolling AFB DC 20332-6448

10. SOURCE OF FUNDING NUMBERS

PROGRAM ELEMENT NO.	PROJECT NO.	TASK NO	WORK UNIT ACCESSION NO.
61102F	2302	B2	

11. TITLE (Include Security Classification)

Microcracking & Toughness of Ceramic-Fiber/Ceramic-Matrix Composites Under High Temperature (U)

12. PERSONAL AUTHOR(S)

Delale, Feridun & Liaw, Been-Ming

13a. TYPE OF REPORT

Scientific

13b. TIME COVERED

FROM 8/1/87 TO 9/30/89

14. DATE OF REPORT (Year, Month, Day)

89/12/1

15. PAGE COUNT

86

16. SUPPLEMENTARY NOTATION

17. COSATI CODES

FIELD	GROUP	SUB-GROUP

18. SUBJECT TERMS (Continue on reverse if necessary and identify by block number)

Composites, Ceramic, Fracture, High Temperature,
Microcracking, Materials, Fibers

19. ABSTRACT (Continue on reverse if necessary and identify by block number)

Silicon Carbide

This report contains the results of the research project entitled:

"Microcracking and Toughness of Ceramic-Fiber/Ceramic-Matrix Composites Under High Temperature" supported by the AFOSR. Microcracking mechanisms and toughness of Nicalon (SiC)/SiC composite at elevated temperature are studied analytically and experimentally. First the fiber distribution patterns in the ceramic composite are determined by observing the specimens

cont.

on back
(CONT'D)

20. DISTRIBUTION/AVAILABILITY OF ABSTRACT

 UNCLASSIFIED/UNLIMITED SAME AS RPT DTIC USERS

21. ABSTRACT SECURITY CLASSIFICATION

UNCLASSIFIED

22a. NAME OF RESPONSIBLE INDIVIDUAL

George K. Haritos, Lt Col, USAF

22b. TELEPHONE (Include Area Code)

(202) 767-0463

22c. OFFICE SYMBOL

NA

DISTRIBUTION STATEMENT A

Approved for public release
Distribution Unlimited

under optical and scanning electron microscopes. Thus the effect of fibers and fiber interactions on the microcrack propagation are investigated analytically through the single-fiber, the two-fiber, and the ring models. Monolithic SiC specimens are tested under varying temperature to determine the effect of temperature on the toughness of the matrix material. The Nicalon/SiC composite specimens are then tested at various temperatures. The combined effect of temperature and fibers on the toughness of the matrix is expressed by introducing the concept of "apparent fracture toughness". The experimental results indicate that for the Nicalon /SiC composite the "apparent fracture toughness" decreases with local volume fraction of fibers v_f and temperature. An analytical model to predict this behavior is developed and used in the analysis of the experimental data. Finally, recognizing the importance of the fiber/matrix interface on the overall toughness and strength of the material, an experimental/analytical technique is developed to determine the interfacial shear strength.

v_f (volume fraction)
← can't put 18.1 et al's

MICROCRACKING AND TOUGHNESS OF
CERAMIC-FIBER/CERAMIC-MATRIX COMPOSITES
UNDER HIGH TEMPERATURE



THE CITY COLLEGE OF
THE CITY UNIVERSITY of NEW YORK

90 02 23 034

FINAL REPORT FOR THE PROJECT ENTITLED

**MICROCRACKING AND TOUGHNESS OF
CERAMIC-FIBER/CERAMIC-MATRIX COMPOSITES
UNDER HIGH TEMPERATURE**

Principal Investigators:

Dr. F. Delale and Dr. B. M. Liaw
The City College of The City University of New York
Department of Mechanical Engineering
New York, NY 10031

Project Manager:

Dr. George K. Haritos, Lieutenant Colonel, USAF

**Sponsored by: AFOSR
Grant No. AFOSR-87-0288**

December 1989

ABSTRACT

This report contains the results of the research project entitled: "Microcracking and Toughness of Ceramic-Fiber/Ceramic-Matrix Composites Under High Temperature" supported by the AFOSR. Microcracking mechanisms and toughness of Nicalon (SiC)/SiC composite at elevated temperature are studied analytically and experimentally. First the fiber distribution patterns in the ceramic composite are determined by observing the specimens under optical and scanning electron microscopes. Thus the effect of fibers and fiber interactions on the microcrack propagation are investigated analytically through the single-fiber, the two-fiber, and the ring models. Monolithic SiC specimens are tested under varying temperature to determine the effect of temperature on the toughness of the matrix material. The Nicalon/SiC composite specimens are then tested at various temperatures. The combined effect of temperature and fibers on the toughness of the matrix is expressed by introducing the concept of "apparent fracture toughness". The experimental results indicate that for the Nicalon /SiC composite the "apparent fracture toughness" decreases with local volume fraction of fibers V_f and temperature. An analytical model to predict this behavior is developed and used in the analysis of the experimental data. Finally, recognizing the importance of the fiber/matrix interface on the overall toughness and strength of the material, an experimental/analytical technique is developed to determine the interfacial shear strength.

Accession For	
NTIS GRA&I <input checked="" type="checkbox"/>	
DTIC TAB <input type="checkbox"/>	
Unannounced <input type="checkbox"/>	
Justification _____	
By _____	
Distribution/	
Availability Codes	
Dist	Avail and/or Special
A-1	

REF ID: A65267

COPY REQUESTED

DTIC

A-1

TABLE OF CONTENTS

1.	Introduction	3
2.	The Material: Nicalon/SiC Composite	4
3.	The Theoretical Studies	6
	(a) The single-fiber model	6
	(b) Interaction of two fibers	15
	(c) The ring model	18
4.	Experimental Work	21
	(a) The experimental set-up	22
	(b) Effect of temperature on toughness of matrix material ..	22
	(c) Effect of fibers and temperature on the "apparent toughness" of the matrix	23
	(d) Determination of interfacial strength and interfacial stresses	25
5.	Theoretical Prediction and Comparison with Experimental Results .	28
6.	References	29
7.	Figures and Tables	33
	APPENDIX: Paper Presented at the ASME 1989 WAM	

1. Introduction

As is well known ceramic matrix composites have recently attracted a great deal of attention due to the promise they hold for developing high-temperature resistant materials with high toughness. Up to now the structural applications of ceramics and ceramic composites have been limited because of the fact that their brittleness makes them an unlikely candidate in applications where high toughness is required. But the combination of advanced manufacturing techniques and new ceramic composites appears to satisfy both conditions of resistance to high-temperature oxidation and high toughness. The current study focuses on one such material, namely, Nicalon/SiC composite manufactured by Amercom, Inc., Chatsworth, CA.

It has long been recognized that the low toughness of ceramics results from the presence of microcracks or voids in the material. These microcracks may develop due to inclusions, thermal expansion mismatch, phase transformation, or thermal expansion anisotropy. Whatever the initial agent, under sustained mechanical and/or thermal loading, these microcracks may coalesce into a critical flaw, causing the failure of the material. In fiber reinforced ceramic composites the failure mechanism is much more complicated because of the presence of fibers. For example, under uniaxial tension fiber matrix microcracks may appear. At sustained loading these cracks may join other cracks to form a dominant flaw or may be deflected at the fiber/matrix interface. It appears that the fiber/matrix interface plays an important role in the overall toughness and strength of the composite. For instance, a relatively weak interface may help deflect matrix cracks while a strong interface may lead to fiber fracture and the eventual catastrophic failure of the composite. The literature on factors

affecting the toughness of ceramics and ceramic composites is extensive. The microstructural dependence of fracture parameters of ceramics are given in [1-12]. Particle and grain size effects are studied in [13-17]. Microcracking in particulate ceramic composites due to thermomechanical stress is investigated in [18].

In this work microcracking in Nicalon/SiC ceramic composite is studied for thermomechanical loading. Monolithic SiC (matrix material) and composite specimens are first observed under microscope, and the fiber distribution patterns are identified. Thus analytical studies relevant to typical fiber distribution patterns (e.g., a single fiber embedded in an infinite medium, two isolated fibers, a ring distribution of fibers, etc.) are performed and the consequences on matrix microcracking are discussed. Next the toughness of matrix material (SiC) is determined under various temperatures (up to 800 C) using the micro-indentation technique [19,20]. The effect of fibers on the "apparent fracture toughness" of matrix is determined experimentally again using the micro-indentation technique. A theoretical model predicting the microcracking behavior is then developed. Finally, the debonding strength of the interface at the initiation of debonding is determined by a method combining experimental results and finite element calculations.

2. The Material: Nicalon/SiC Composite

The material studied is Nicalon/SiC purchased from Amercom, Inc., Chatsworth, CA. The properties of the constituents are given in the following table:

	Young's Modulus E (psi)	Coefficient of Thermal Expansion α (in/in/ C)
Fibers (Nicalon)	26×10^6	3.1×10^{-6}
Matrix (SiC)	55×10^6	4.3×10^{-6}

It should be noted that this material is a reversed composite. That is, stiffness of the matrix (SiC) is greater than that of the fibers (Nicalon). The volume fraction of fibers V_f is approximately 0.35 and the void volume fraction V_d is about 0.15. The composite is manufactured using the chemical vapor deposition (CVD) method.

Using the information obtained from preliminary testing and considering the size of the heating chamber of the furnace, the test specimens were designed as follows:

12 pc. of $(1/2)" \times (1/2)" \times (1/4)"$ 3-D braided Nicalon/SiC specimens infiltrated by CVD to a minimum density of 2.3 g/c.c.

6 pc. of $(1/2)" \times (1/2)" \times (1/4)"$ silicon carbide coated graphite specimens coated on one face with SiC by CVD to a minimum thickness of 0.020 inches.

The first set of specimens is used to determine the effect of fibers on matrix microcracking and the shear strength of the fiber/matrix interface. The second set is used to determine the fracture toughness of the matrix at varying temperatures.

An examination of the composite specimens under microscope reveals that there are basically four fiber distribution patterns: (a) an isolated fiber (Photo 1), (b) two isolated fibers (Photo 2), (c) a circular array (ring) of

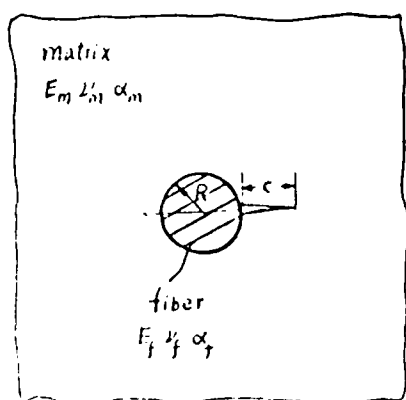
fibers (Photo 3), and (d) closely packed, randomly distributed fibers. The microcracks could be in the matrix or at the interface. Thus the analytical studies presented in the next section are based on models simulating the observed configurations.

3. The Theoretical Studies

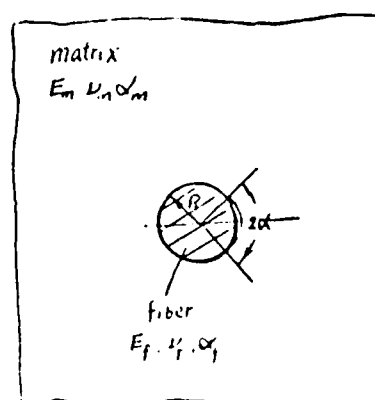
The analysis for each specific model considered is outlined below.

(a) The single-fiber model

This model is designed to simulate situations seen in Photo 1. It is assumed that a single fiber is embedded in an infinite matrix. The microcracking configurations studied are shown in Fig. 1.



(a) Radial Crack in Matrix



(b) Interface Crack

FIGURE 1.

First the stress fields for the uncracked configurations are computed in closed form for temperature rise as well as mechanical loads. Consider a ceramic fiber of radius R embedded in an infinite ceramic matrix as shown in Fig. 2. If the temperature is increased by T , the stresses in the fiber and the matrix can easily be found by considering a uniformly loaded

cylinder and a plane with a hole and matching the displacement at their common boundary. After some algebra, we obtain:

$$\text{for } r < R \left\{ \begin{array}{l} \sigma_{rr} = \bar{\sigma} \\ \sigma_{\theta\theta} = -\bar{\sigma} \end{array} \right. \quad (\text{in the fiber}); \quad (1)$$

$$\text{for } r > R \left\{ \begin{array}{l} \sigma_{rr} = \bar{\sigma} \left(\frac{R}{r} \right)^2 \\ \sigma_{\theta\theta} = -\bar{\sigma} \left(\frac{R}{r} \right)^2 \end{array} \right. \quad (\text{in the matrix}); \quad (2)$$

where

$$\bar{\sigma} = \frac{\alpha_m (1+\nu_m) - \alpha_f (1+\nu_f)}{\lambda} \Delta T; \quad (3)$$

and

$$\lambda = \frac{1+\nu_m}{E_m} + \frac{1-\nu_f-2\nu_f^2}{E_f}. \quad (4)$$

Here (E_m, ν_m, α_m) and (E_f, ν_f, α_f) are the Young's moduli, the Poisson's ratios and the coefficients of thermal expansion for the matrix and fibers, respectively. Assuming $\Delta T > 0$, i.e. heating, and considering that $\nu_m \approx \nu_f$, one may conclude immediately that if $\alpha_m < \alpha_f$, $(\sigma_{\theta\theta})_{\text{matrix}}$ is tensile and may induce radial cracks in the matrix. On the other hand if $\alpha_m > \alpha_f$, $(\sigma_{rr})_{\text{matrix}}$ is tensile with the possibility of debonding along the fiber-matrix interface. In practice of course, in addition to the thermal stresses described above, one has to include also the mechanical stresses due to external loading and the residual stresses induced in the material during the manufacturing process.

Radial crack in the matrix. Consider the radial crack geometry shown in Fig. 1(a). The formulation of this problem for uniaxial loading is given in [21]. Here instead of external loads, the crack surface will be loaded with the residual stresses derived in the previous section and expressed by Eq. (2). Referring to [21], after some simplification the formulation of the problem in terms of the crack surface displacement derivative $f(t)$ can be written as:

$$\int_R^{c+R} \frac{f(t)}{t-x} dt + \int_R^{c+R} [k_{11s}(x,t) + k_{11f}(x,t)] f(t) dt = \frac{\pi(\Xi_m + 1)}{2\mu_m} p(x), \quad R < x < c+R; \quad (5a)$$

with the single valuedness condition:

$$\int_R^{c+R} f(t) dt = 0; \quad (5b)$$

where

$$\begin{aligned} k_{11s}(x,t) &= \frac{1}{t-s} [(A_1 + A_2) \frac{s}{2x} + \frac{A_1}{x^2} (3s^2 - R^2) (1 - \frac{2s}{t})] \\ &\quad + A_1 [(1 - \frac{4s}{t}) \frac{s(s^2 - R^2)}{x^2(t-s)^2} - \frac{s^3(s^2 - R^2)^2}{R^4 t(t-s)^3}]; \\ k_{11f}(x,t) &= \frac{A_1 R^2}{x^2} (\frac{2}{x} + \frac{1}{2t} - \frac{3R^2}{tx^2}) - [M(\Xi_f + 1) - 1] \frac{R^2}{2tx^2}; \\ A_1 &= \frac{1-m}{1+m\Xi_m}; \quad A_2 = \frac{\Xi_f - m\Xi_m}{\Xi_f + m}; \quad s = \frac{R^2}{x}; \quad m = \frac{\Xi_f}{\Xi_m}; \quad M = \frac{m(\Xi_m + 1)}{(\Xi_f + m)(\Xi_f - 1 + 2m)}; \\ \Xi_m &= 3 - 4\nu_m; \quad \Xi_f = 3 - 4\nu_f; \quad \mu_m = \frac{E_m}{2(1+\nu_m)}; \quad \mu_f = \frac{E_f}{2(1+\nu_f)}. \end{aligned} \quad (6)$$

For the problem under consideration, the crack surface will be loaded with the negative of residual stress $\sigma_{\theta\theta}$ given in Eq. (2). Thus,

$$p(x) = \frac{-R^2}{x^2}. \quad (7)$$

To solve the singular integral equation (5a), the following normalization is used:

$$\begin{aligned} x &= \frac{c}{2}\rho + R + \frac{c}{2}, & \text{for } R < x < c+R \text{ and } -1 < \rho < +1; \\ t &= \frac{c}{2}\tau + R + \frac{c}{2}, & \text{for } R < t < c+R \text{ and } -1 < \tau < +1; \\ f(t) &= g(\tau); \quad k_{11s}(x, t) = K_{11s}(\rho, \tau); \\ p(x) &= q(\rho); \quad k_{11f}(x, t) = K_{11f}(\rho, \tau). \end{aligned} \quad (8)$$

Then Eqs. (5a,b) become:

$$\begin{aligned} \int_{-1}^{+1} \frac{g(\tau)}{\tau - \rho} d\tau + \frac{c}{2} \int_{-1}^{+1} [K_{11s}(\rho, \tau) + K_{11f}(\rho, \tau)]g(\tau) d\tau \\ = \frac{\pi(\Xi_m + 1)}{2\mu_m} q(\rho), \quad -1 < \rho < +1; \end{aligned} \quad (9a)$$

and

$$\int_{-1}^{+1} g(\tau) d\tau = 0. \quad (9b)$$

The normalized crack surface displacement $g(\tau)$ is singular at $\tau = \pm 1$ and may be written as [22]:

$$g(\tau) = \frac{G(\tau)}{\sqrt{1-\tau}(1+\tau)^{-\beta}}; \quad (10)$$

where $G(\tau)$ is a bounded function and $-1 < \beta < 0$ is given by [21] as:

$$2\cos\pi\beta + (A_1+A_2) - 4A_1(\beta+1)^2 = 0. \quad (11)$$

At the crack tip embedded in the matrix the stress intensity factor can be defined as:

$$k(c) = \lim_{x \rightarrow R+c} \sqrt{2[x-(R+c)]} \sigma_{yy}(x, 0) \Big|_{\text{matrix}}. \quad (12)$$

Using Eqs. (5a), (8) and (10) and after some lengthy algebra, we obtain:

$$k(c) = -\frac{2\mu_m}{\frac{\nu_m}{m} + 1} \sqrt{c} 2^\beta G(1). \quad (13)$$

Noting that $K_I = \sqrt{\pi} k(c)$, then the strain energy release rate is found to be:

$$G_I = \frac{K_I^2 (1-\nu_m^2)}{E_m} = \frac{\pi}{E_m} (1-\nu_m^2) k^2(c); \quad (14)$$

or

$$G_I = \frac{\pi}{E_m} (1-\nu_m^2) R \frac{c}{R} \left(\frac{k(c)}{\sqrt{c}} \right)^2. \quad (15)$$

Defining $\frac{c}{R} = \epsilon$ and noting that $\frac{k(c)}{\sqrt{c}} = \bar{\sigma} k'(\epsilon)$, Eq. (15) becomes:

$$G_I = \frac{\pi}{E_m} (1-\nu_m^2) R \epsilon [k'(\epsilon)]^2 \bar{\sigma}^2. \quad (16)$$

The radial matrix crack will propagate when the strain energy release rate reaches the critical strain energy release rate of the matrix, i.e., when

$G_I \geq (G_{Ic})_{\text{matrix}}$. Equating Eq. (16) with $(G_{Ic})_{\text{matrix}}$, we obtain the critical fiber size as:

$$R_c = \frac{(G_{Ic})_{\text{matrix}} E_m}{\pi(1-\nu_m^2) \epsilon [k'(\epsilon)]^2 \bar{\sigma}^2}. \quad (17)$$

However, the crack size (or ϵ) is not known a priori. Therefore, we can determine only a minimum critical fiber size which will occur when $g(\epsilon) = \epsilon [k'(\epsilon)]^2$ is maximum. Thus,

$$R_c^{\min} = \frac{(G_{Ic})_{\text{matrix}} E_m}{\pi(1-\nu_m^2) [g(\epsilon)]_{\max} \bar{\sigma}^2}. \quad (18)$$

Formula (18) can be used to conservatively determine the critical fiber size for radial matrix crack suppression.

As an example, the fibers are assumed to be SiC and the matrix a glass-ceramic (lithium aluminosilicate or LAS) with the following properties [23]:

$$E_m = 85 \text{ GPa}; \quad \nu_m = 0.2; \quad \alpha_m = 9 \times 10^{-6}/^\circ\text{C};$$

$$E_f = 200 \text{ GPa}; \quad \nu_f = 0.2; \quad \alpha_f = 4 \times 10^{-6}/^\circ\text{C}.$$

$$(G_c)_{\text{interface}} = 20 \text{ Pa-m}; \quad \Delta T = -1000^\circ\text{C}; \quad (K_{Ic})_{\text{matrix}} = 2 \text{ MPa}\sqrt{\text{m}}; \quad \text{or}$$

$$(G_{Ic})_{\text{matrix}} = (K_{Ic})_{\text{matrix}}^2 (1-\nu_m^2)/E_m = 45.18 \text{ Pa-m}.$$

Equations (9a) and (9b) are solved numerically for the material combination defined above by using the collocation technique described in [24,25].

Figure 3 shows the variation of $g(\epsilon)$ with $\frac{c}{R}$. It is seen that the curve

passes through a maximum around $[g(\epsilon)]_{\max} \approx 0.075$. It must be noted that the variation of $g(\epsilon)$ shown in Fig. 3 is for the specific material combination used in the example. To assess the effect of the elastic properties on the value of $g(\epsilon)$, results are obtained for various ratios of E_m/E_f ranging from 0.2 to 5. These results are shown in Fig. 4.

As can be seen from Fig. 4, surprisingly the E_m/E_f ratio has little effect on $g(\epsilon)$. Therefore, one curve can represent all practical material combinations, including the Nicalon/SiC being studied here. Using the value $[g(\epsilon)]_{\max} = 0.075$ and substituting into Eq. (18), we obtain $R_c^{\min} \approx 148\mu\text{m}$, which is larger than the actual fiber size used in such composites.

Interface crack along the fiber/matrix boundary. For this case, the crack geometry is shown in Fig. 1(b). It is well known that at the interface crack tip the stresses and strains have an oscillatory singularity [26-30] and the stress intensity factors cannot be defined by using their classical definition. Instead, we will determine the strain energy release rate at the crack tip which is not affected by this peculiar behavior. The problem does not appear to have been solved for thermal stresses. Using the solution given by Toya [31] and the superposition principle we present here a solution for the residual stress loading expressed by Eqs. (1) and (2). For the plane loading shown in Fig. 5, the strain energy release rate at the interface crack tip is given as [31]:

$$G = \frac{1}{4}kRA_0(1+4\lambda_0^2)\pi N\bar{N}\sin\alpha\exp[2\lambda_0(\pi-\alpha)]; \quad (19)$$

where

$$k = \frac{\beta_0}{1+\nu}; \quad \nu = (\mu_f + \Xi_f \mu_m) / (\mu_m + \Xi_m \mu_f); \quad \beta_0 = \mu_m (1 + \Xi_f) / (\mu_m + \Xi_m \mu_f)$$

$$A_0 = \frac{k}{4} \left(\frac{1 + \Xi_m}{\mu_m} + \frac{1 + \Xi_f}{\mu_f} \right); \quad \lambda_0 = -\ln \nu / 2\pi;$$

$$N = (c_0 - \frac{d-1}{k}) + \frac{1-k}{k} (N_\infty - T_\infty) \exp[i(2\phi - \alpha) + 2\lambda_0(\alpha - \pi)]; \quad c_0 = G_0 + iH_0;$$

$$G_0 = [\frac{1}{2}(N_\infty - T_\infty) \{1 - (\cos \alpha + 2\lambda_0 \sin \alpha) \exp[2\lambda_0(\pi - \alpha)]\}]$$

$$- \frac{1}{2}(1-k)(1+4\lambda_0^2)(N_\infty - T_\infty) \sin^2 \alpha \cos 2\phi] /$$

$$\{2 - k - k(\cos \alpha + 2\lambda_0 \sin \alpha) \exp[2\lambda_0(\pi - \alpha)]\};$$

$$H_0 = [\frac{1}{2}(1-k)(1+4\lambda_0^2)(N_\infty - T_\infty) \sin^2 \alpha \sin 2\phi$$

$$+ \frac{4\mu_m i \epsilon_\infty}{1 + \Xi_m} \{1 + (\cos \alpha + 2\lambda_0 \sin \alpha) \exp[2\lambda_0(\pi - \alpha)]\}] /$$

$$k(1 + (\cos \alpha + 2\lambda_0 \sin \alpha) \exp[2\lambda_0(\pi - \alpha)])];$$

$$d_{-1} = \frac{1}{2}(N_\infty - T_\infty) + \frac{4\mu_m i \epsilon_\infty}{1 + \Xi_m}.$$

where ϵ_∞ is the rotation at infinity, \bar{N} is the complex conjugate of N , and T_∞ , N_∞ , R , α and β are shown in Fig. 5. To obtain the solution for a constant crack surface pressure $\bar{\sigma}$, which is the loading shown in Fig. 1(b) and expressed by Eqs. (1) and (2), consider the stress distribution for a cylindrical inclusion embedded in an infinite matrix under uniaxial tension σ_0 (Fig. 6). The radial stress along the fiber/matrix interface may be expressed as [32]:

$$\sigma_{rr} = \frac{\sigma_0}{2} (1 - \cos 2\theta) - 2\sigma_0 (A(\frac{R}{r})^2 + B[3(\frac{R}{r})^4 - 4(\frac{R}{r})^2] \cos 2\theta); \quad (20)$$

where

$$A = \frac{(1-2\nu_f)\mu_m - (1-2\nu_m)\mu_f}{4[(1-2\nu_f)\mu_m + \mu_f]},$$

and

$$B = \frac{\mu_m - \mu_f}{4[\mu_m + (3-4\nu_m)\mu_f]}.$$

Superimposing to this expression a uniaxial loading σ_0 in the x direction, with $r=R$, the radial stress along the fiber/matrix interface becomes constant (independent of θ):

$$\sigma_{rr} = \sigma_0(1-4A). \quad (21)$$

Thus, to obtain a stress $\bar{\sigma}$ =constant at the interface, we must have:

$$\sigma_0 = \bar{\sigma}/(1-4A). \quad (22)$$

The strain energy release rate at the crack tip for the thermal loading is then obtained by using Eq. (19) with $T_\infty = N_\infty = \frac{\bar{\sigma}}{1-4A}$ and $\phi = \frac{\pi}{2}$. Defining:

$$G' = \frac{GE_m}{2(1+\nu_m)\bar{\sigma}^2 R}; \quad (23)$$

the critical fiber size for the suppression of interface cracking can be obtained by equating G to G_c , the total critical strain energy release rate of the interface. Again, noting that the crack length is not known a priori, we obtain the minimum critical fiber size R_c^{\min} when G' is maximum, G'_{\max} . Thus:

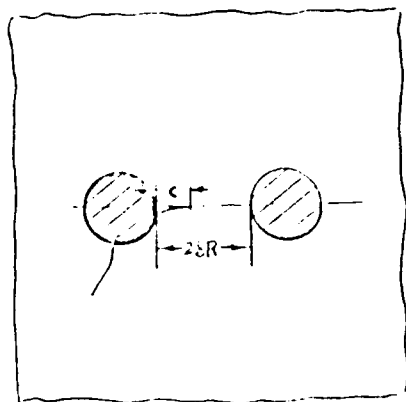
$$R_c^{\min} = \frac{G_c E_m}{2(1+\nu_m)\sigma^2 G'_{\max}}. \quad (24)$$

As an example, we assume the material properties given in the previous section. Figure 7 shows the variation of G' with the crack angle α . Again, it is seen that the curve reaches a maximum of $G' \approx 0.53$ at $\alpha \approx 65^\circ$. With these values and $\Delta T = +1,000^\circ\text{C}$, Eq. (24) gives $R_c^{\min} \approx 11.7\mu\text{m}$ which is of the same order as the actual fiber size. To assess the effect of the elastic properties, the ratio of Young's moduli, E_m/E_f , is varied from 0.2 to 5. Unlike the case of radial cracking, as Fig. 8 shows, for interface cracking the normalized strain energy release rate G' is heavily dependent on the elastic properties of the constituents.

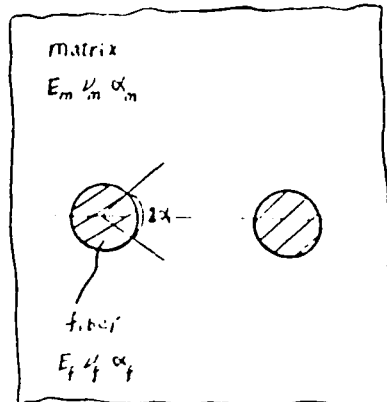
(b) Interaction of two fibers

This model is designed to simulate situations similar to those seen in Photo 2. In this case it is assumed that two fibers are embedded in an infinite matrix and subjected to mechanical or thermal loads. Again we considered two crack configurations: (a) a radial matrix crack and (b) an interface crack as shown in Figs. 9(a) and 9(b), respectively. Due to the complexity of the geometry, here numerical and approximate methods have been used to develop the solutions. For the uncracked geometry, the stress fields in the matrix and at the fiber/matrix interface are determined using the finite element technique. We have developed a finite element computer procedure using ANSYS [33] which gives the stress and displacement fields for in-plane mechanical and thermal loadings. Figures 10 to 15 show the typical stress distributions of the two-fiber model due to thermal loading

and Figs. 16 to 21 show the stress distributions due to mechanical loading. In either case effects of various Young's modulus ratios and fiber spacings were investigated. It is found that the stress distributions are strongly influenced by fiber interaction.



(a) Radial Crack in Matrix



(b) Interface Crack

FIGURE 9.

The crack configurations shown in Figs. 9(a) and 9(b) are handled as follows: For the radial crack, we developed an approximate solution in terms of a singular integral equation. The approximation is due to the fact that the kernel used in the singular integral equation is taken from the single fiber model, while the crack surfaces are loaded with the negative of the stresses obtained above. This means that Eqs. (5) to (18) are still valid with the understanding that $p(x)$ in Eq. (5a) is now replaced by the stress obtained for the uncracked two-fiber geometry. The numerical results are computed for varying material properties and fiber separation ($2\delta R$) and are displayed in Figs. 22 to 24. The results indicate that (a) material properties have very little effect on the normalized fracture energy, $g(\epsilon)$, as shown in Fig. 22; (b) the separation plays a significant role on whether crack arrest is possible (e.g., Fig. 23 indicates that when δ is large,

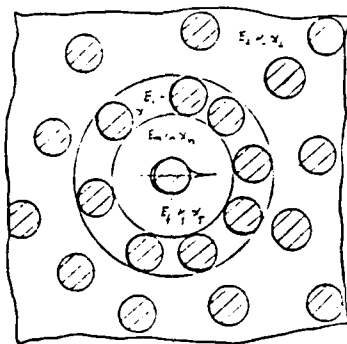
i.e., the fibers are far from each other, the normalized strain energy release rate passes through a maximum making crack arrest possible; on the other hand when δ is small, i.e., when the fibers are close to each other, there is no possibility of radial crack arrest); and (c) the variation of the normalized strain energy release rate $g(\epsilon)$ is drastically different for the single-fiber and the two-fiber geometries.

For the interface crack problem, again an approximate solution based on Toya's single-fiber model [31] is developed. First it may be noted that Toya's solution [31] (Fig. 25(a)) can be considered as the superposition of an uncracked geometry (Fig. 25(b)) and a crack loaded with the negative stresses obtained in the first part (Fig. 25(c)). Then the strain energy release rate can be computed by considering only the perturbation problem shown in Fig. 25(c). Next the thermal- or mechanical-loading induced tangential and radial stresses at the fiber/matrix interface, as shown in Figs. 10 to 21, can be approximated in the least square sense to yield the crack surface tractions prescribed in Fig. 5(c). Thus in Toya's solution, Eq. (19), the forces N and T and the angle ϕ are replaced by N_{eq} , T_{eq} and ϕ_{eq} , respectively. The numerical results are displayed in Figs. 26 to 30 for thermal and mechanical loading, where the normalized strain energy release rate is plotted against the interfacial crack angle α . The material properties and the crack spacing are varied and the results are compared with those obtained for the single-fiber case. It is found that the properties of fibers and matrix and the spacing of fibers may affect the interfacial crack propagation considerably. Furthermore, contrary to the radial crack case, the variation of G' is similar qualitatively for both the

single-fiber and the two-fiber cases, making interfacial crack arrest possible (see Figs. 27 to 30).

(c) The ring model

This model is designed to simulate situations similar to those seen in Photo 3. The model consists of a single fiber surrounded by a circular array of fibers. This array of fibers is assumed to form a ring of material with properties obtained by considering it a composite. The model is shown in Fig. 31. The stress distribution in the uncracked composite due to mechanical and thermal loadings can be obtained in closed form using Mitchell's solution [34] for the four regions shown in Fig. 32.



The Ring Model

FIGURE 31.

Assuming plane strain,

$$\epsilon_{zz1} = \epsilon_{zz2} = \epsilon_{zz3} = \epsilon_{zz4} = 0; \quad (25)$$

i.e.

$$\epsilon_{zz1} = \frac{1}{E_f} [\sigma_{zz1} - \nu_f (\sigma_{rr1} + \sigma_{\theta\theta1})] + \alpha_f \Delta T; \quad (26)$$

$$\epsilon_{zz2} = \frac{1}{E_m} [\sigma_{zz2} - \nu_m (\sigma_{rr2} + \sigma_{\theta\theta2})] + \alpha_m \Delta T; \quad (27)$$

$$\epsilon_{zz^3} = \frac{1}{E_3} [\sigma_{zz^3} - \nu_3 (\sigma_{rr^3} + \sigma_{\theta\theta^3})] + \alpha_3 \Delta T; \quad (28)$$

$$\epsilon_{zz^4} = \frac{1}{E_{43}} [\sigma_{zz^4} - \nu_{43} (\sigma_{rr^4} + \sigma_{\theta\theta^4})] + \alpha_4 \Delta T. \quad (29)$$

Equations (26)-(29) can also be written as:

$$\sigma_{zz^1} = \nu_f (\sigma_{rr^1} + \sigma_{\theta\theta^1}) - E_f \alpha_f \Delta T; \quad (30)$$

$$\sigma_{zz^2} = \nu_m (\sigma_{rr^2} + \sigma_{\theta\theta^2}) - E_m \alpha_m \Delta T; \quad (31)$$

$$\sigma_{zz^3} = \nu_3 (\sigma_{rr^3} + \sigma_{\theta\theta^3}) - E_3 \alpha_3 \Delta T; \quad (32)$$

$$\sigma_{zz^4} = \nu_{43} (\sigma_{rr^4} + \sigma_{\theta\theta^4}) - E_{43} \alpha_4 \Delta T. \quad (33)$$

In these equations E_m , E_f , ν_m , ν_f , α_m , α_f refer to the Young's moduli, Poisson's ratios and thermal expansion coefficients of the matrix and fibers, respectively, while E_3 , ν_3 , E_{43} , ν_{43} are the composite elastic properties for regions 3 and 4, which are described below with the geometry shown in Fig. 33.

Region 3 contains a group of fibers randomly distributed in a concentric annular domain with inner radius b and outer radius c . The Young's modulus E_3 , Poisson's ratio ν_3 and thermal expansion coefficient α_3 of the composite are dependent on n , the number of the fibers in this domain and the geometrical parameters. As shown below, they can be determined by virtue of the rule of mixtures:

$$E_3 = E_f \frac{n a^2}{c^2 - b^2} + E_m \frac{c^2 - b^2 - n a^2}{c^2 - b^2}; \quad (34)$$

$$\nu_3 = \nu_f \frac{n a^2}{c^2 - b^2} + \nu_m \frac{c^2 - b^2 - n a^2}{c^2 - b^2}; \quad (35)$$

$$\alpha_3 = \alpha_f \frac{na^2}{fc^2 - b^2} + \alpha_m \frac{c^2 - b^2 - na^2}{c^2 - b^2}. \quad (36)$$

Region 4 is an infinitely extended domain with a hole of radius c . The material in this region is transversely isotropic and the Young's modulus, Poisson's ratio and thermal expansion coefficient of the material are determined by the following formulas (see Fig. 33):

$$E = \frac{1}{V_f V_m} \frac{\frac{1}{E_f} + \frac{1}{E_m}}{ }; \quad (37)$$

where E is the Young's modulus in x_1 - x_2 plane (see Fig. 33), V_f is the volume fraction of fibers defined as:

$$V_f = \frac{(n+2)\pi a^2}{\pi c^2} \quad \text{and} \quad V_m = 1 - V_f; \quad (38)$$

with n the number of fibers inside the ring.

$$\nu = V_f \nu_f + (1-V_f) \nu_m = \frac{4c^2 - (n+3)\pi a^2}{4c^2} \nu_f + \frac{(n+3)\pi a^2}{4c^2} \nu_m; \quad (39)$$

$$\alpha = V_f \alpha_f + (1-V_f) \alpha_m = \frac{4c^2 - (n+3)\pi a^2}{4c^2} \alpha_f + \frac{(n+3)\pi a^2}{4c^2} \alpha_m; \quad (40)$$

$$E_{13} = V_f E_f + (1-V_f) E_m = \frac{4c^2 - (n+3)\pi a^2}{4c^2} E_f + \frac{(n+3)\pi a^2}{4c^2} E_m; \quad (41)$$

where ν and α are the Poisson's ratio and the thermal expansion coefficient in the x_1 - x_2 plane and E_{13} is the Young's modulus in the x_3 direction.

Furthermore

$$\nu_{43} = \nu; \quad (42)$$

and

$$\alpha_4 = \alpha; \quad (43)$$

where ν_{43} and α_4 are properties in x_3 direction.

Influence of the surrounding fibers in the ring model is considered in the average sense. The influence of the surrounding fibers can be adjusted either by changing the value of b , i.e., changing the closeness of the fiber cluster or by changing the number of the fibers n in the ring. When the number of the fibers in the ring is changed, the volume fraction of the fibers in the ring is changed; and thus the Young's modulus E_3 , Poisson's ratio ν_3 and the thermal expansion coefficient α_3 will all change and the influence of the ring (fiber cluster) will be different.

The continuity conditions at the interfaces can be written as:

$$u_1 = u_2, \quad v_1 = v_2, \quad r_{r\theta 1} = r_{r\theta 2}, \quad \sigma_{rr1} = \sigma_{rr2}; \quad (r = a) \quad (44)$$

$$u_2 = u_3, \quad v_2 = v_3, \quad r_{r\theta 2} = r_{r\theta 3}, \quad \sigma_{rr2} = \sigma_{rr3}; \quad (r = b) \quad (45)$$

$$u_3 = u_4, \quad v_3 = v_4, \quad r_{r\theta 3} = r_{r\theta 4}, \quad \sigma_{rr3} = \sigma_{rr4}. \quad (r = c) \quad (46)$$

Solving the equations, we obtain the expressions for stresses in closed form. Based on the expression which are very lengthy to reproduce here, a typical distribution of $\sigma_{\theta\theta}$ is given in Fig. 34. The crack problem for this case is discussed later in Sec. 5.

4. Experimental Work

The experimental program is designed to accomplish the following: (a) to observe and document the microcracking patterns of a ceramic-fiber/

ceramic-matrix composite under high temperature, (b) to obtain the variation of the fracture toughness of the matrix material with temperature, (c) to evaluate the effects of such factors as fiber size and distribution, thermal expansion coefficients, and temperature rise on matrix microcracking of ceramic composites, and (d) to determine the shear strength at the fiber/matrix interface.

(a) The experimental set-up

The experiments consist of micro-indenting monolithic and composite specimens with a microhardness indenter under various temperatures and recording the resulting microcracking patterns using a microscope. For this purpose an ATS series 3320 split-tube laboratory furnace (Applied Test Systems, Inc., Butler, PA) which can be heated up to 3000°F in 30 minutes and a Nikon UM-2 universal measuring microscope are used. The indentation load is recorded by a 10-lb super-mini load cell (Interface, Inc., Scottsdale, AZ) and the temperature is read by a type-B platinum/platinum-30% rhodium thermocouple. A sketch of the experimental set-up is shown in Fig. 35. Figure 36 shows the series 3320 split-tube laboratory furnace.

(b) Effect of temperature on toughness of matrix material

The toughness of the matrix material is obtained by indenting monolithic SiC coated specimens described in Sec. 3. The specimens were first mounted in a bakelite mold, polished with paste of extra fine alumina and diamond powders (as small as half a micron) and indented with a diamond Vickers indenter (Wilson Instruments, Inc., Bridgeport, CT). They were then examined under optical and scanning electron microscopes to document pre-existing microcracks and only a few of them were observed. To ascertain the effect of temperature on the toughness of the material, the testing

temperature was varied from room (25°C) to 800°C . Thus micro-indentation tests were carried out at 25°C , 250°C , 600°C and 800°C . At each temperature level the indentation load P was recorded by the super-mini load cell and the half size of the impression D , as shown in Fig. 37, was measured by the Nikon UM-2 microscope. From this information one may calculate the toughness of the material using a typical formula as given below:

$$K_{Ic} = \frac{1}{\pi^{3/2} \tan\psi} \left(\frac{P}{D^{3/2}} \right), \quad (47)$$

where P is the applied load, D the half crack length and $\psi = 68^{\circ}$ is the indenter angle. Details of the indentation technique can be found in Lawn et al. [19] or Evans [20]. The results for the fracture toughness of SiC at various temperatures are displayed in Fig. 38. One may note that, as expected, there is some scattering in the results. However, more importantly it seems that the fracture toughness of SiC decreases significantly with increasing temperature. For example K_{Ic} decreases from approximately $4.5 \text{ ksi}/\sqrt{\text{in}}$ at room temperature to $3.5 \text{ ksi}/\sqrt{\text{in}}$ at 800°C . The fracture toughness of the matrix was also measured from the composite specimens. To preclude any effect of fibers on the results, the indentation was done in sites with no neighboring fibers. The same results were obtained, as will be seen later from the results presented in Figs. 40-43.

(c) Effect of fibers and temperature on the "apparent toughness" of the matrix

Just like the case for the monolithic specimens described in Sec. 4(b), each Nicalon/SiC ceramic composite specimen was also first mounted in a bakelite mold, polished and examined under optical and scanning

electron microscopes to document the pre-cracking (existing microcracks) and the fiber distribution patterns used in the analytical model. Again only a few existing microcracks were observed. The specimens were then heated in the ATS furnace up to 3000°F. The heated specimens were later examined under optical and scanning electron microscopes. Again no further microcracking was observed due to temperature rise alone. This confirms the claim of the manufacturer and our preliminary calculations, using the single-fiber model, Sec. 3(a), that for this material microcracks do not occur under thermal loading alone. The combination of thermal and mechanical loadings is necessary to generate microcracks.

Next the 1/2"x1/2"x1/8" Nicalon/SiC composite specimens with fibers facing up were also polished as before and in the matrix of the composite, microcracks were generated again using the indentation technique at various temperatures ranging from room to 800°C. To ascertain the effects of fibers, the specimens were indented at locations of varying fiber density and the fracture toughness was calculated using Eqn. (47), as if the fibers did not exist. Since the fracture toughness described above contains the effect of fibers, from here on it will be referred to as the "apparent fracture toughness" of the matrix material (SiC). The effect of fibers is introduced through the concept of local volume fraction: A cell of fixed proportions, Fig. 39, (say, $b/a=3$, where $2a$ is the crack length and $2b$ is the total length of the cell) is selected with the indentation imprint at the center and several fibers scattered within the composite cell. The local volume fraction V_f is defined as the ratio of the total cross-sectional areas of fibers to the total area of the composite cell. As a

consequence, at each indentation site, one obtains a different local V_f . The experimental results obtained at room (25°C), 250°C , 600°C and 800°C are shown in Figs. 40 to 43. In each figure the "apparent fracture toughness" is plotted against the local volume fraction of fibers, V_f , at a given temperature. It is observed that the "apparent fracture toughness" decreases with increasing local volume of fibers and also with increasing temperature. This means that it is easier to generate microcracks at a location where the density of fibers is higher and when the temperature is increased. The result that the "apparent fracture toughness" of the matrix is decreasing with increasing local volume fraction must be expected, since the composite under consideration is a so-called "reversed" composite, meaning that the matrix is stiffer than the fibers. Here the Young's modulus of the matrix material (SiC) is $E_m=55\times 10^6$ psi and the Young's modulus of fibers (Nicalon) is $E_f=26\times 10^6$ psi. These results are summarized in Fig. 44, where the experimental data are presented with fitted straight lines.

(d) Determination of interfacial strength and interfacial stresses

The interfacial strength at debonding initiation is determined by a combination of experimental measurements and finite element analysis. First the load at debonding initiation is measured. For this purpose some specimens were micro-indented at room temperature using the Wilson Tukon 300 microhardness tester whose attached microscope enabled us to indent at the desired site and to observe the ensuing microcracks. For instance, two perpendicular matrix cracks generated by loading a Vickers indenter at 600

grams is shown in Photo 4. Photo 5 shows a partial interfacial crack produced at the interface of a fiber which is surrounded by a circular array of fibers. The Vickers indenter was loaded at 50 grams with an eccentricity of approximately three quarters of the fiber radius. Photo 6 depicts complete debonding of two isolated fibers, each was loaded eccentrically with a Vickers indenter at 50 grams. The eccentricity in either fiber is about one half of the fiber radius. From these observations we can conclude that the micro-indentation fracture behavior of ceramic composites is affected not only by the magnitude and location of the indenter but also by the distribution of the fibers, i.e. fiber interaction.

To simplify the calculation, the indentation is performed at isolated fiber locations when determining the interfacial shear strength. One can then neglect the far away fibers and model the problem as a fiber surrounded by an infinite matrix. In general, however, the model used is a single fiber surrounded by an annulus of matrix material with the rest of fibers and matrix being modeled as a transversely isotropic composite as shown in Fig. 45. A similar model was developed in [35]. A number of debonding experiments were conducted and in each case the critical load P_{cr} , which is the load at debonding initiation, and the fiber size were recorded. During the debonding test the indenter is pressed at the center of the fiber and the load is applied incrementally until complete debonding occurs. Through a regression analysis, it can easily be shown that the critical loads P_{cr} are proportional to the square of fiber radii (see Fig. 46). This finding indicates that the results are consistent for all the fibers with different sizes.

To relate the critical debonding load to the strength of the fiber-matrix interface, one needs the distribution of interfacial stresses. For this purpose a finite element model has been developed. In the finite element model the loading is specified as a concentrated force acting at the center of the fiber (Fig. 44(b)). In the analysis ANSYS [33] finite element code is used. Since the geometry and loading are axisymmetric, the axisymmetric element is employed. To check the accuracy of the solution, the fiber and the matrix are assigned the same mechanical properties and the results obtained are compared with the closed form Boussinesq's solution [34]. The results agree extremely well. The calculations are performed in two steps, i.e. first a course mesh is used and later a finer mesh is employed. A typical mesh used in the computation is shown in Fig. 46a. The normalized shear and radial stresses at the fiber-matrix interface are shown in Fig. 47. The stresses due to temperature change were also considered and are displayed in Fig. 48. The debonding shear strength is the maximum shear strength when the load is P_{cr} . Based on the analysis given above, the shear strength can be calculated by the following formula:

$$\tau_{rf} \mid_{critical} = \frac{K}{\frac{1}{P_{cr}/R^2} + \frac{1}{E_m \alpha_m \Delta T}}; \quad (48)$$

where K is a constant (in our example $K \approx 0.18$), P_{cr} the critical load (i.e., the load at the onset of debonding), E_m Young's modulus of the matrix, α_m thermal expansion coefficient of the matrix, R radius of the fiber being tested and ΔT change in temperature.

5. Theoretical Prediction and Comparison with Experimental Results

To explain and predict the observed experimental results given in the previous section, a theoretical model has been developed. In a composite material, the distribution of fibers may assume many patterns such as an isolated fiber, two interacting fibers, a ring of fibers, or random. Here we assume that the fibers form a ring of composite material with elastic properties calculated based on a volume fraction equivalent to the volume fraction in the cell described above. The geometry of the model is shown in Fig. 49. Since the properties of the constituents are fixed, from dimensional considerations, it can be shown that for the ring model the stress intensity factor for a crack of length $2a$ in a uniformly loaded composite can be expressed as:

$$K_I = \sigma_o \sqrt{\pi a} f(V_f, R/a, \Delta T), \quad (49)$$

where σ_o is the crack surface traction, V_f the local fiber volume fraction, R the fiber radius, and ΔT the temperature rise. When σ_o reaches the critical value $(\sigma_o)_c$, K_I will become the toughness of the matrix, $(K_{Ic})_{\text{matrix}}$. Thus the "apparent fracture toughness", which is defined as:

$$(K_{Ic})_{\text{apparent}} = (\sigma_o)_c \sqrt{\pi a}, \quad (50)$$

can be expressed in terms of V_f and R/a as:

$$(K_{Ic})_{\text{apparent}} = \frac{(K_{Ic})_{\text{matrix}}}{f(V_f, R/a, \Delta T)}, \quad (51)$$

where

$$f(V_f, R/a, \Delta T) = \frac{K_I}{\sigma_0 \sqrt{\pi a}}, \quad (52)$$

is the normalized stress intensity factor.

The stress intensity factor K_I is determined using the finite element program ABAQUS [36]. Thus for a given R/a and ΔT , a $(K_{Ic})_{\text{apparent}}$ versus V_f curve can be plotted. Numerical results for $R/a = 0.95$ and $T = 25^\circ\text{C}$, 250°C , 600°C , and 800°C have been computed. The finite element mesh used in the calculations is shown in Fig. 50. The theoretical results obtained for each temperature level are plotted against the experimental results and are depicted in Figs. 51 to 54. It is seen that the agreement between the two sets of results is good. The model also predicts a decreasing "apparent fracture toughness" with local volume fraction of fibers. For low volume fractions and high temperatures, the quantitative prediction is excellent. However, for large volume fractions and low temperatures, there is some deviation between the experimental and the predicted results. This is expected since our model does not take into account the specific arrangement of fibers around the crack tip and the possible mode II effects, which may influence the "apparent fracture toughness" significantly.

6. References

- [1] A. G. Evans and K. T. Faber, "Crack-Growth Resistance of Microcracking in Brittle Materials," Journal of the American Ceramic Society, Vol. 67, pp. 255-260, 1984.
- [2] R. W. Rice, "Fractographic Identification of Strength Controlling Flaws and Microcracking, : in Fracture Mechanics of Ceramics, Vol. 1, ed. R. C. Bradt, D. P. H. Hasselman and F. F. Lange, Plenum Press, New York, 1974, pp. 323-345.

- [3] R. W. Rice, S. W. Frieman, R. C. Pohanka, J. J. Mecholsky, and C. C. Wu, "Microstructural Dependence of Fracture Mechanics Parameters in Ceramics," in Fracture Mechanics of Ceramics, Vol. 4, ed. by R. C. Bradt, D. P. H. Hasselman and F. F. Lange, Plenum Press, New York, 1978, pp. 840-876.
- [4] R. W. Rice, "Microstructural Dependence of Mechanical Behavior of Ceramics," in Treatise on Materials Science and Technology, Vol. 2, Properties and Microstructure, ed. by R. K. McCrone, Academic Press, New York, 1977, pp. 199-381.
- [5] R. W. Rice, R. C. Pohanka and W. J. McDonough, "Effect of Stresses from Thermal Expansion Anisotropy, Phase Transformations and Second Phases on the Strength of Ceramics," Journal of the American Ceramic Society, Vol. 63, pp. 703-710, 1980.
- [6] R. W. Rice, "Processing Induced Sources of Mechanical Failure in Ceramics," in Processing of Crystalline Ceramics, ed. by H. Palmour, III, R. F. Davis and T. M. Hare, Plenum Press, New York, pp. 303-319, 1978.
- [7] F. I. Baratta, "Stress Intensity Factor Estimates for a Peripherically Cracked Spherical Void and a Hemispherical Surface Pit," Journal of the American Ceramic Society, Vol. 61, pp. 490-493, 1978.
- [8] A. G. Evans, D. R. Biswas and R. M. Fulrath, "Some Effects of Cavities on the Fracture of Ceramics: I, Cylindrical Cavities," Journal of the American Ceramic Society, Vol. 62, pp. 95-100, 1979.
- [9] A. G. Evans, D. R. Biswas and R. M. Fulrath, "Some Effects of Cavities on the Fracture of Ceramics: II, Spherical Cavities," Journal of the American Ceramic Society, Vol. 62, pp. 101-106, 1979.
- [10] D. J. Green, "Stress Intensity Factors Estimates for Annular Cracks at Spherical Voids," Journal of the American Ceramic Society, Vol. 63, pp. 342-344, 1980.
- [11] F. I. Baratta and A. P. Parker, "Stress Intensity Factor Estimates for Various Configurations Involving Cracked Spherical Voids," in Fracture Mechanics of Ceramics, Vol. 5, ed. by R. C. Bradt, A. G. Evans, D. P. H. Hasselman and F. F. Lange, Plenum Press, New York, 1983, pp. 543-567.
- [12] R. W. Rice, "Test-Microstructural Dependence of Fracture Energy Measurements in Ceramics," in Fracture Mechanics Methods for Ceramics, ASTM Symposium on Fracture Mechanics Methods for Ceramics, Rocks and Concrete, Chicago, 1980.

- [13] R. W. Davidge and D. J. Green, "The Strength of Two-Phase Ceramic-Glass Material," Journal of Materials Science, Vol. 3, pp. 629-634, 1968.
- [14] F. F. Lange, "Criteria for Crack Extension and Arrest in Residual Localized Stress Field Associated with Second Phase Particles," in Fracture Mechanics of Ceramics, Vol. 2, ed. by R. C. Bradt, D. P. H. Hasselman and F. F. Lange, Plenum Press, 1974
- [15] A. G. Evans, "The Role of Inclusions in the Fracture of Ceramic Materials," Journal of Materials Science, Vol. 9, pp. 1145-1152, 1974.
- [16] D. J. Green, "Stress-Induced Microcracking at Second Phase Inclusion," Journal of the American Ceramic Society, Vol. 64, pp. 138-141, 1981.
- [17] Y. M. Ito and R. B. Nelson, "Numerical Modeling of Microcracking in Two-Phase Ceramics," in Fracture Mechanics of Ceramics, Vol. 5, ed. by R. C. Bradt, A. G. Evans, D. P. H. Hasselman and F. F. Lange, Plenum Press, New York, 1983, pp. 479-493.
- [18] Y. M. Ito, M. Rosenblatt, L. Y. Cheng, F. F. Lange, and A. G. Evans, "Cracking in Particulate Composites due to Thermomechanical Stress," International Journal of Fracture, Vol. 27, pp. 483-491, 1981.
- [19] B. R. Lawn and T. R. Wilshaw, "Review - Indentation Fracture: Principle and Applications," Journal of Materials Science, Vol. 10, pp. 1049-1081, 1975.
- [20] A. G. Evans, "Fracture Toughness: The Role of Indentation Technique," Fracture Mechanics Applied to Brittle Materials, ASTM STP 678, S. W. Freiman, Ed., American Society for Testing and Materials, pp. 112-135, 1979.
- [21] F. Erdogan and G. D. Gupta, "The Inclusion Problem with a Crack Crossing the Boundary", International Journal of Fracture, Vol. 11, pp. 13-27, 1975.
- [22] F. Erdogan, "Mixed Boundary Value Problems," in Mechanics Today, Vol. 4, ed. by S. Nemat-Nasser, Pergamon Press, Oxford, 1978, pp. 1-30.
- [23] D. B. Marshall and A. G. Evans, "Failure Mechanisms in Ceramic-Fiber/Ceramic-Matrix Composites", Journal of the American Ceramic Society, Vol. 68, pp. 225-231, 1985.
- [24] F. Erdogan, G. D. Gupta and T. S. Cook, "Numerical Solution of Singular Integral Equations," Mechanics of Fracture, Vol. 1: Methods of Analysis and Solutions of Crack Problems, ed. by G. C. Sih, Noordhoff, Leyden, The Netherlands, 1973, pp. 368-425.

- [25] N. I. Ioakimidis and P. S. Theocaris, "On the Solution of Collocation Points for the Numerical Solution of Singular Integral Equations with Generalized Kernels Appearing in Elasticity Problems," Computers and Structures, Vol. 11, pp. 289-295, 1980.
- [26] A. H. England, "A Crack Between Dissimilar Media," Journal of Applied Mechanics, Vol. 32, pp. 400-402, 1965.
- [27] F. Erdogan, "Stress Distribution in Bonded Dissimilar Materials with Cracks," Journal of Applied Mechanics, Vol. 32, pp. 403-410, 1965.
- [28] F. Erdogan and G. D. Gupta, "The Stress Analysis of Multi-Layered Composites with a Flaw," International Journal of Solids and Structures, Vol. 7, pp. 39-61, 1971.
- [29] M. L. Williams, "The Stress around a Fault or Crack in Dissimilar Media," Bulletin of the Seismological Society of America, Vol. 49, pp. 199-204, 1959.
- [30] G. P. Cherepanov, Mechanics of Brittle Fracture, McGraw-Hill, New York, 1979.
- [31] M. Toya, "A Crack Along the Interface of a Circular Inclusion Embedded in an Infinite Solid", Journal of the Mechanics and Physics of Solids, Vol. 22, pp. 325-348, 1974.
- [32] J. N. Goodier, Journal of Applied Mechanics, Vol. 1, p. 39, 1933.
- [33] ANSYS, Swanson Analysis System, Inc.
- [34] R. W. Little, Elasticity, Prentice-Hall, Englewood Cliffs, NJ, 1973.
- [35] D. H. Grande, J. F. Mandell and K. C. C. Hong, "Fibre-Matrix Bond Strength Studies of Glass, Ceramic, and Metal Matrix Composites," Journal of Materials Science, Vol. 23, pp. 311-328, 1988.
- [36] ABAQUS, Hibbit, Karlsson & Sorensen, Inc., Providence, RI.

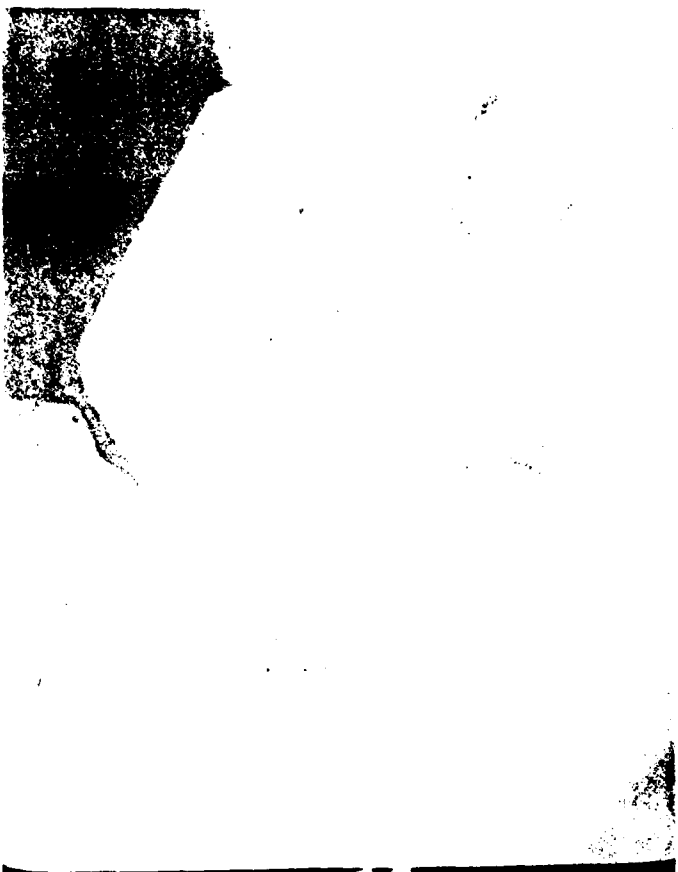


PHOTO 1 Isolated Fiber

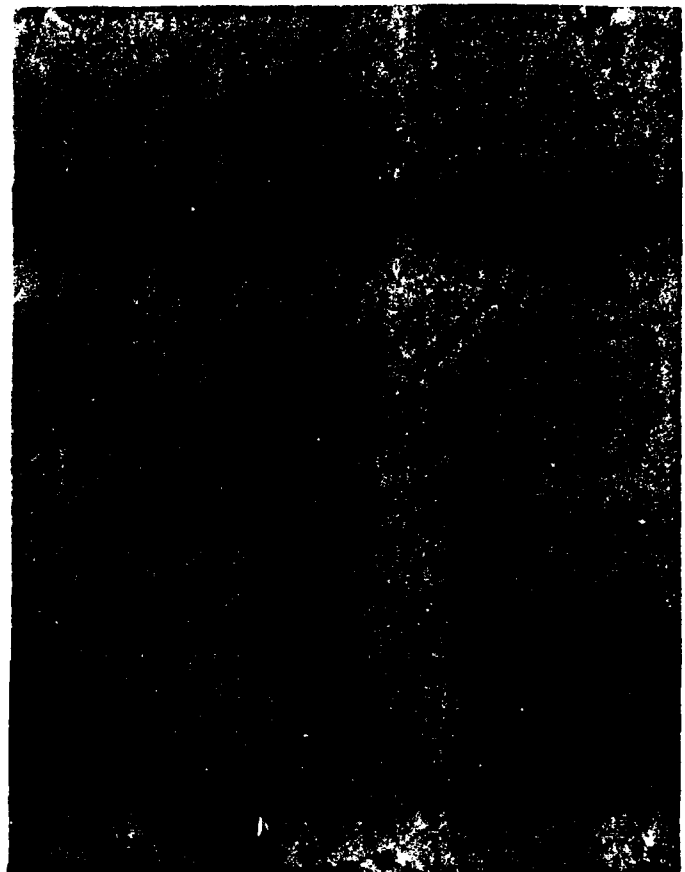


PHOTO 2 Two Isolated Fibers



PHOTO 3 Fiber Surrounded by an array of fibers

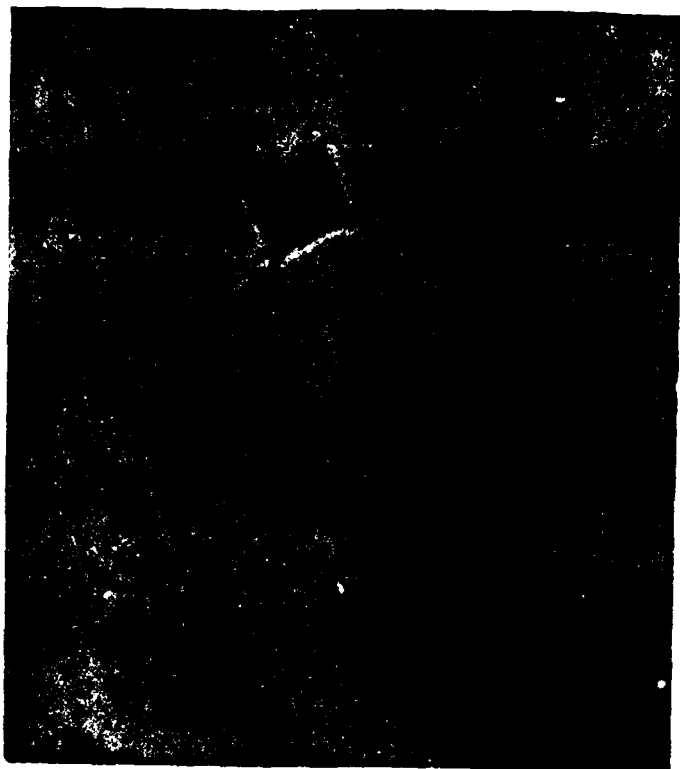


PHOTO 4. Matrix cracks

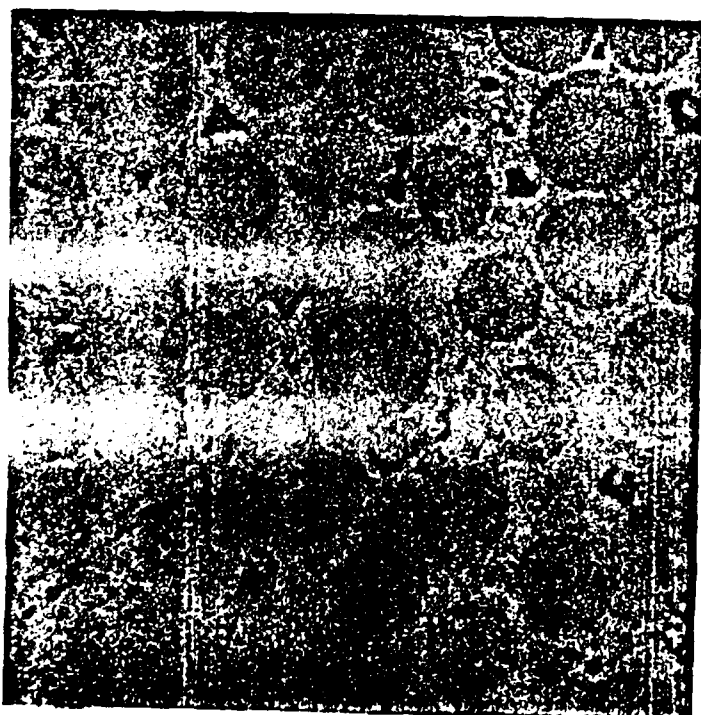


PHOTO 5. Partial Debonding Along
Fiber/Matrix Interface



PHOTO 6. Complete Debonding Along
Fiber/Matrix Interface

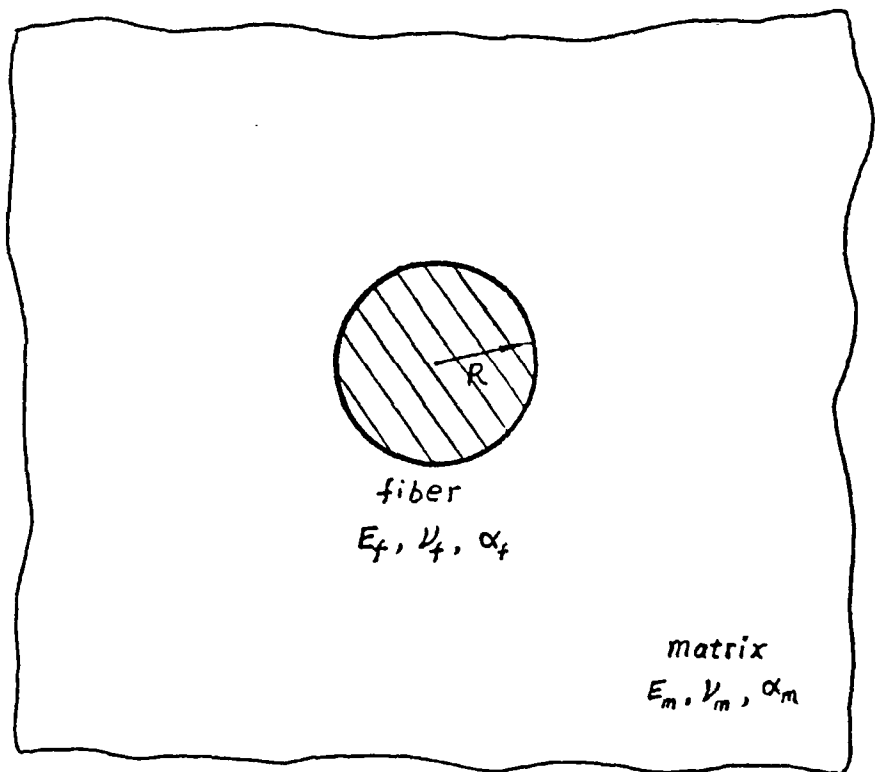


Figure 2. Geometry of a single fiber embedded in infinite matrix.

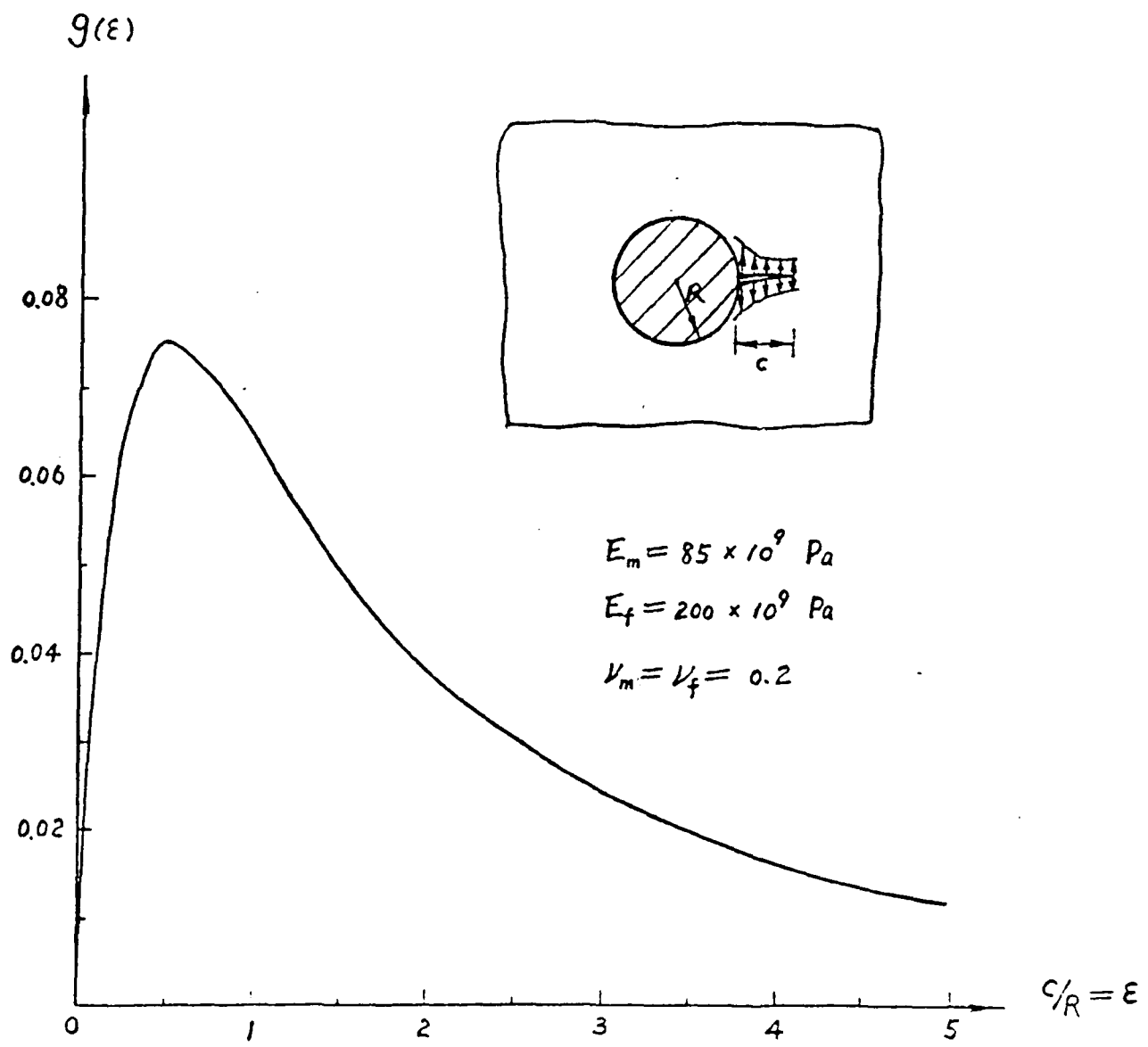


Figure 3. Variations of the normalized strain energy release rate $g(\epsilon)$ with c/R .

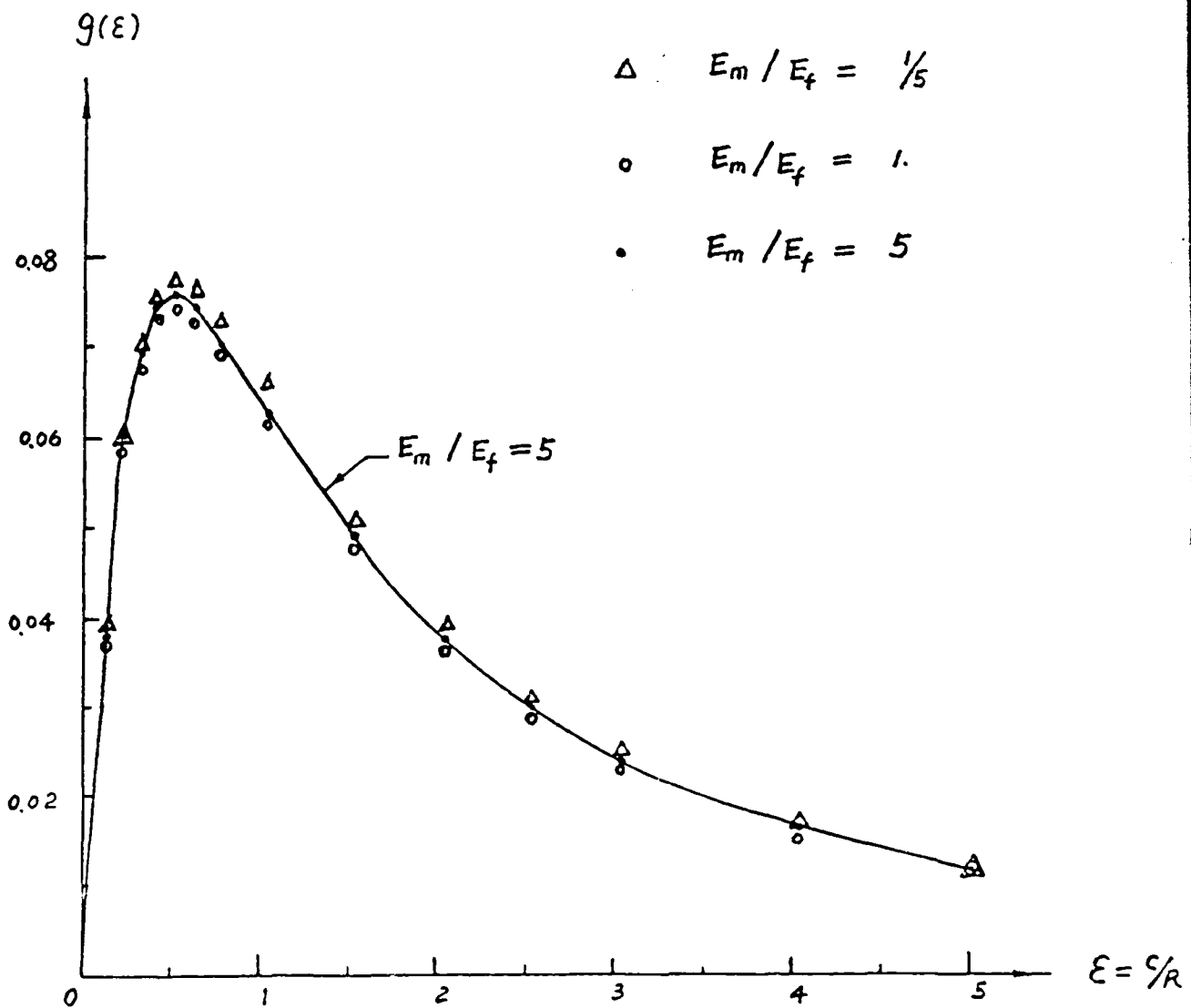


Figure 4. Variations of $g(\epsilon)$ with c/R for variations ratios of E_m/E_f .

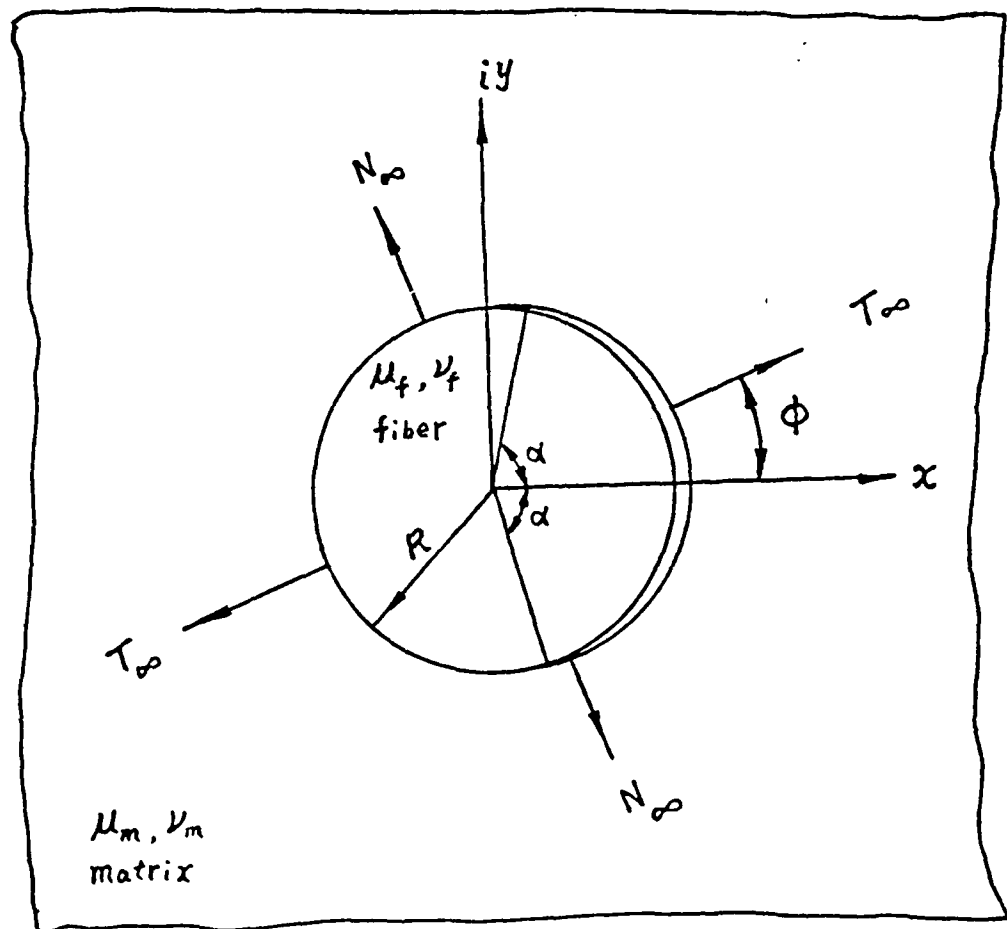


Figure 5. Interface crack under plane loading.

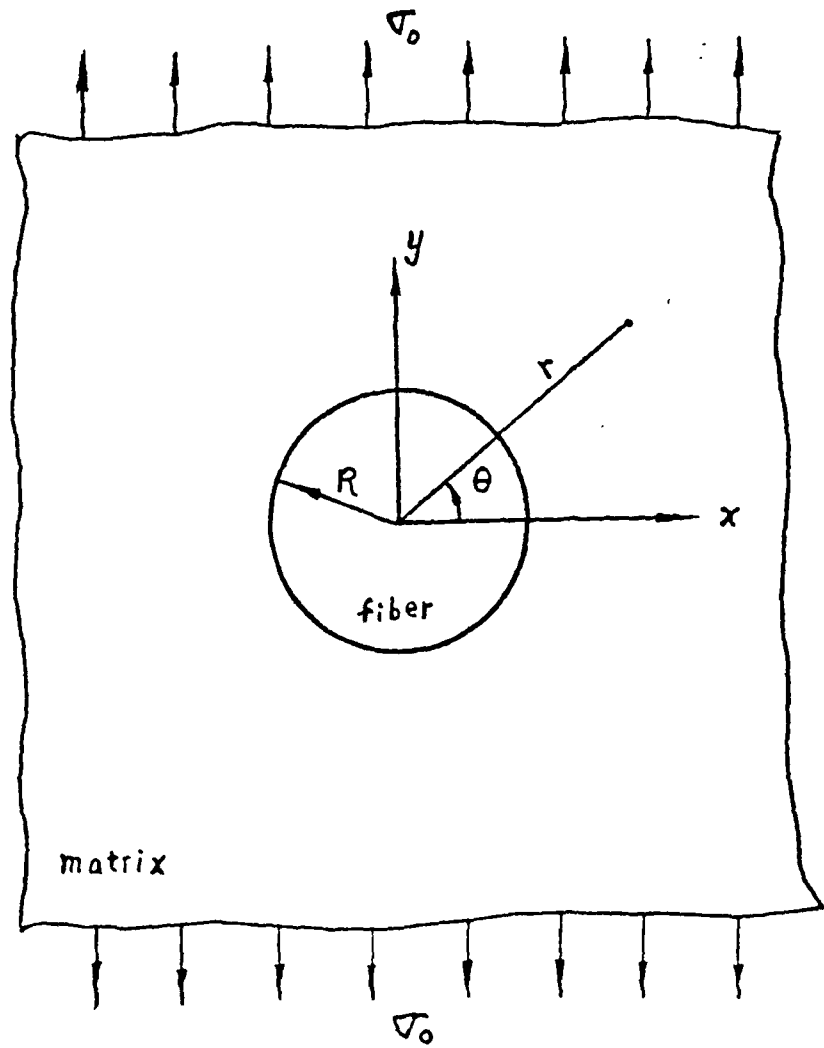
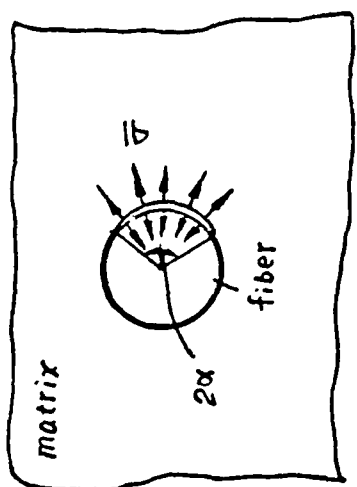


Figure 6. Uniaxial loading of a fiber/matrix system.



$$\begin{aligned}E_m &= 85 \times 10^9 \text{ Pa} \\E_f &= 200 \times 10^9 \text{ Pa} \\v_m = v_f &= 0.2\end{aligned}$$

plane strain

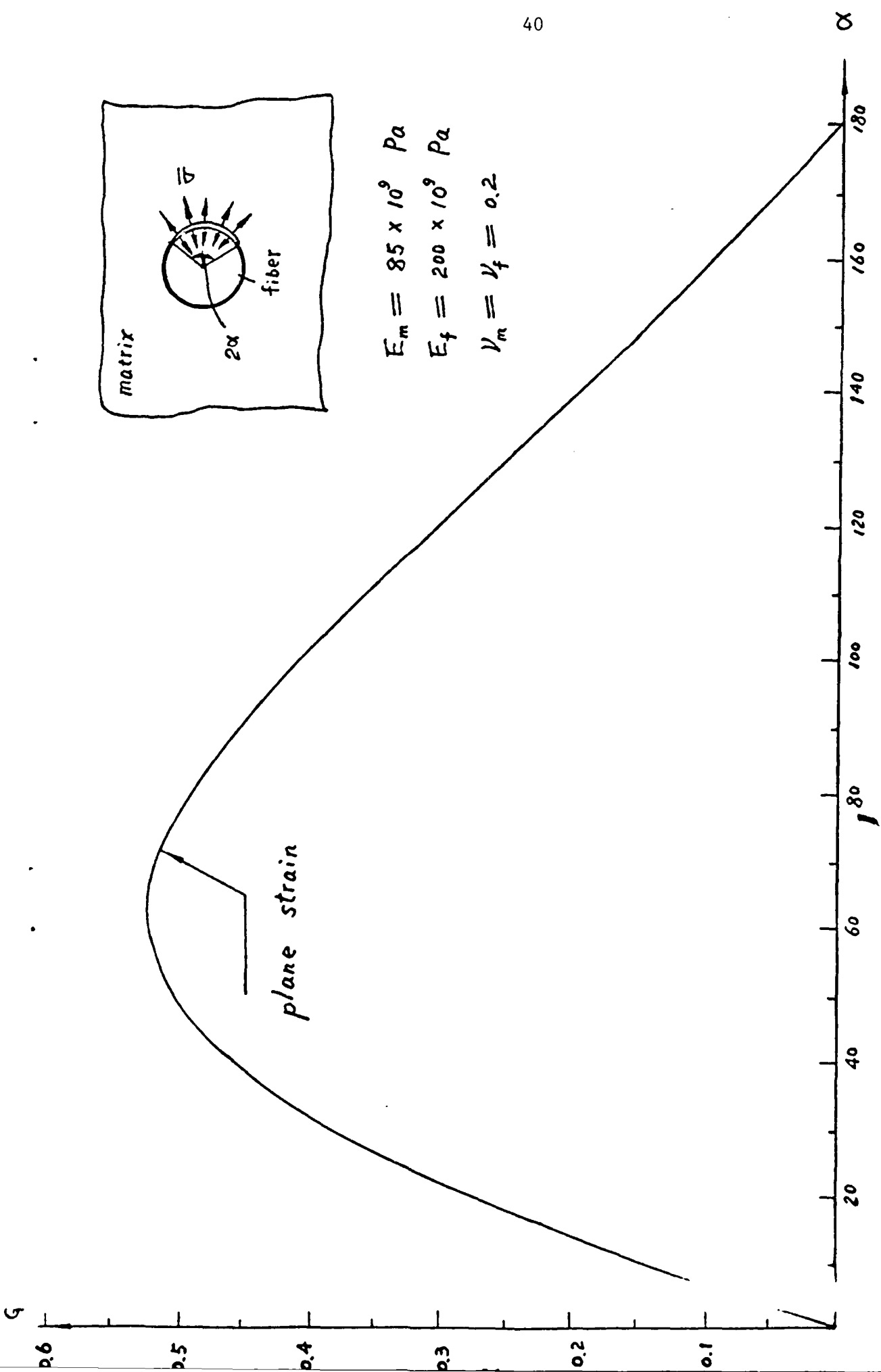


Figure 7. Variation of the normalized strain energy release rate G' with the crack angle α .

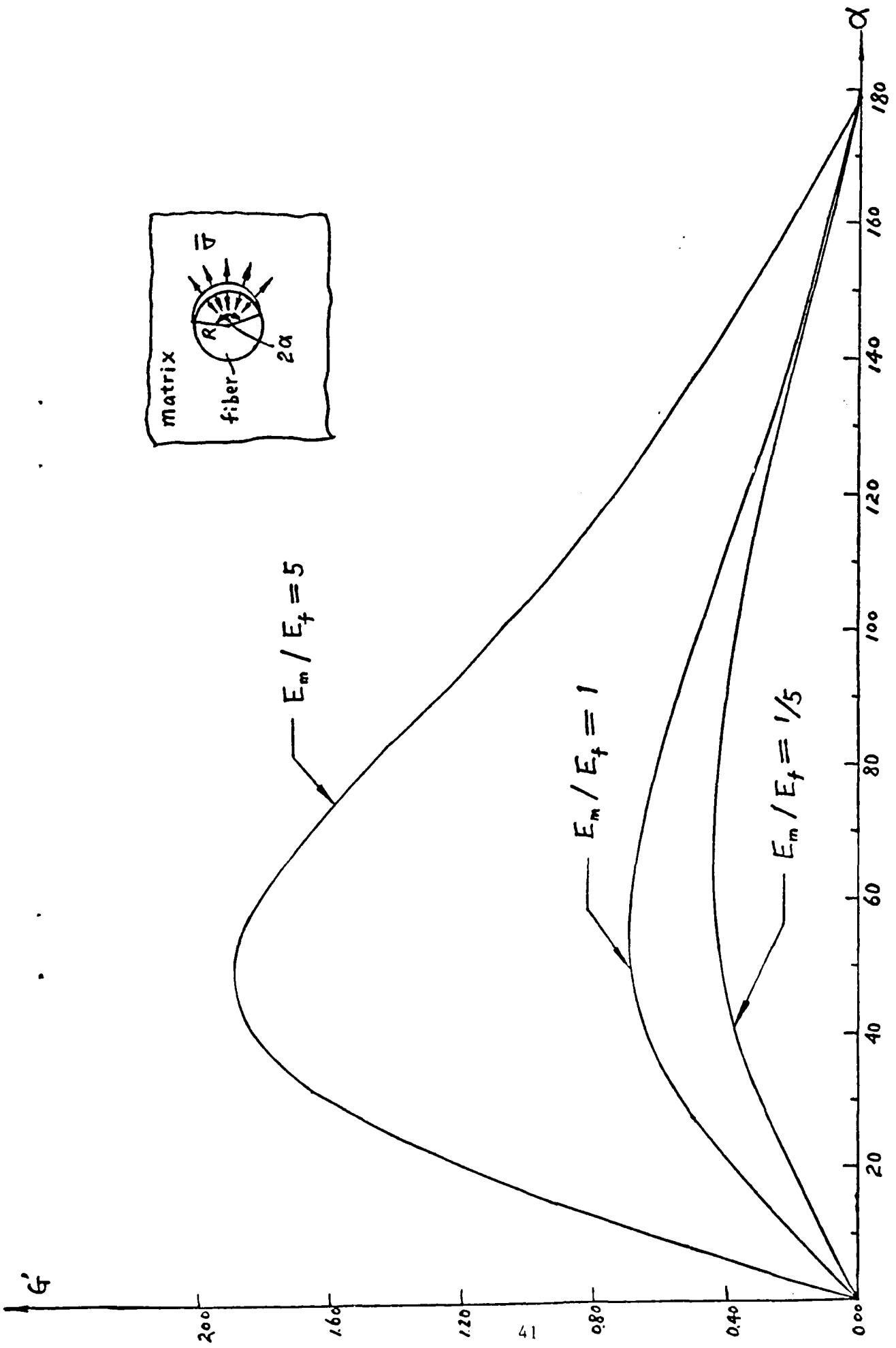
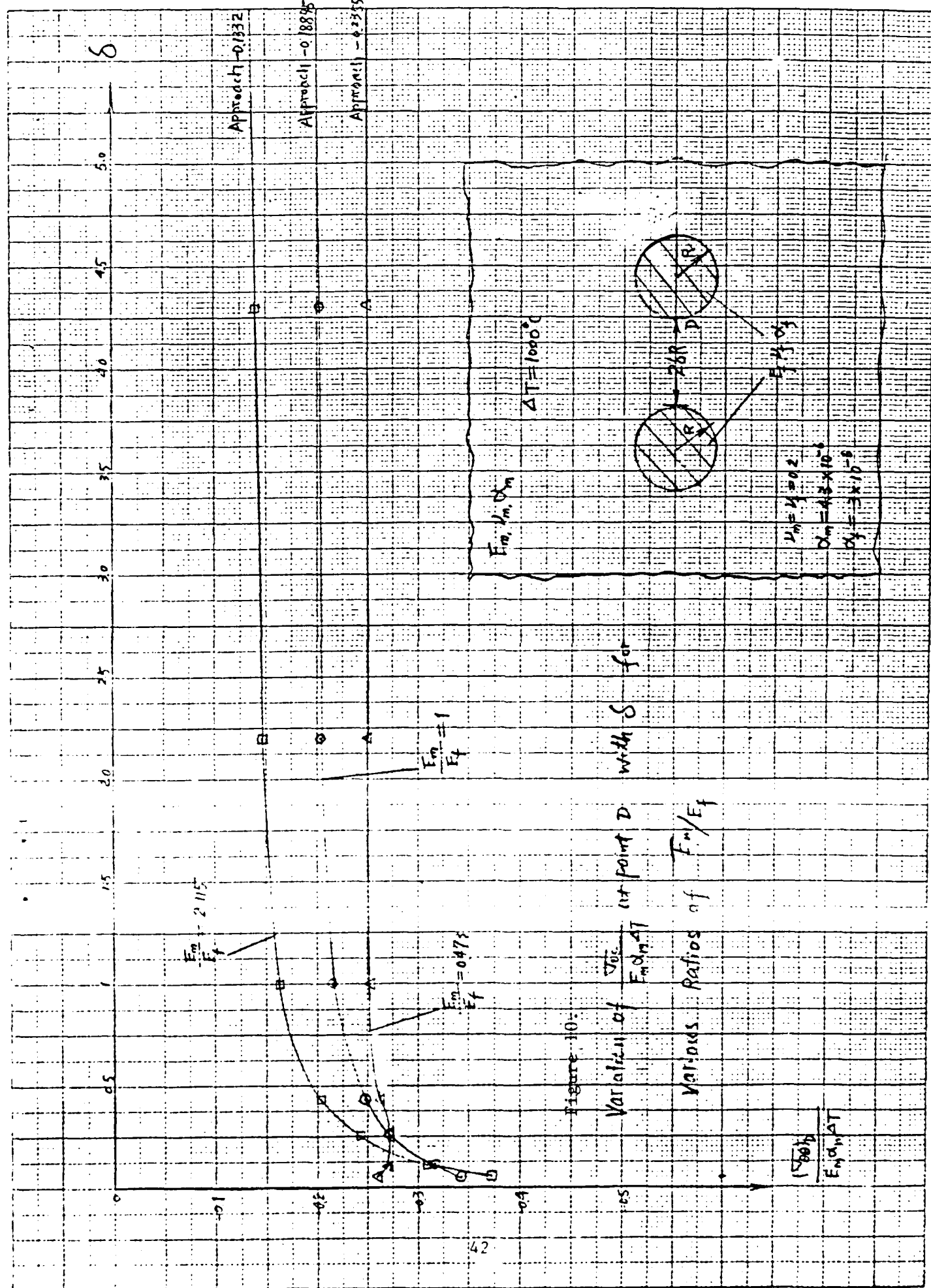


Figure 8. Variation of G' with the interface crack angle α for various values of the ratio E_m/E_f .



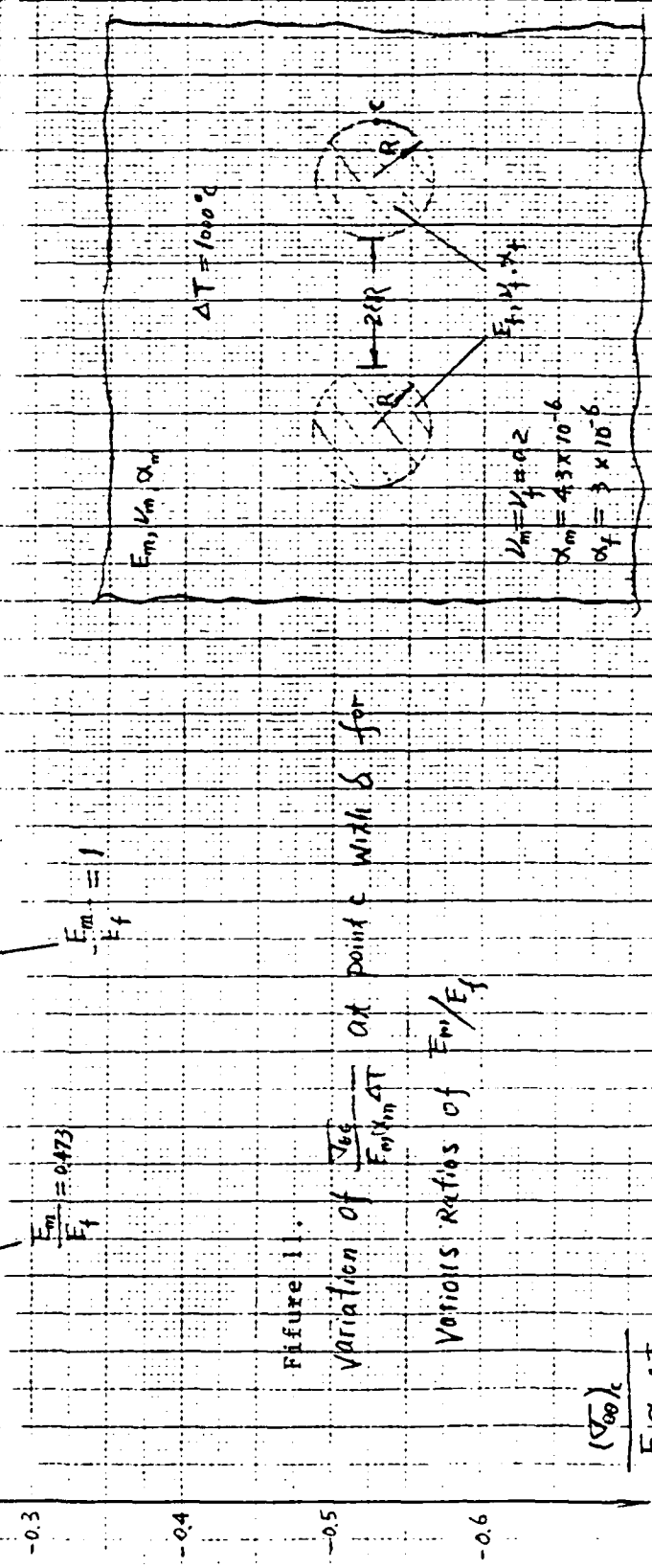
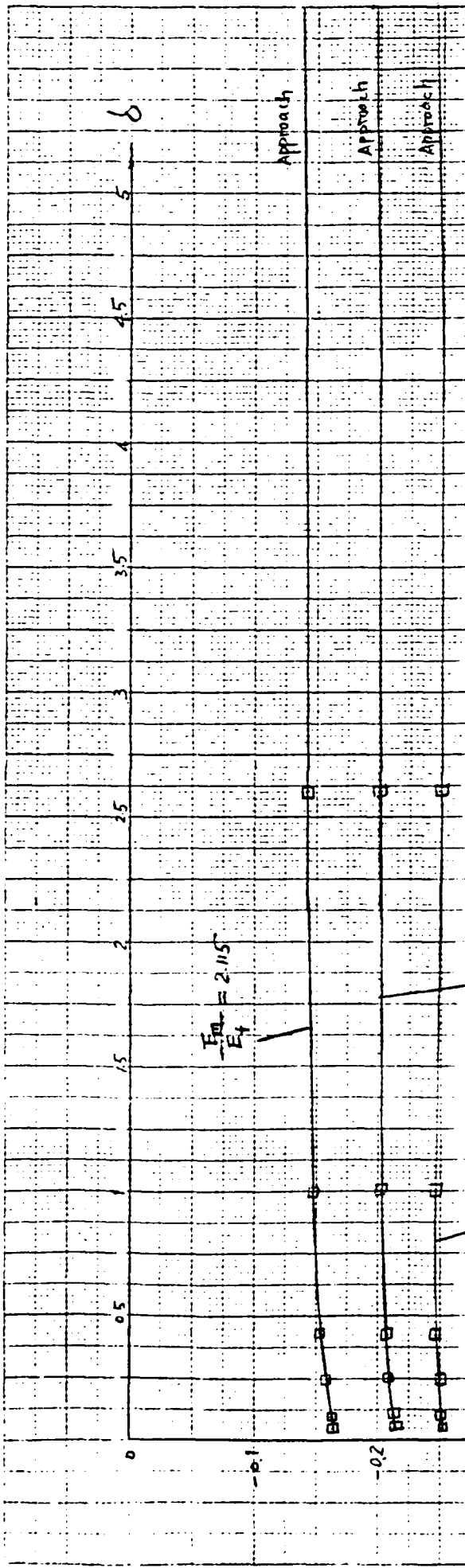


Figure 1.

Variation of $\frac{E_{mn}}{E_f}$ at point c with c for various ratios of E_m/E_f

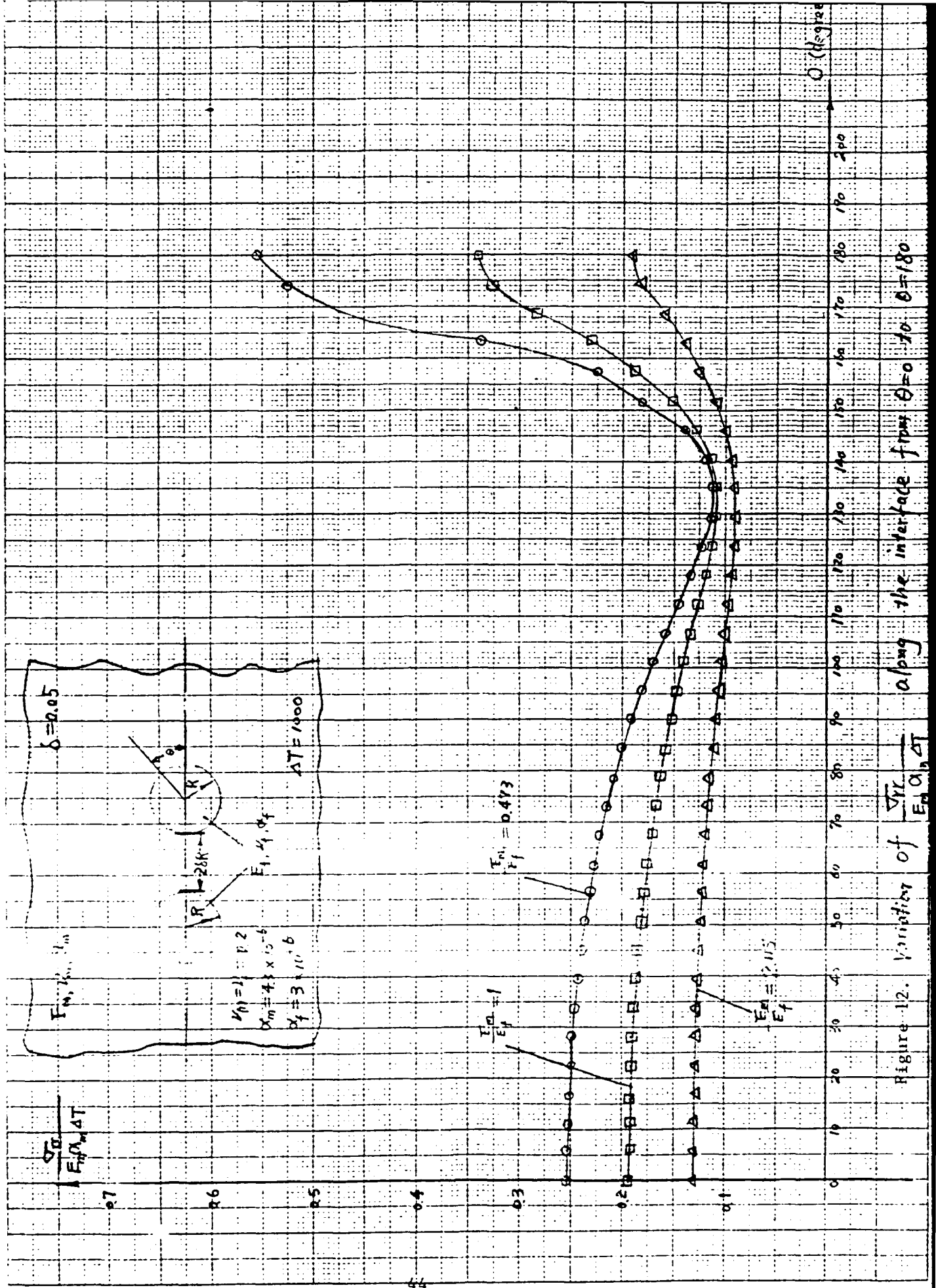


Figure 12. Variation of $\sqrt{\frac{G}{G_0}} * 4T$ along the interface between E_0, G_0 and E_f, G_f .

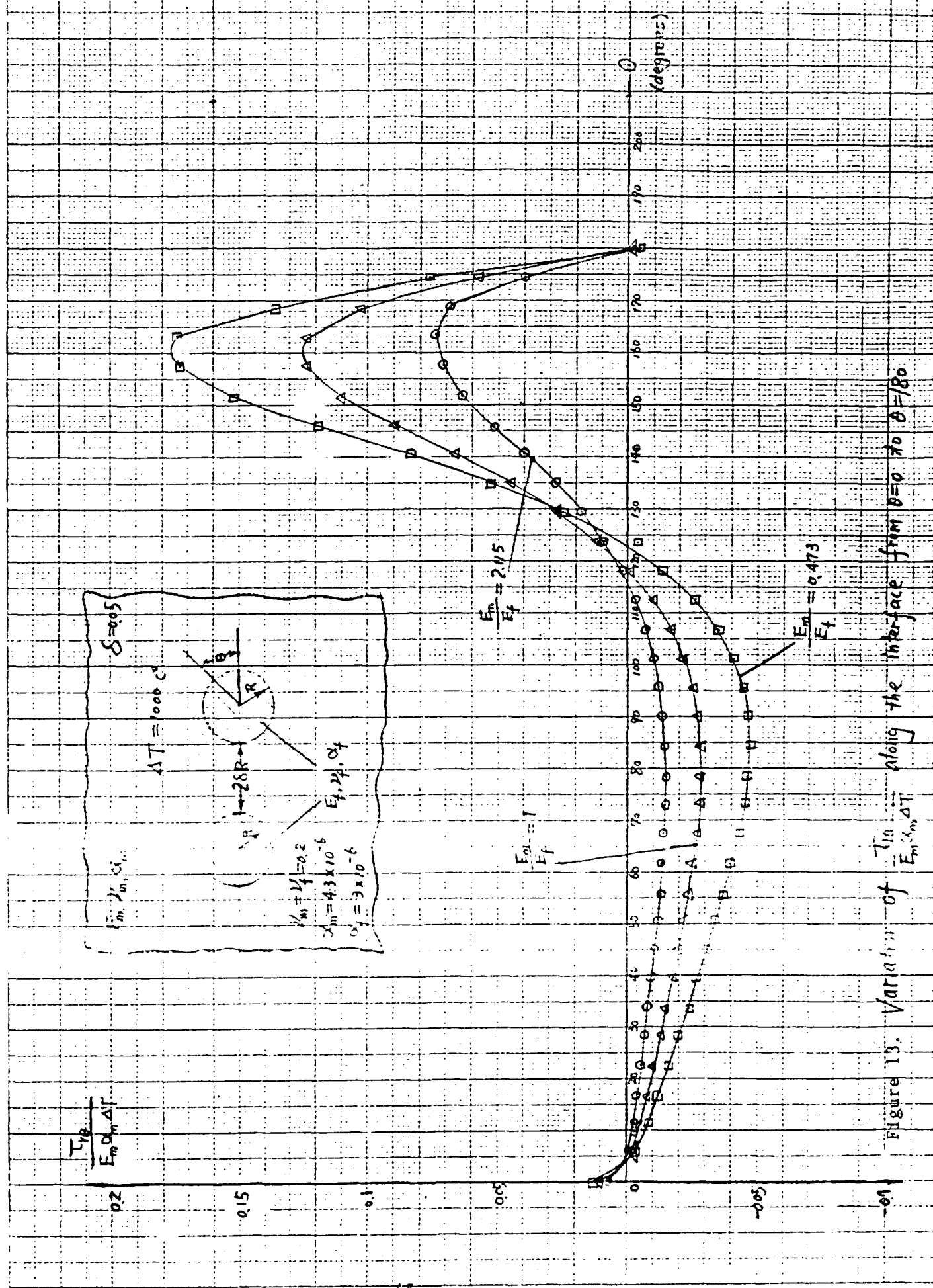


Figure 13. Variation of the interface along the interface from $\theta = 0$ to 270°

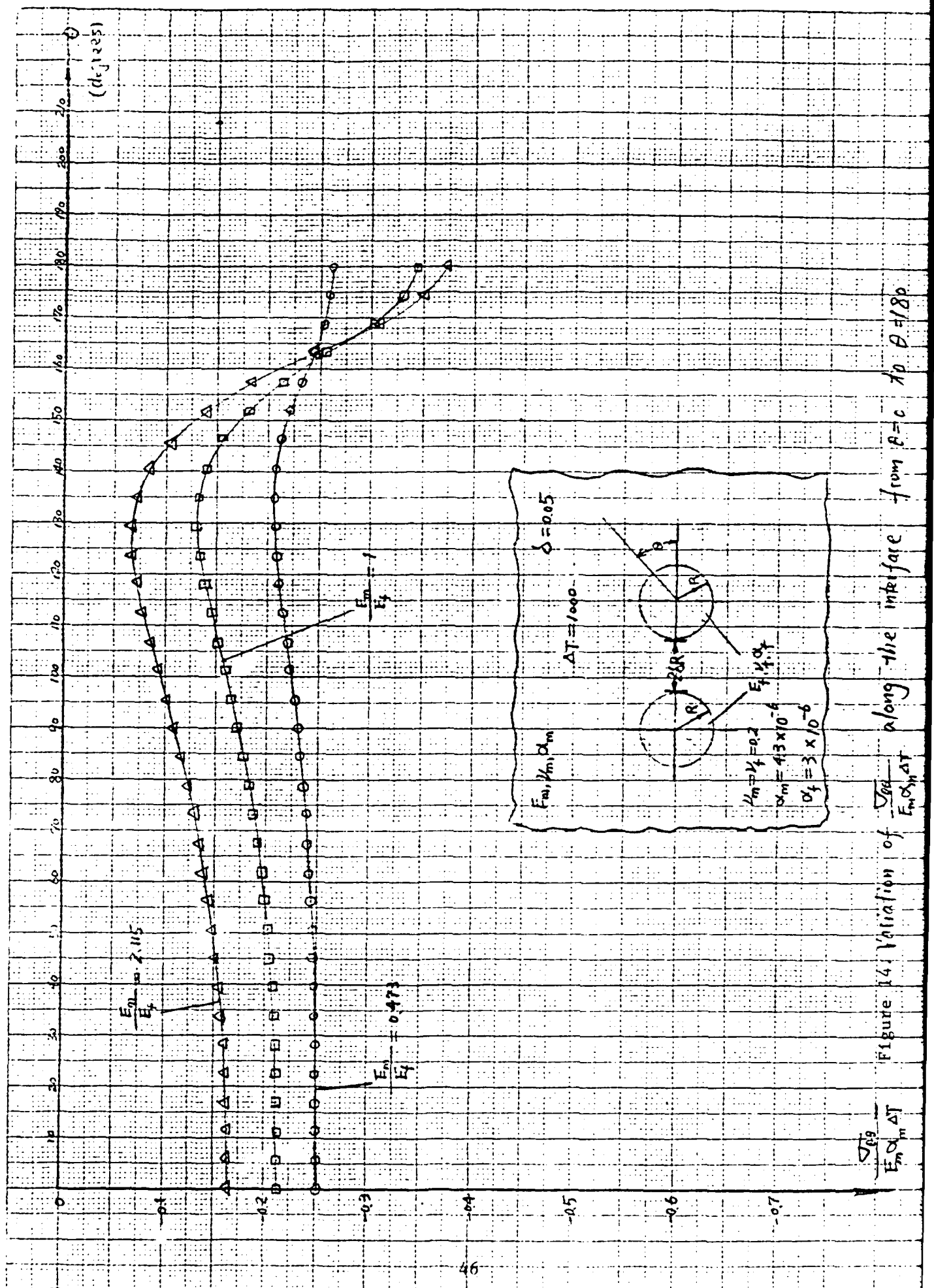


Figure 14. Variation of $\frac{E_m}{E_m + d_m}$ along the infarce from $\theta = 0^\circ$ to $\theta = 180^\circ$

$$\frac{\Delta T}{E_m / (E_m + d_m)}$$

Figure 15.
Variation of the
 E_m vs ΔT
with the
ratios of
 E_m/E_f

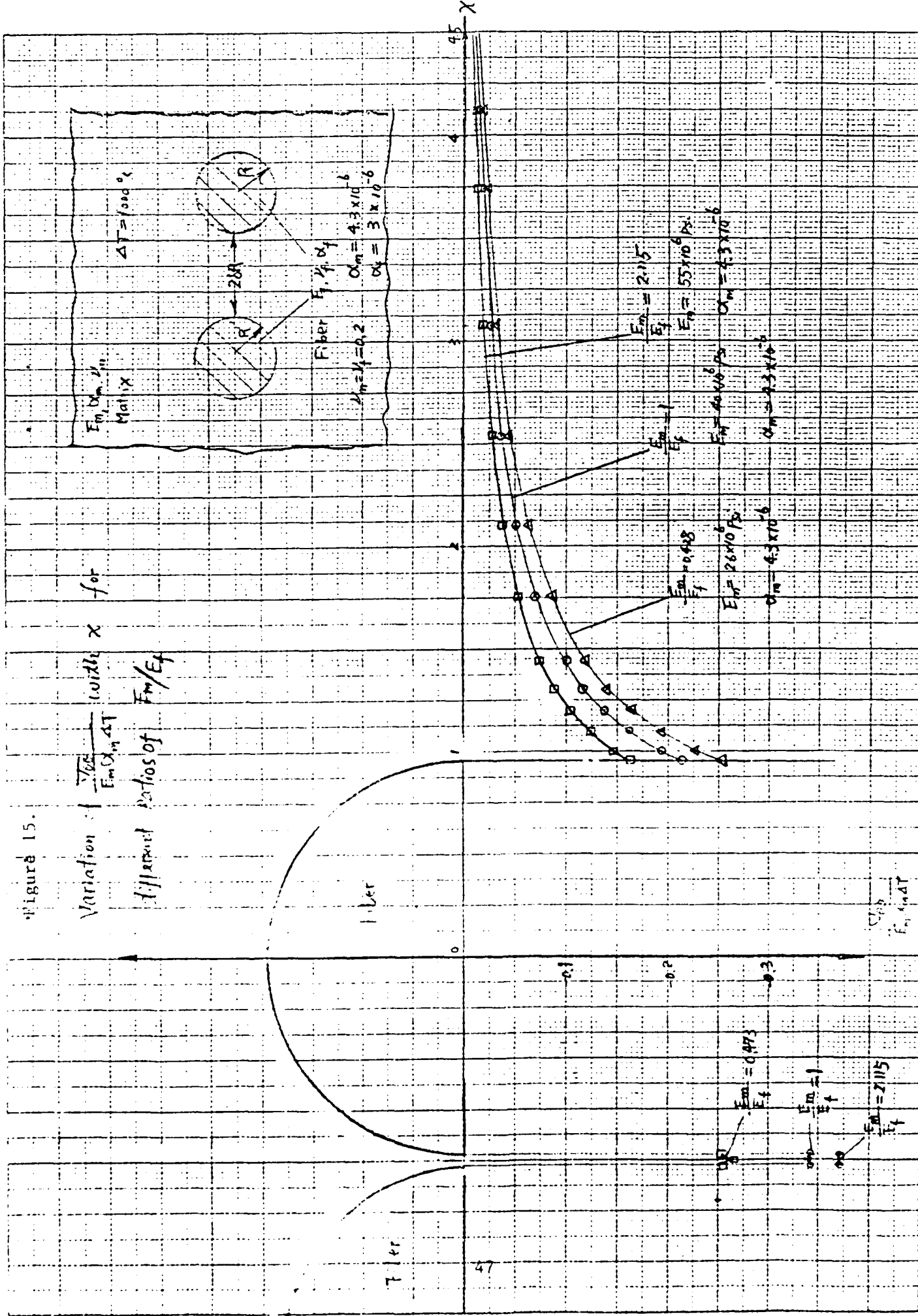
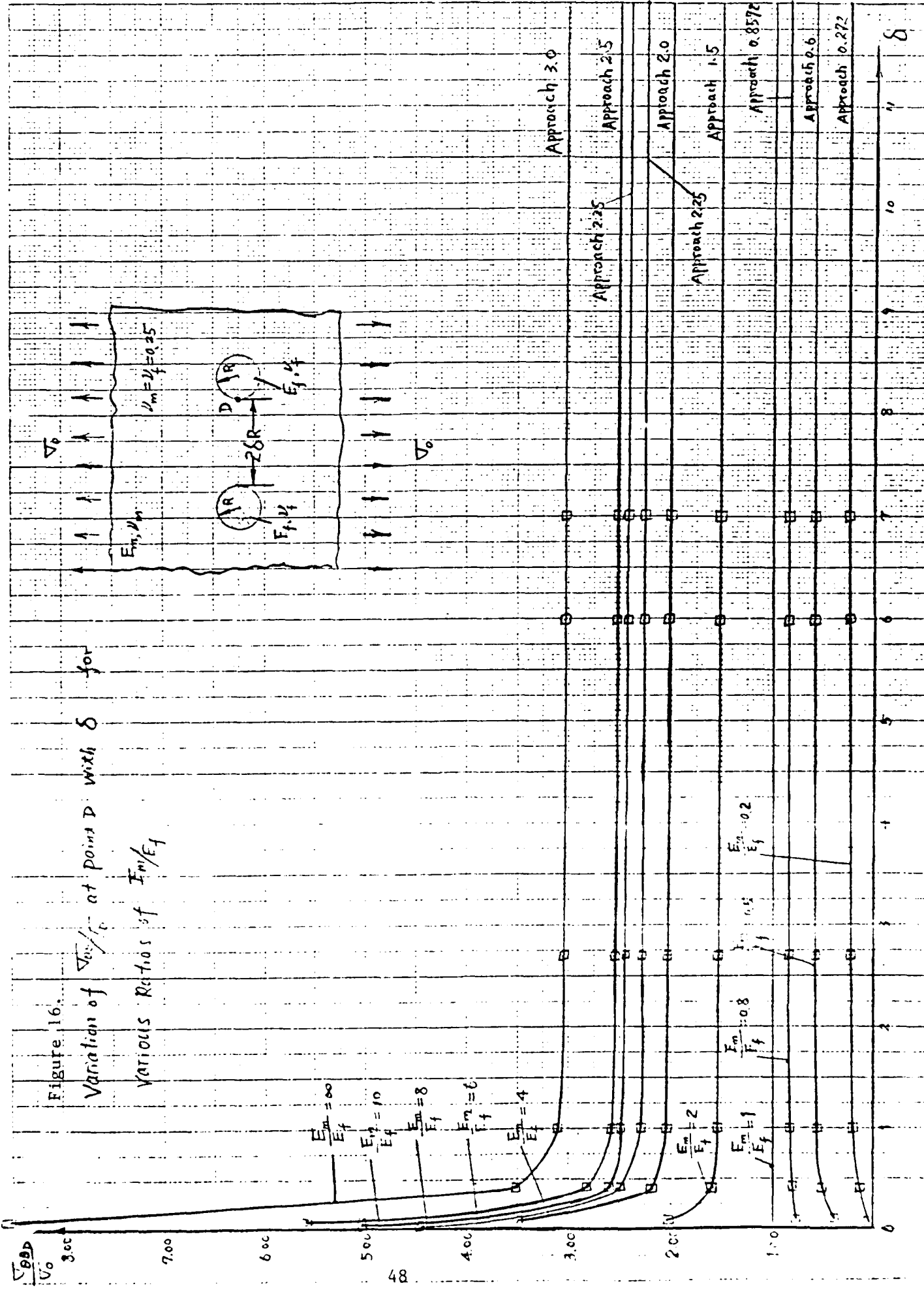


Figure 16.

Variation of $\frac{\nabla_{BD}}{\nabla_0}$ at point D with S for various ratios of E_m/E_f



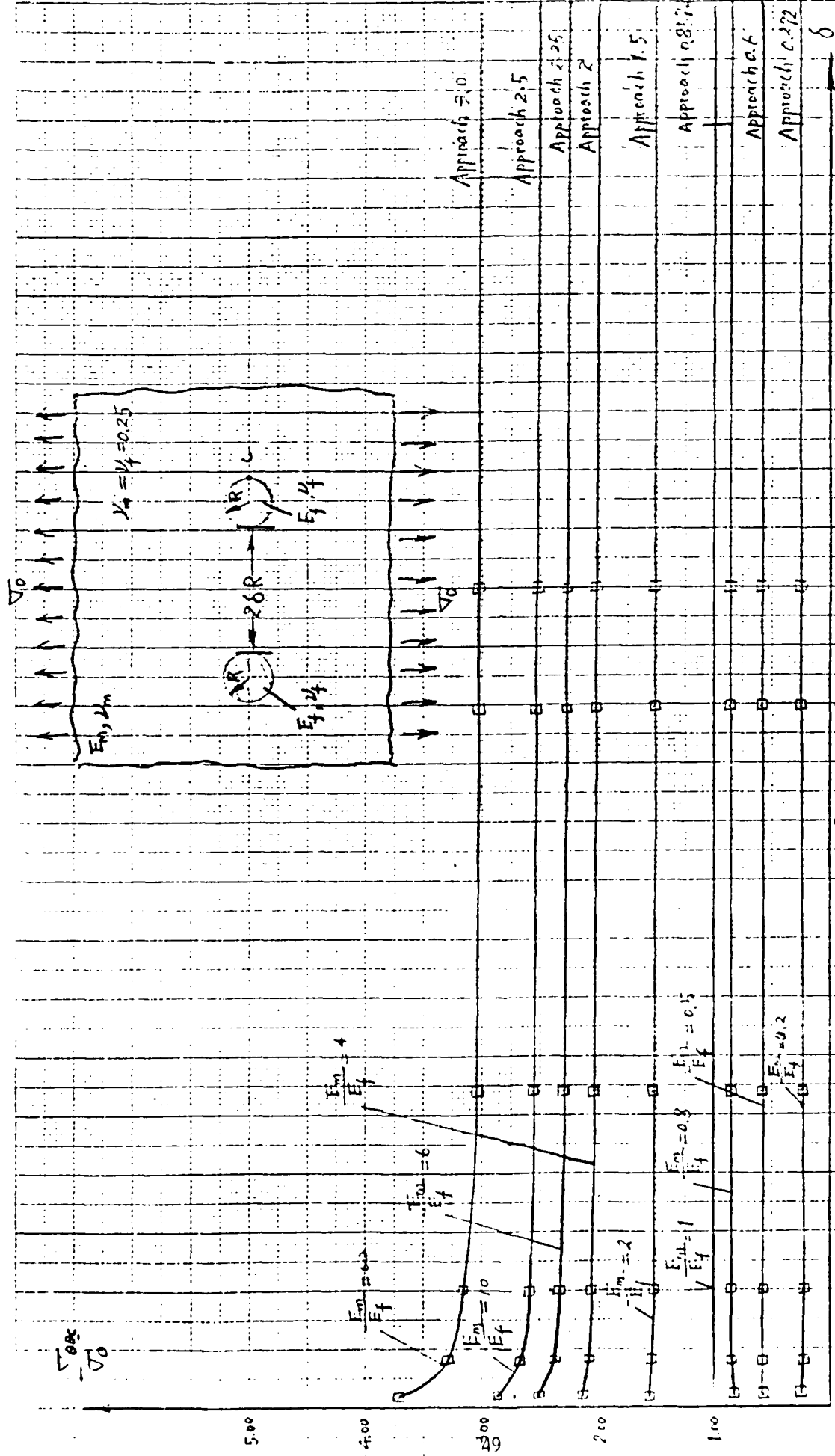


Figure 17. Variation of $\frac{E_m}{E_f}$ with S for various ratios of E_m/E_f at point C

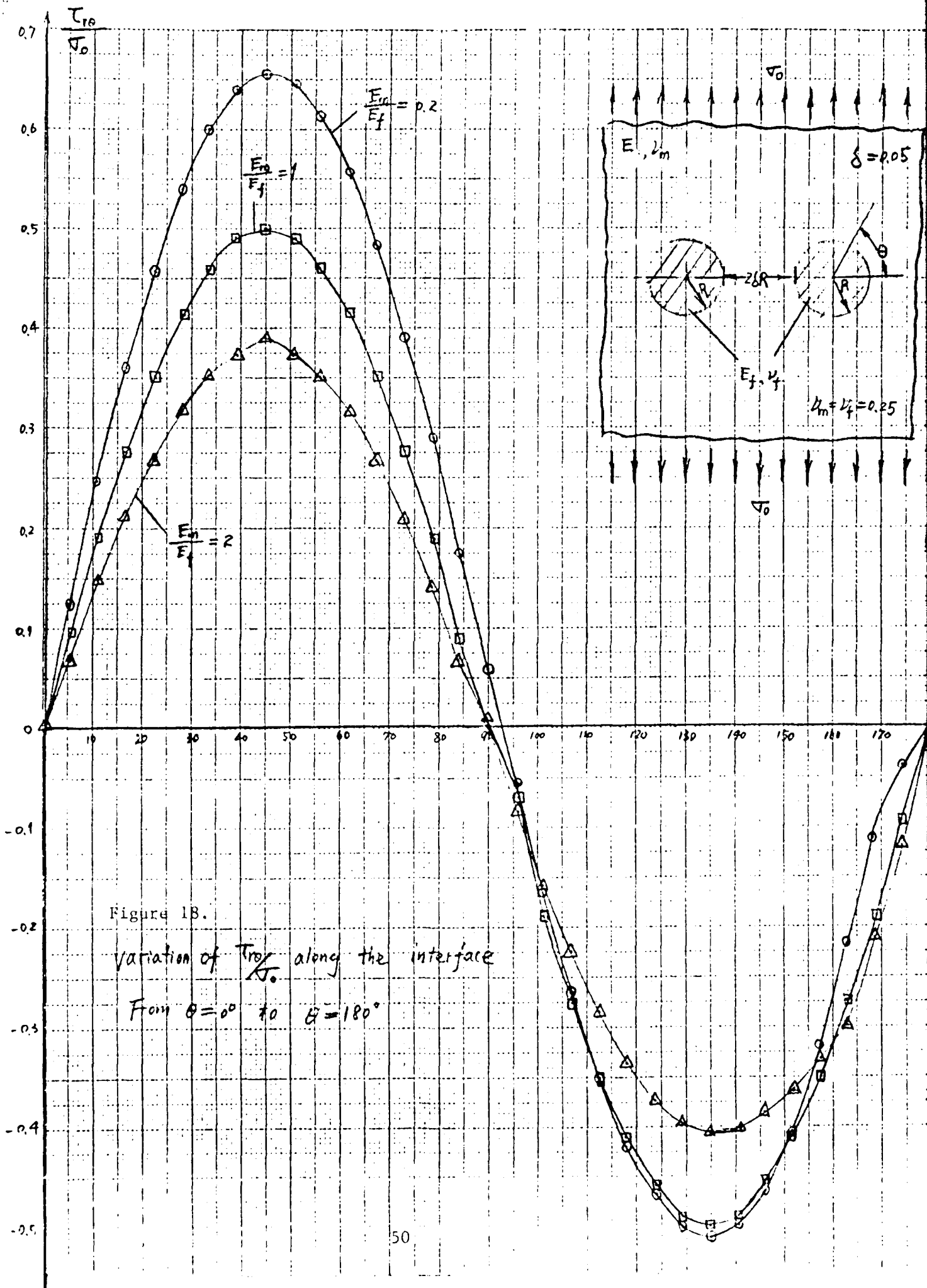


Figure 18.

variation of T_{f0}/T_0 along the interface

From $\theta = 0^\circ$ to $\theta = 180^\circ$

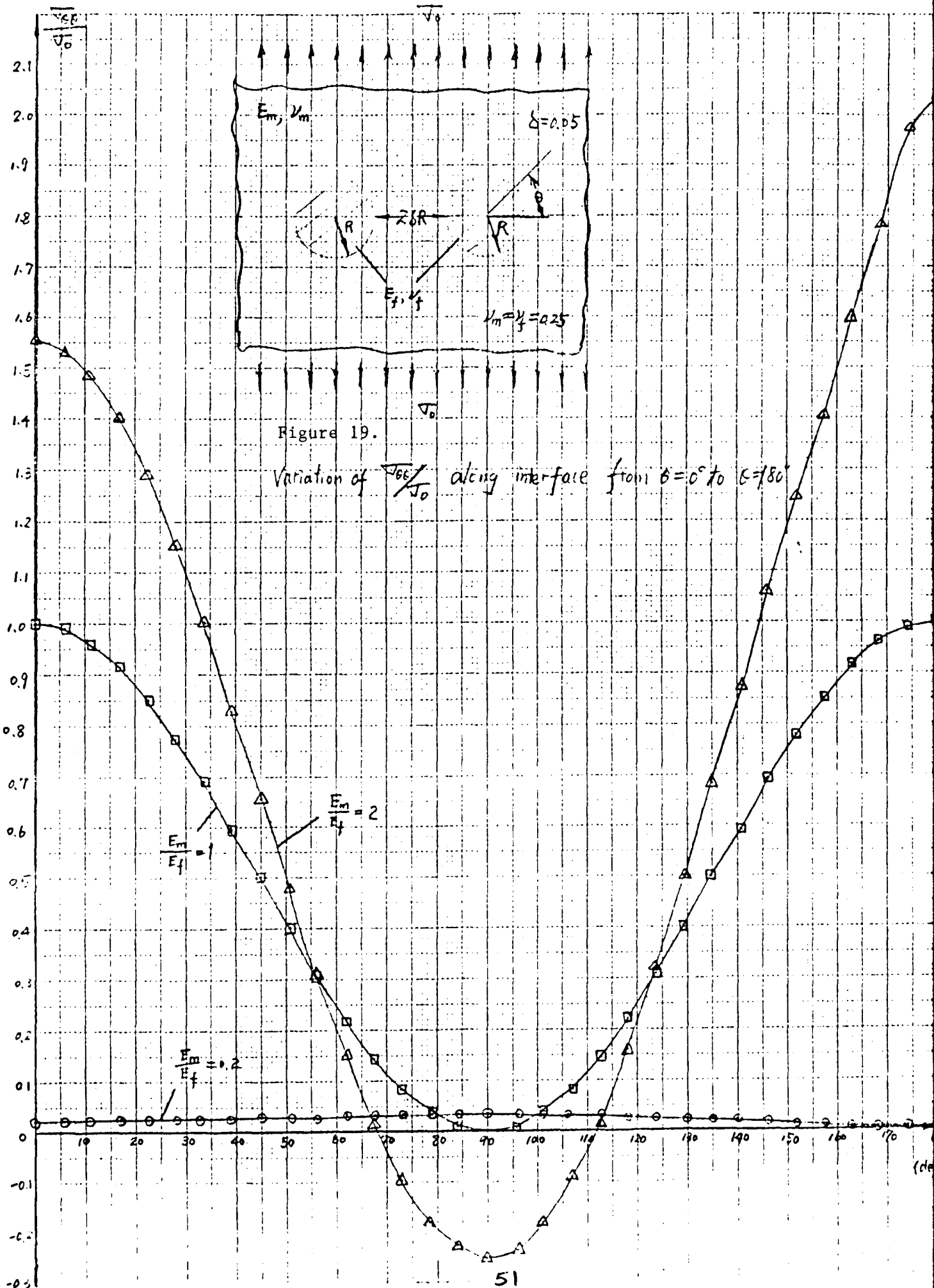
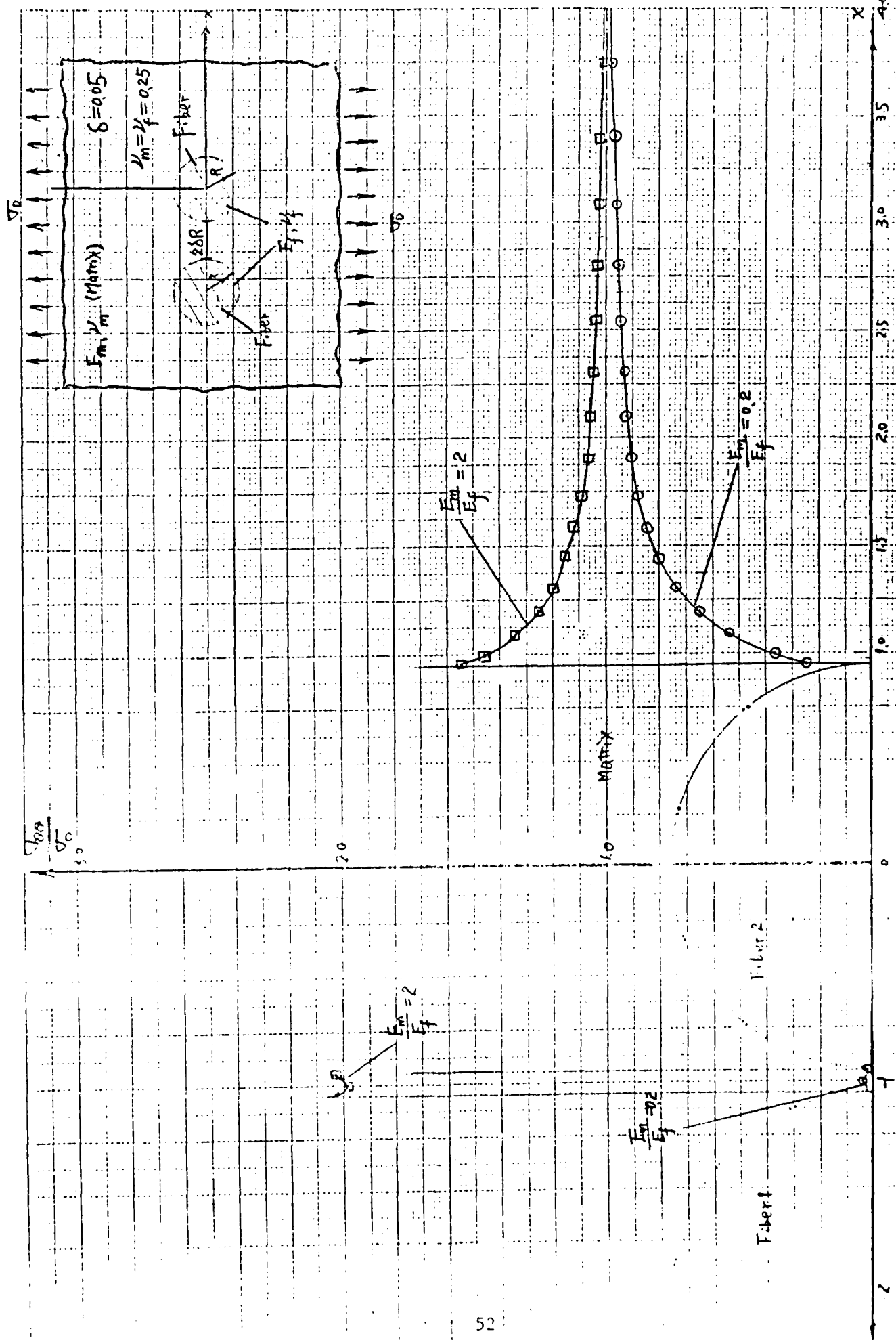
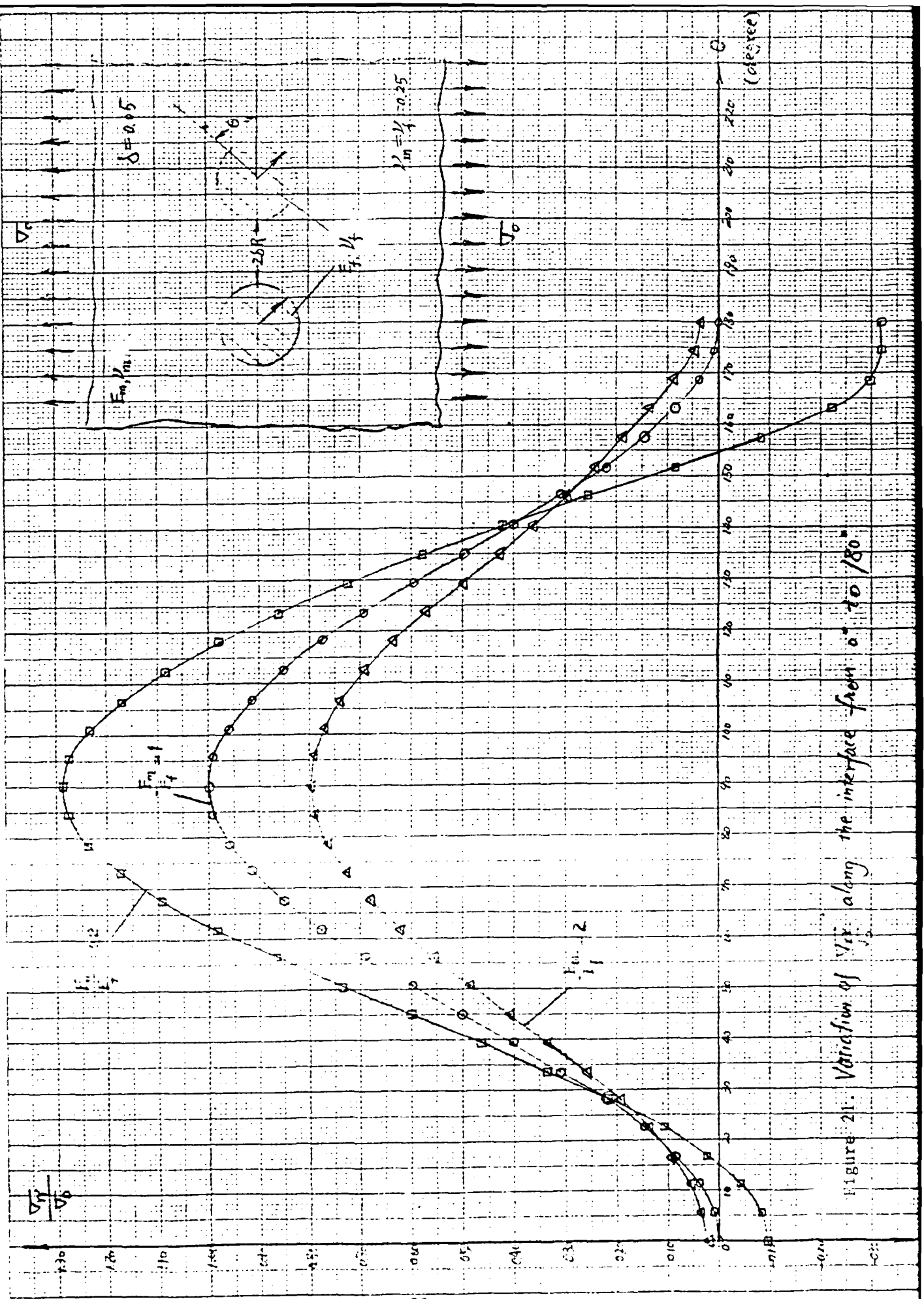


Figure 20. Variation of $\frac{\sigma_{60}}{\sigma_0}$ with X for variation of ratios of E_m/E_f





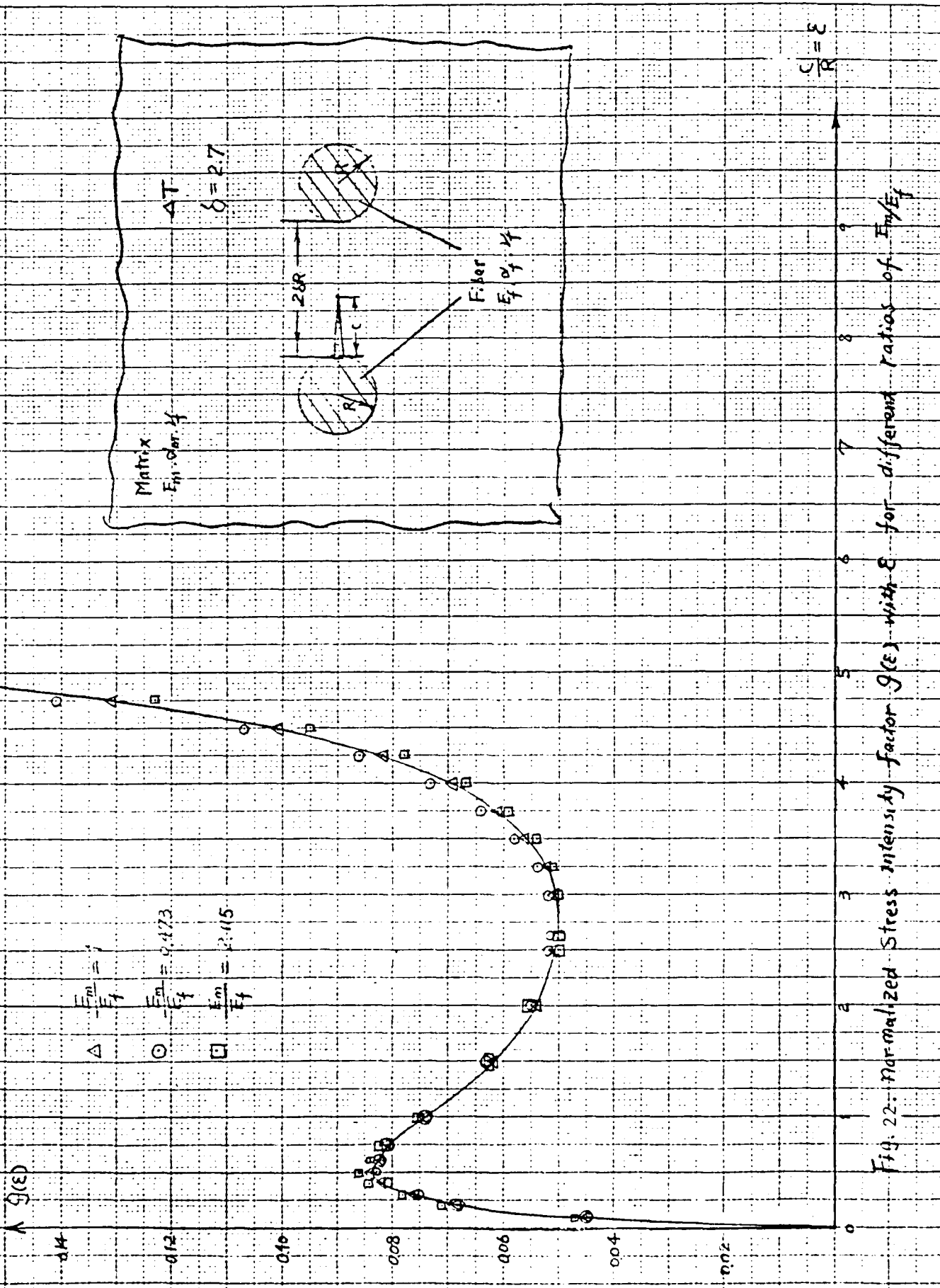


Fig. 22: Normalized Stress Intensity factor $g(\epsilon)$ with ϵ for different ratios of E_m/E_f

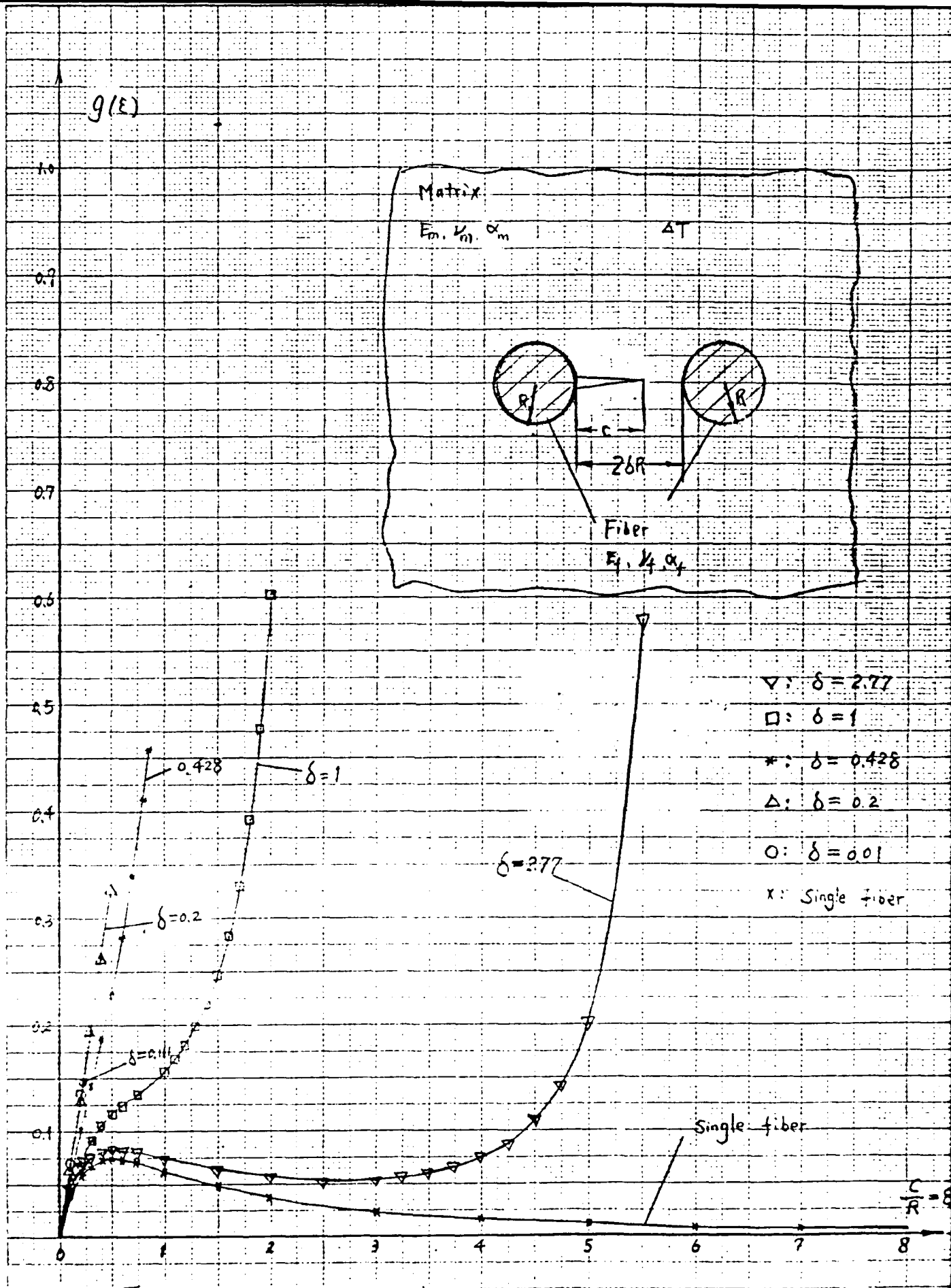


Fig. 23. Variations of the normalized strain energy release rate $g(\epsilon)$ with C/R for different δ

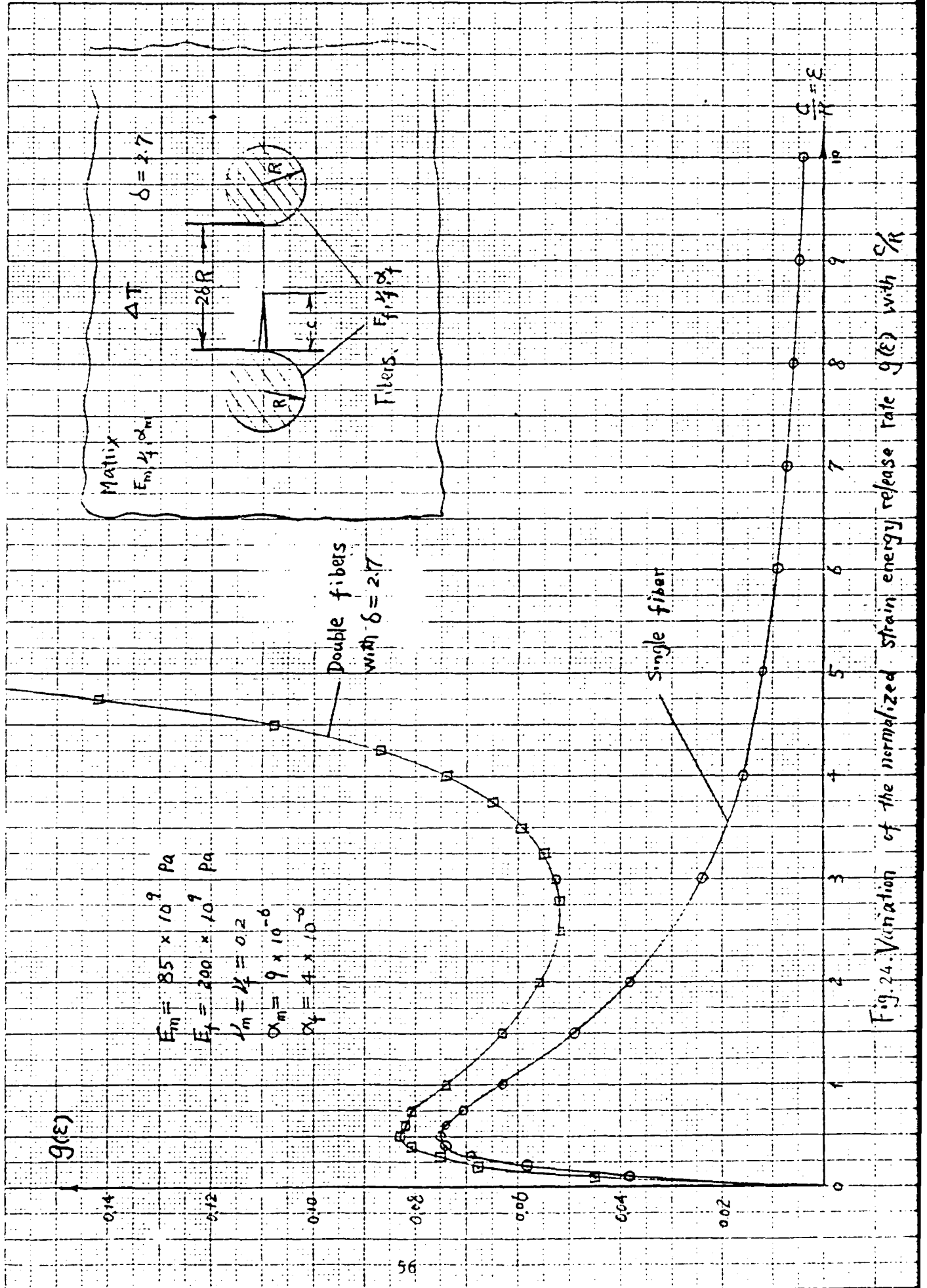
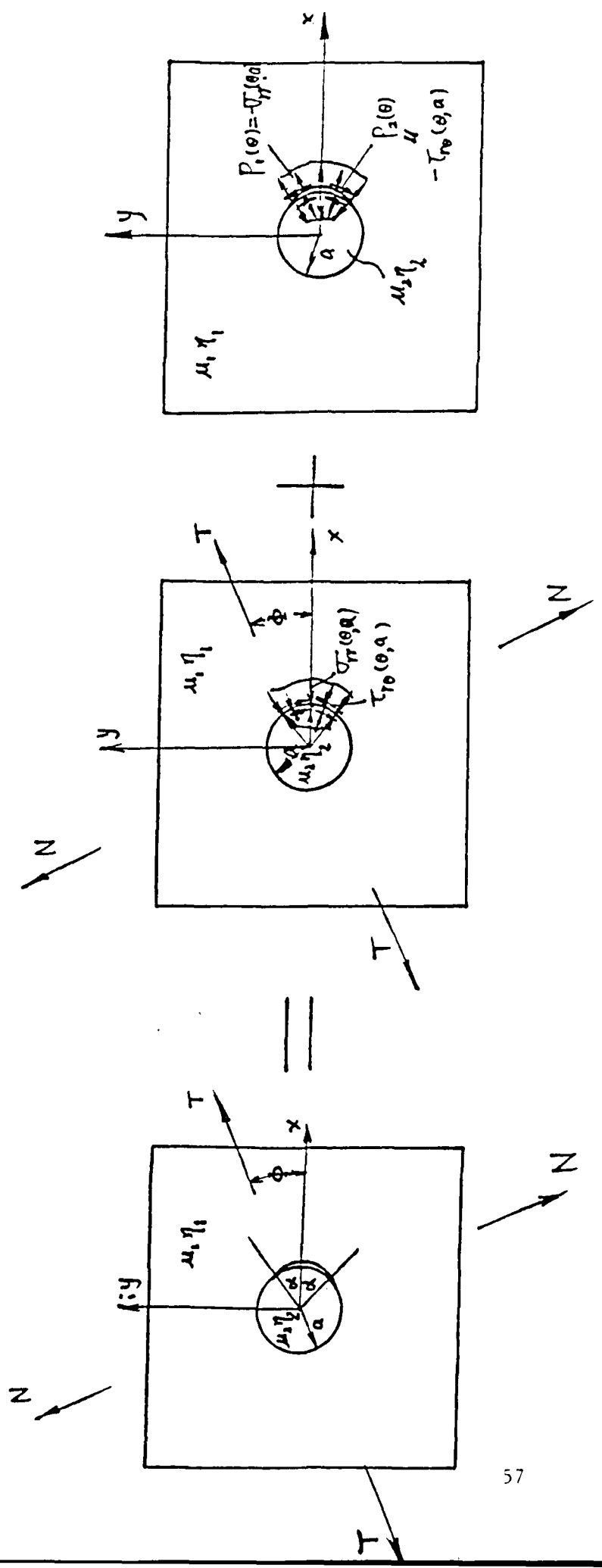


Fig. 24. Variation of the normalized strain energy release rate $g(\epsilon)$ with ϵ/R



a) Original problem

b) uncracked geometry

c) cracked geometry

Figure 25. Decomposition of Toya's solution.

EFFECT OF MATERIAL PROPERTIES INTERFACIAL CRACK(TWO FIBER MODEL)

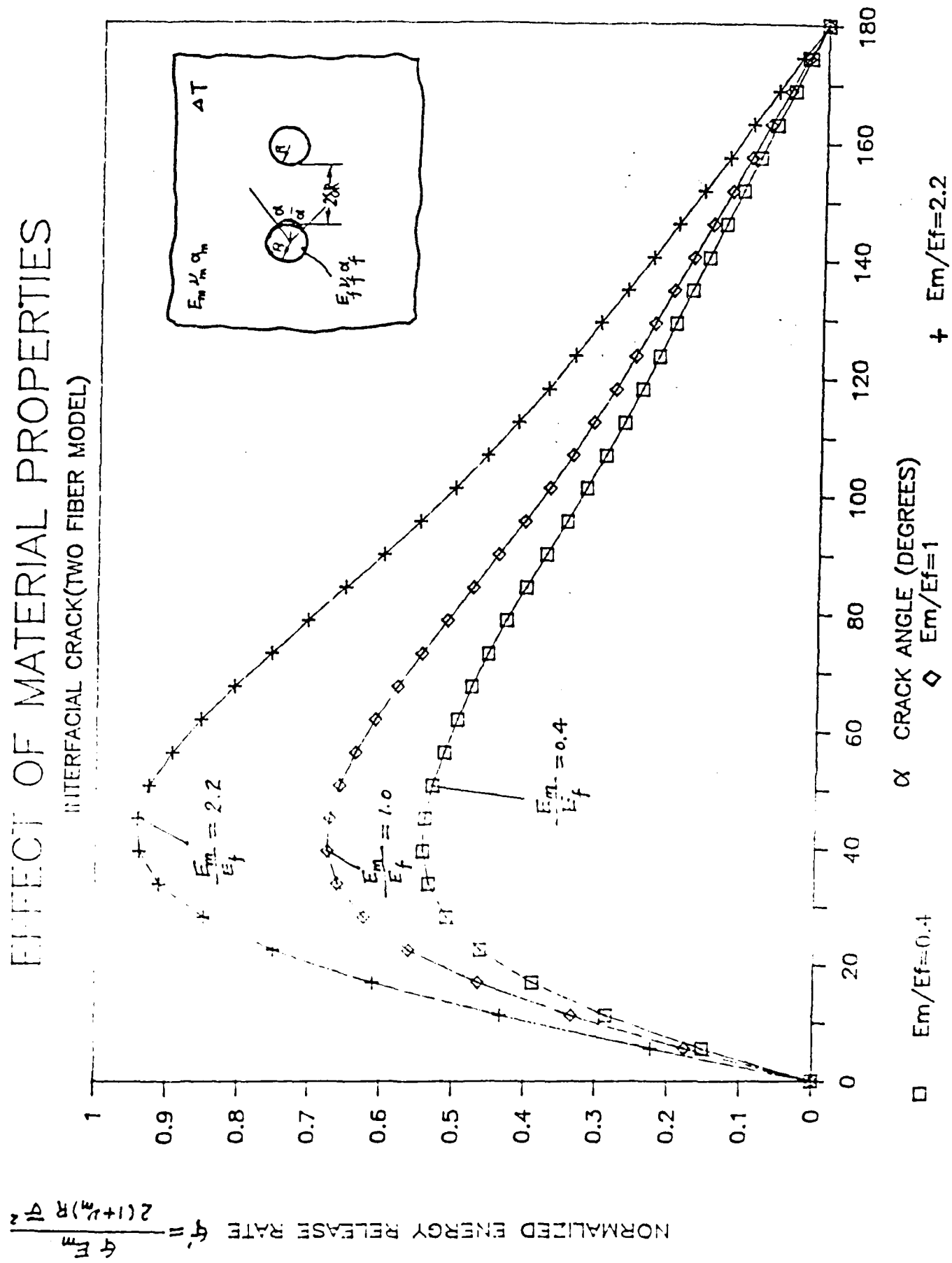


Figure 26.

EFFECT OF NEIGHBORING FIBER

INTERFACIAL CRACK (TWO FIBER MODEL)

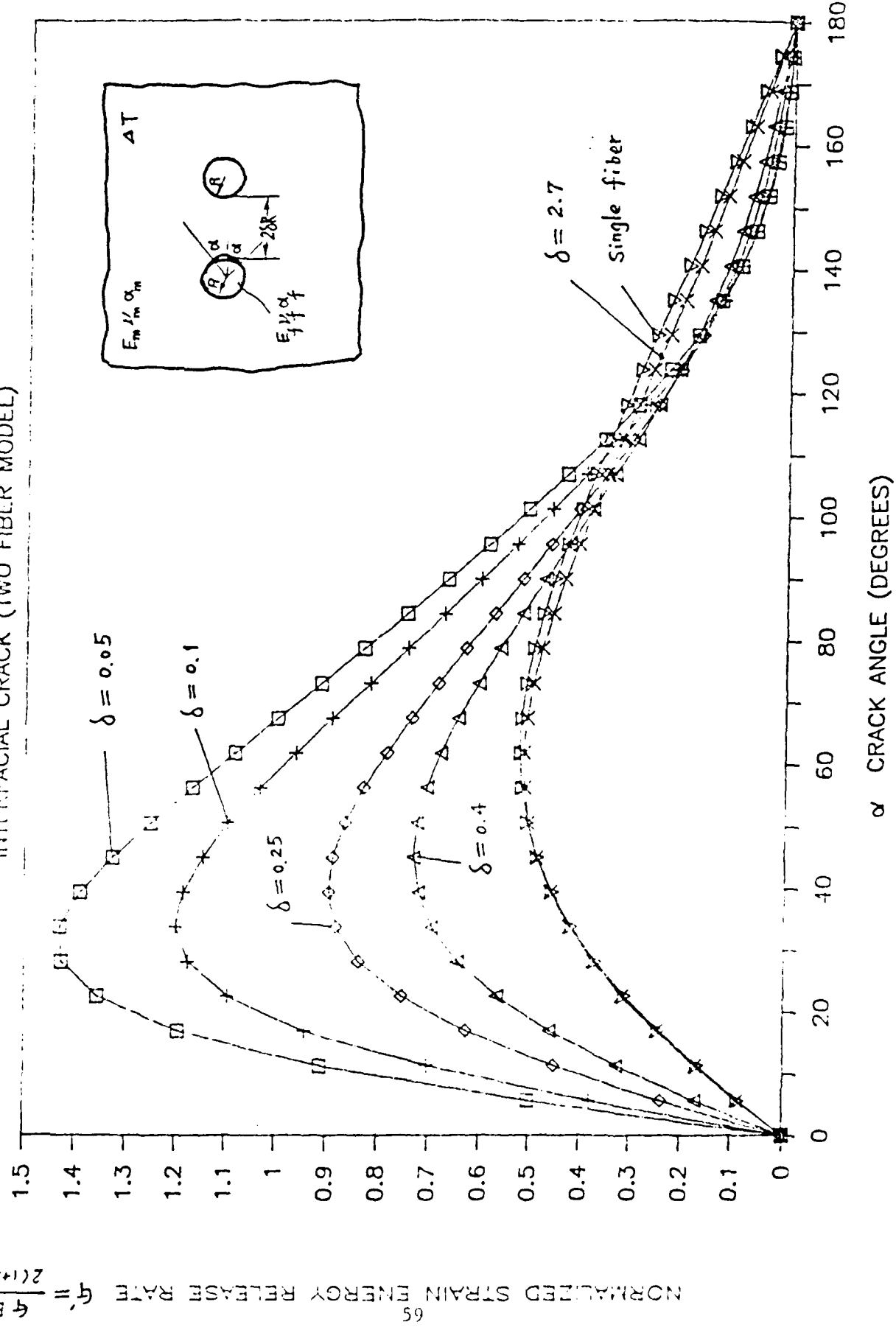


Figure 27.

COMPARISON WITH SINGLE FIBER MODEL
INTERFACIAL CRACK

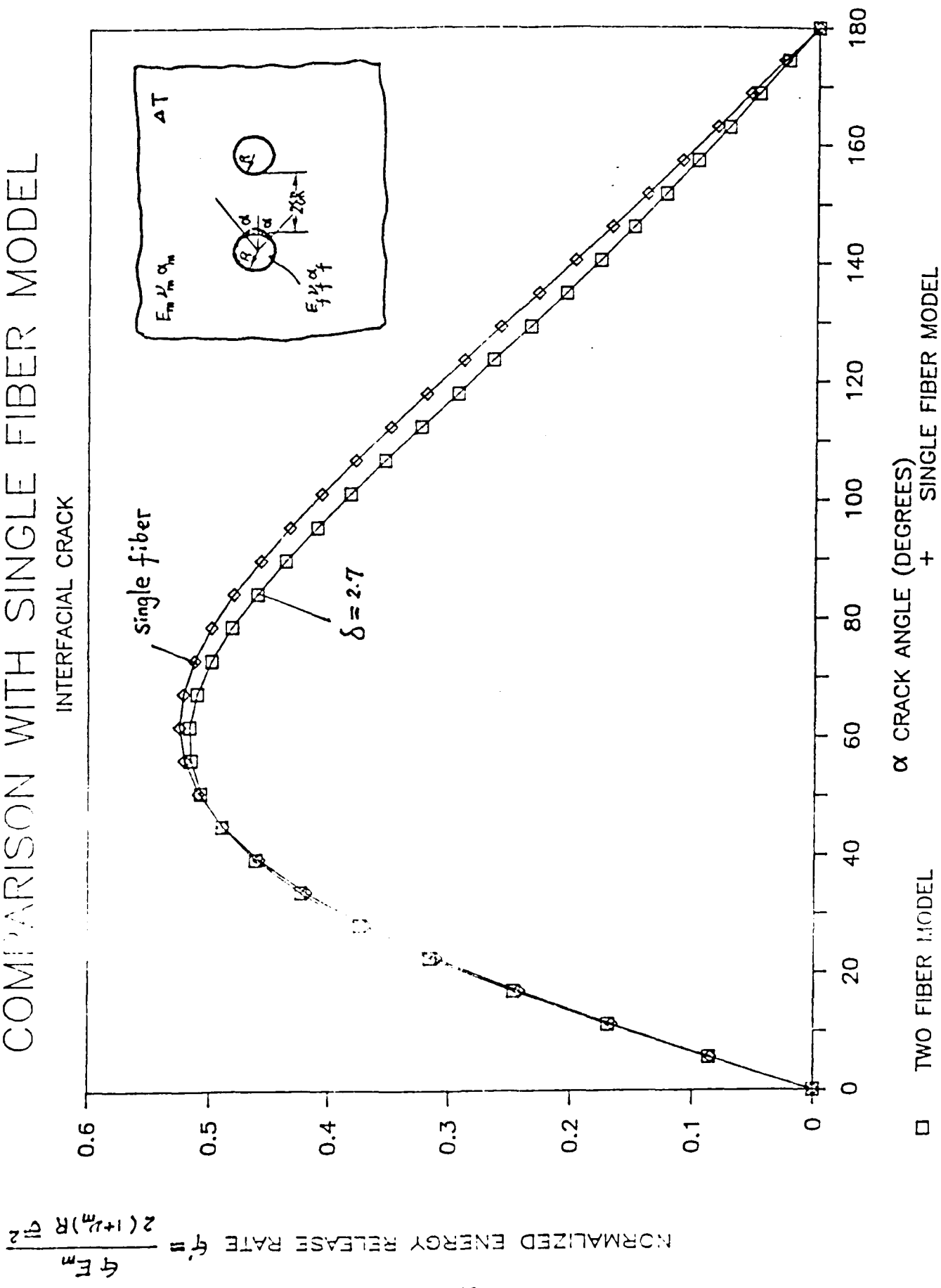
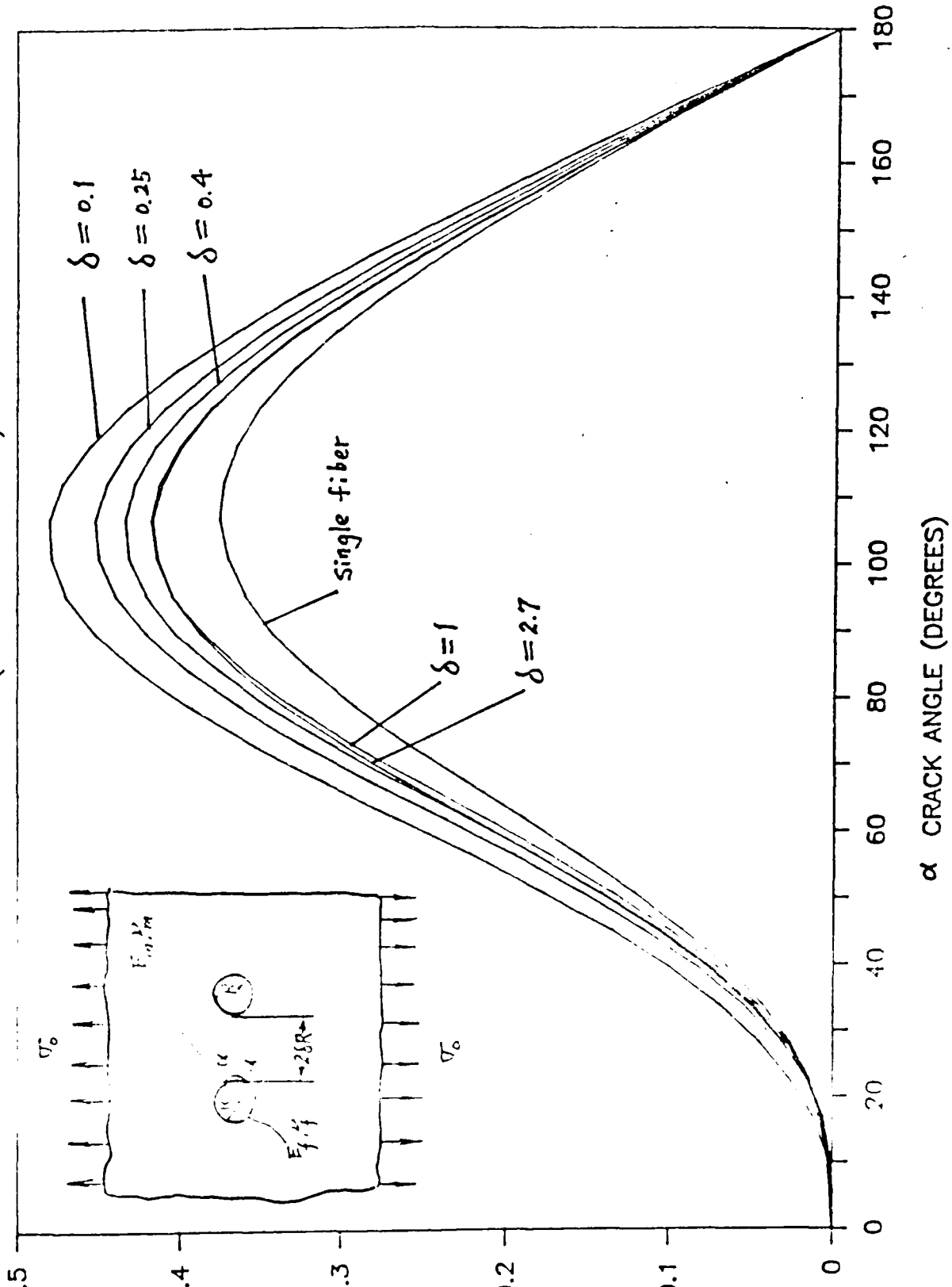


Figure 28.

EFFECT OF NEIGHBORING FIBER
INTERFACIAL CRACK (TWO FIBER MODEL)



$$\text{NORMALIZED ENERGY RELEASE RATE } \bar{G} = \frac{G}{E_m} = \frac{2(1+\nu_m)R\dot{\gamma}_0}{E_m}$$

Figure 29.

COMPARISON WITH SINGLE FIBER CASE
INTERFACIAL CRACK

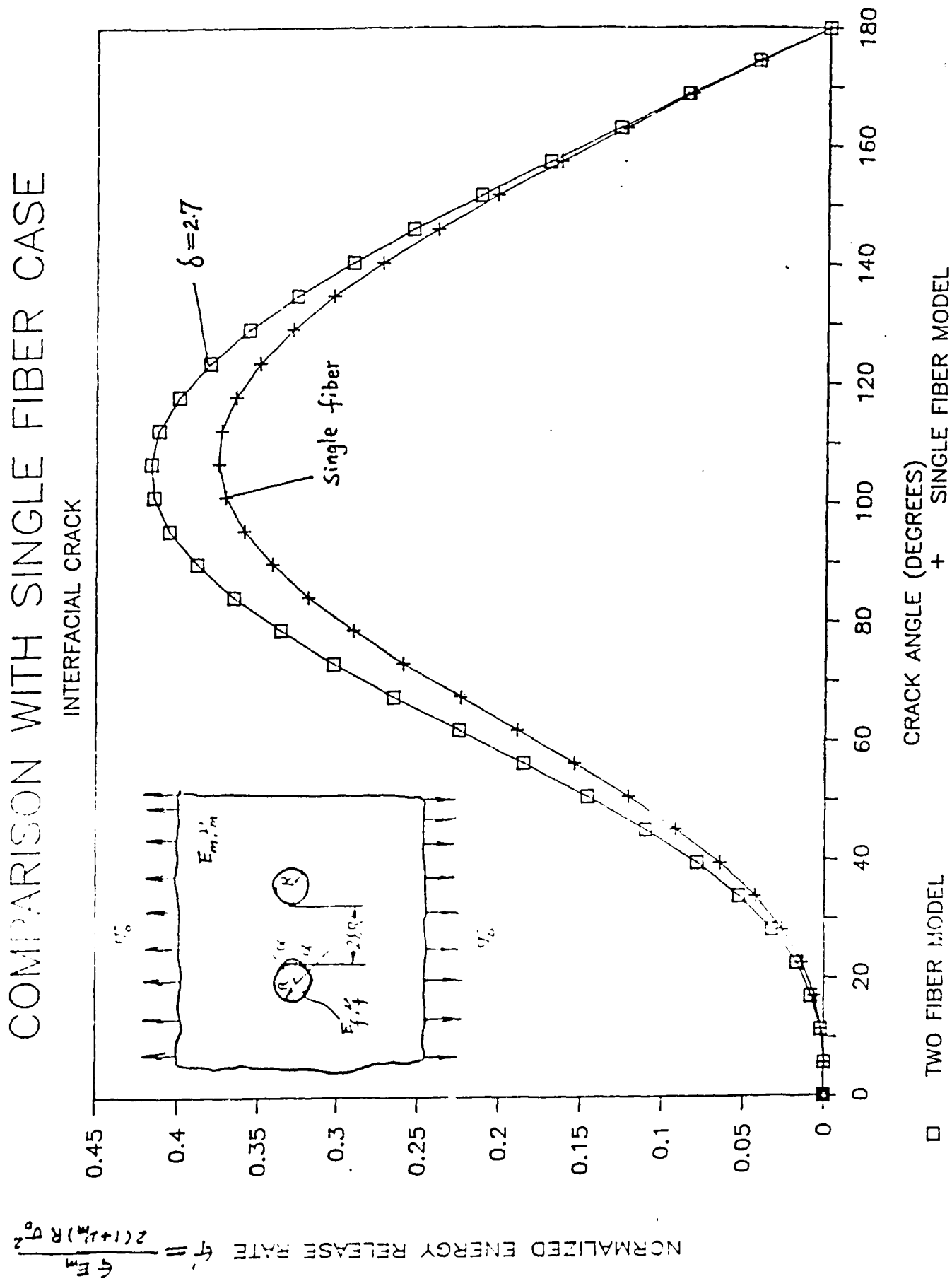


Figure 30.

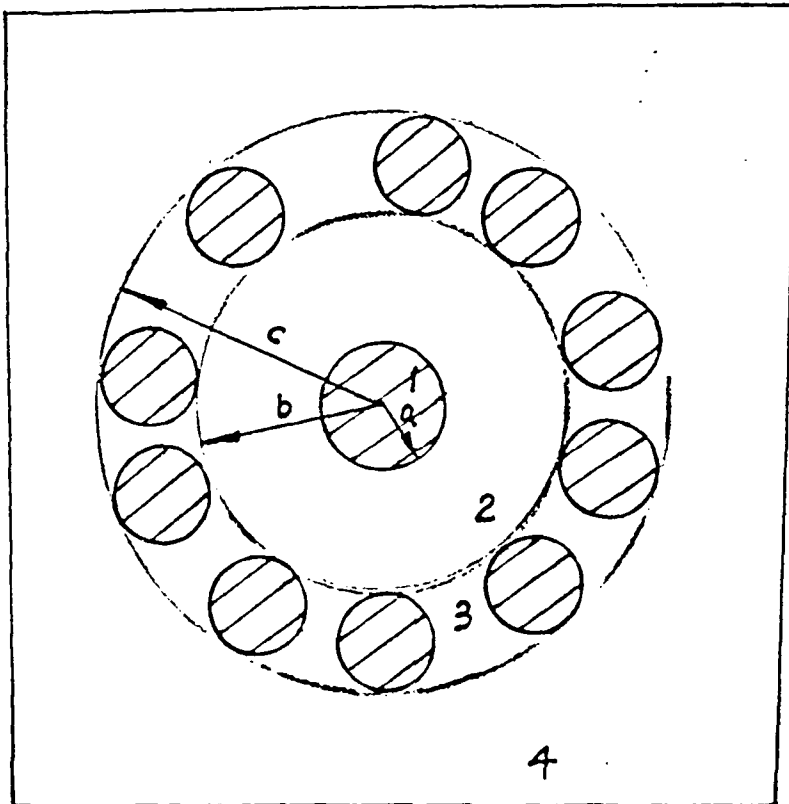
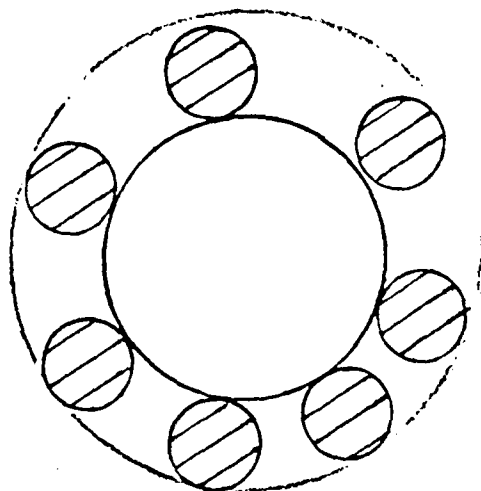
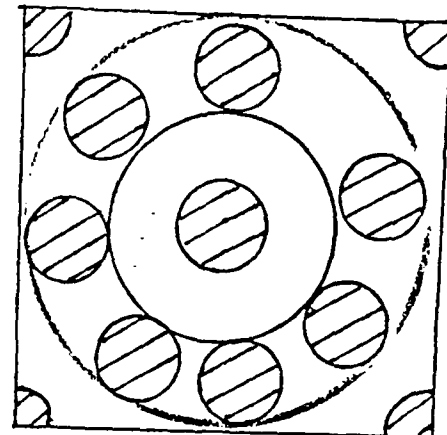


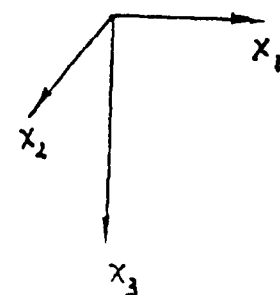
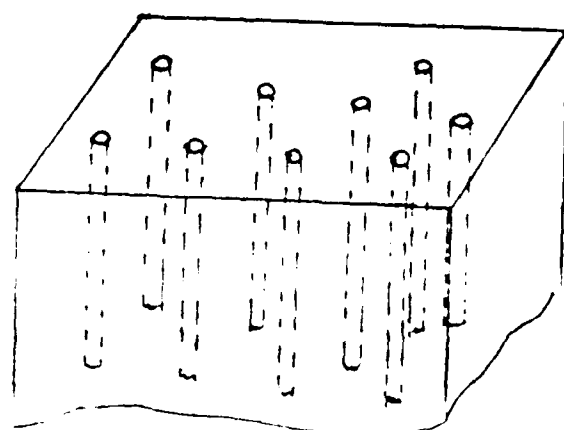
Fig 32. Ring model



a) Calculation of volume fraction
of fibers in region 3



b) Calculation of overall volume
fraction in region 4



c) Coordinate system for calculation
of elastic parameters

Fig 33. Calculation of elastic parameters
in ring model

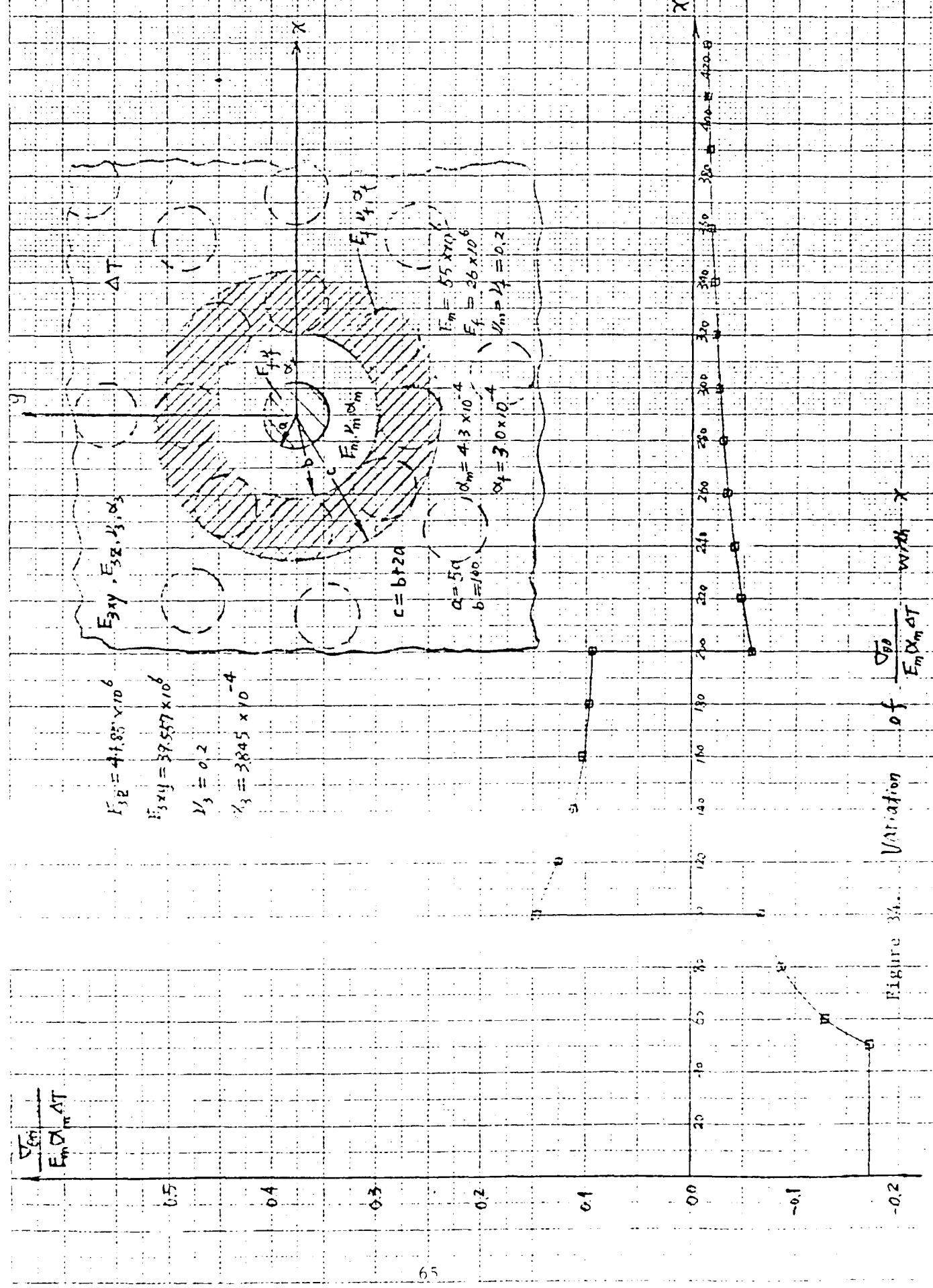


Figure 34. Variation of $\frac{V_B}{E_m \Delta m \sigma T}$ with X

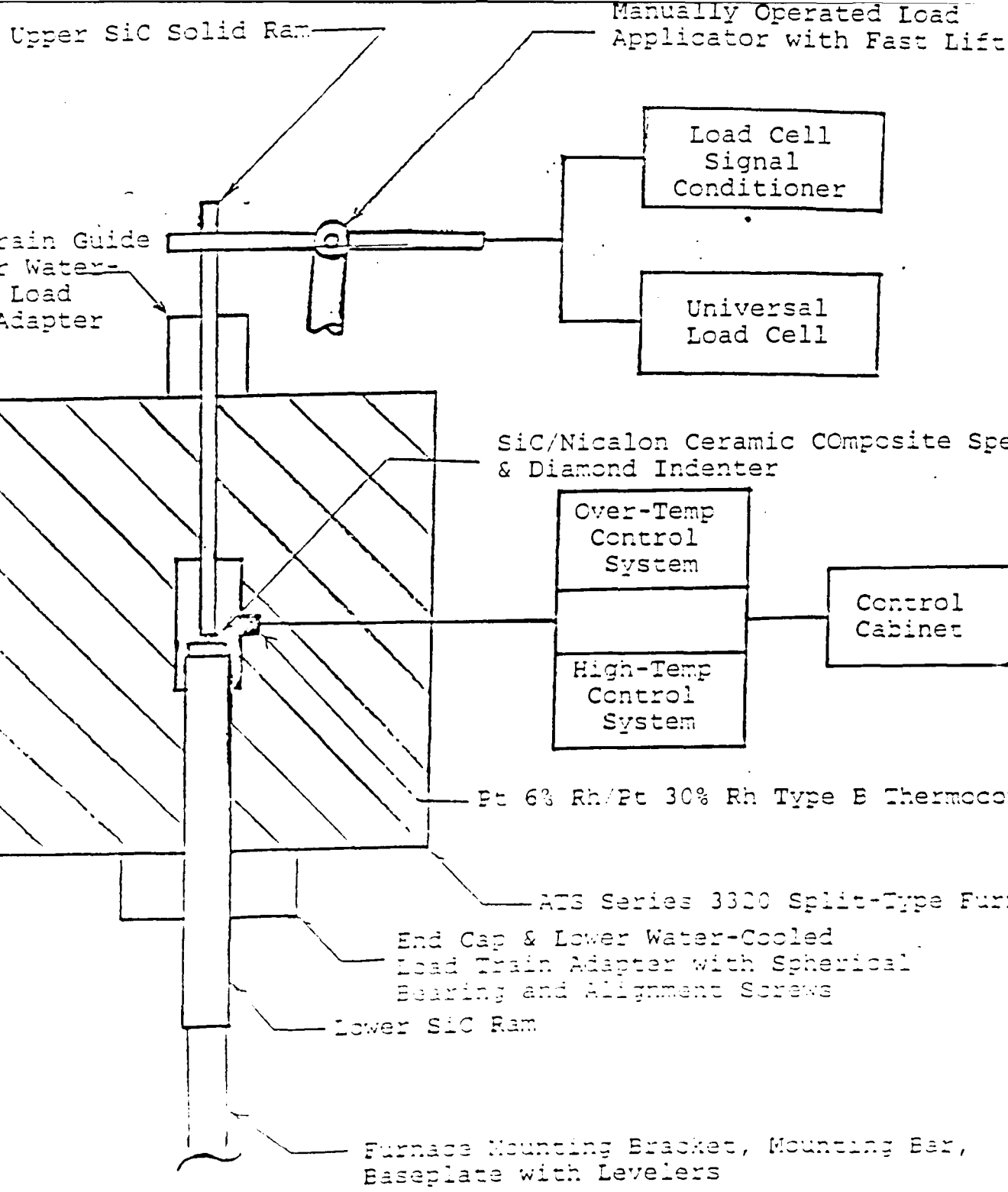


FIGURE 35. EXPERIMENTAL SET-UP OF HIGH-TEMPERATURE MICROINDENTATION TESTING OF CERAMIC COMPOSITES.

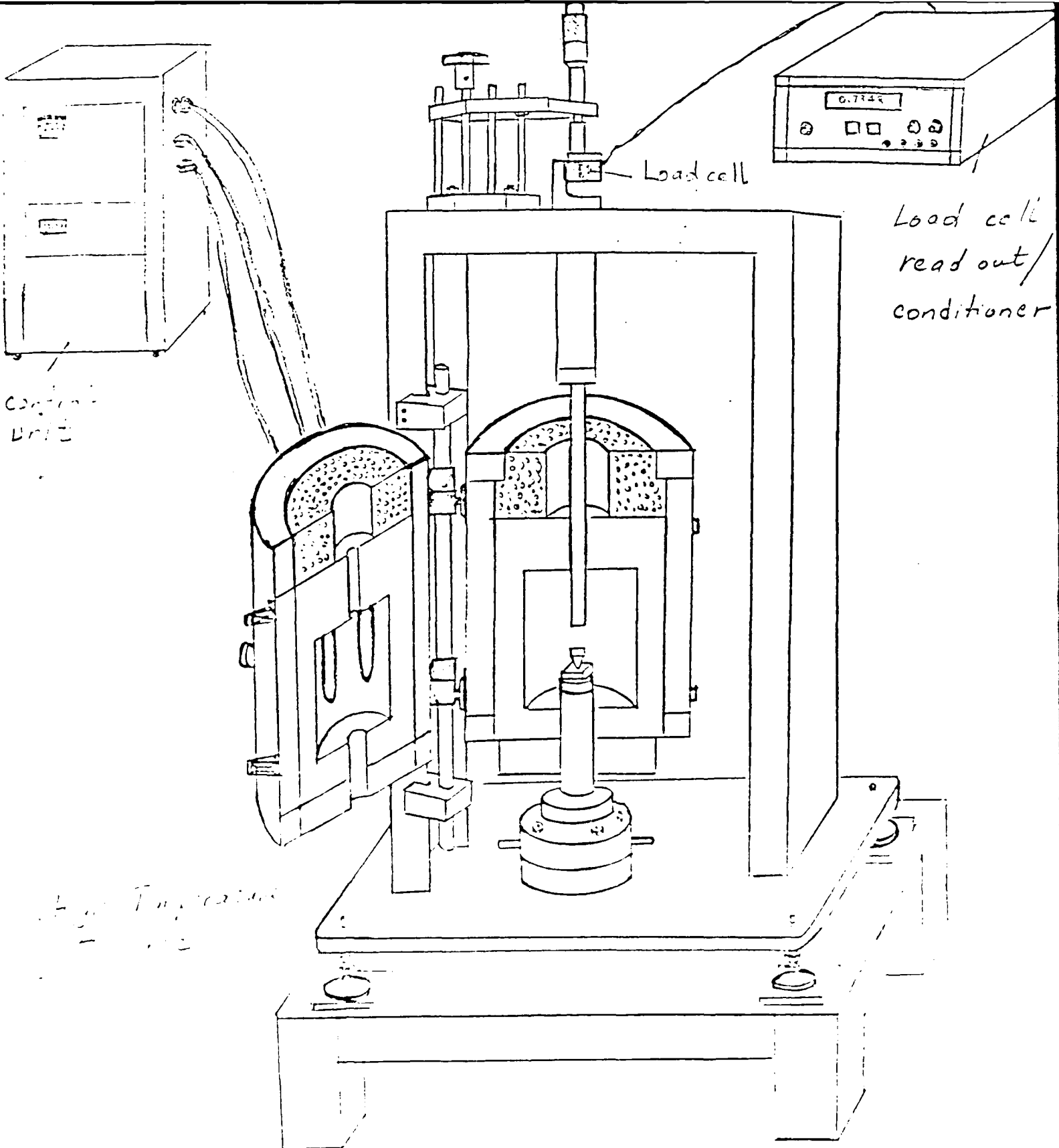
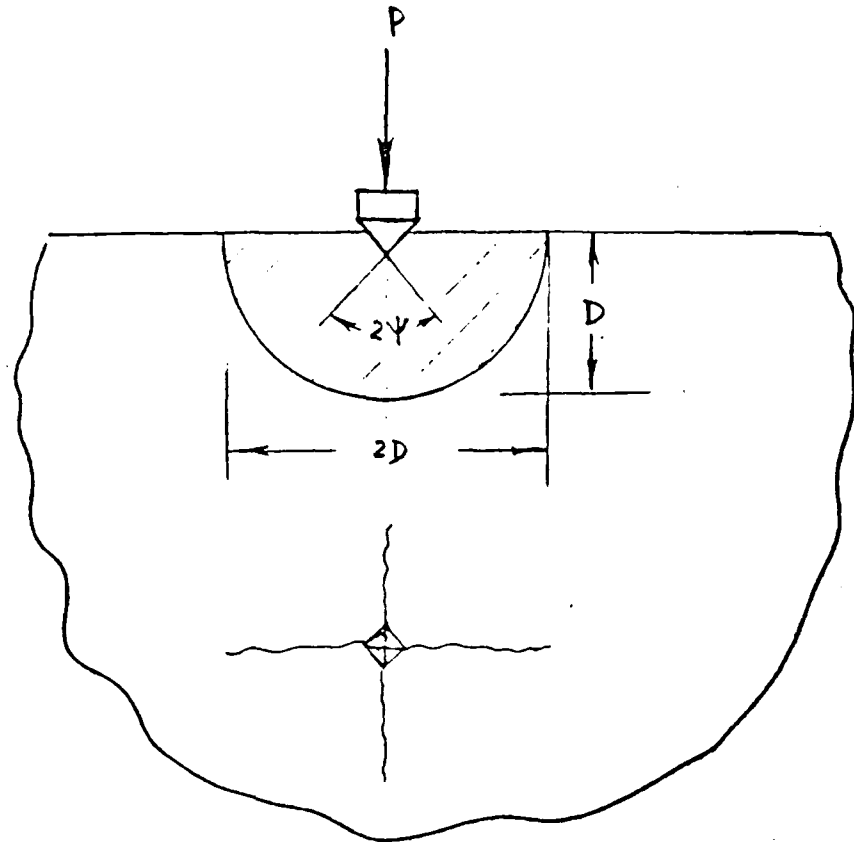


Fig. 36. Configuration of series 3320 split-tube laboratory furnace



Formula for measuring K_{1c} from
Indentation fracture technique

$$K_{1c} = \frac{P}{\pi^{3/2} \tan \psi} \left(\frac{P}{D^{3/2}} \right) \quad \gamma = c \cdot \varepsilon$$

Fig 37. Indentation test to determine K_{1c}
of ceramic matrix materials

EFFECT of TEMPERATURE on K_{IC} of MATRIX

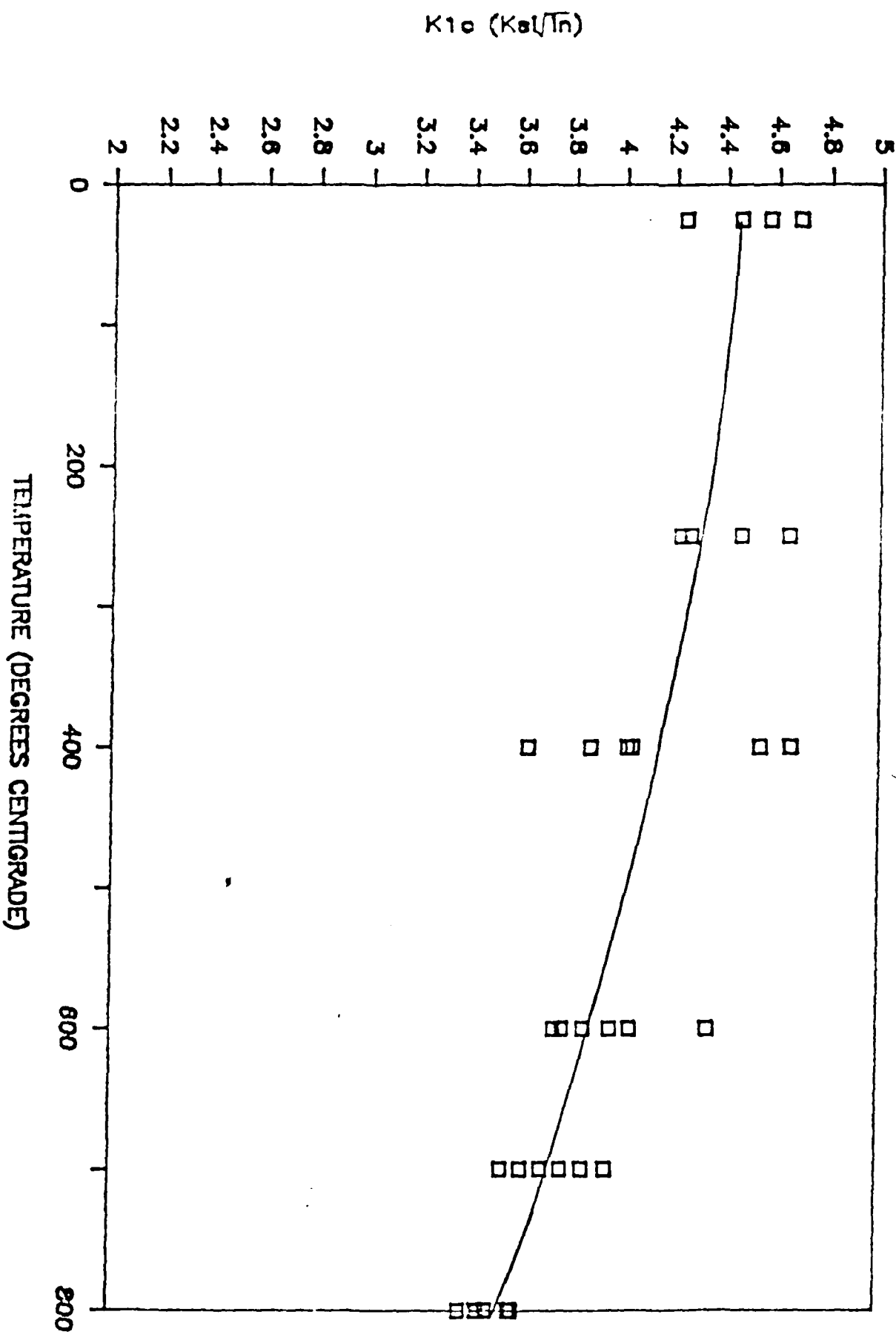


Fig. 38. Effect of temperature on K_{IC} of matrix

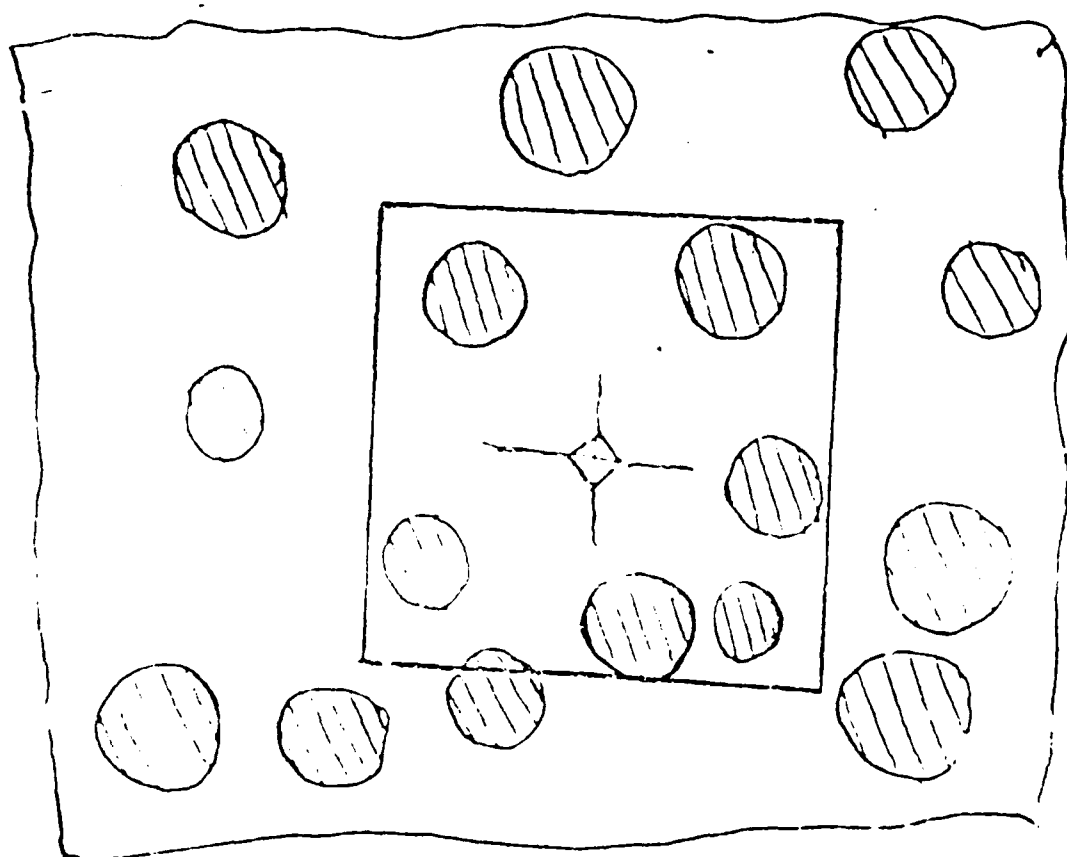
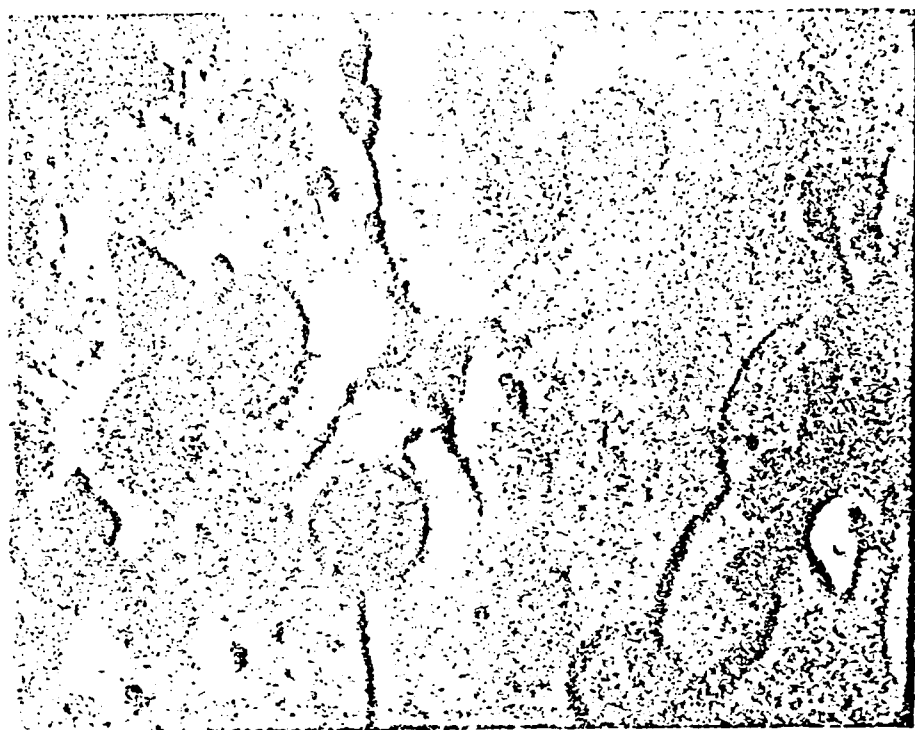


FIG. 39. Indentation on Matrix in the Ceramic Composite

K₁C_{apparent} .VS. V_f
120°C TEMPERATURE 25C

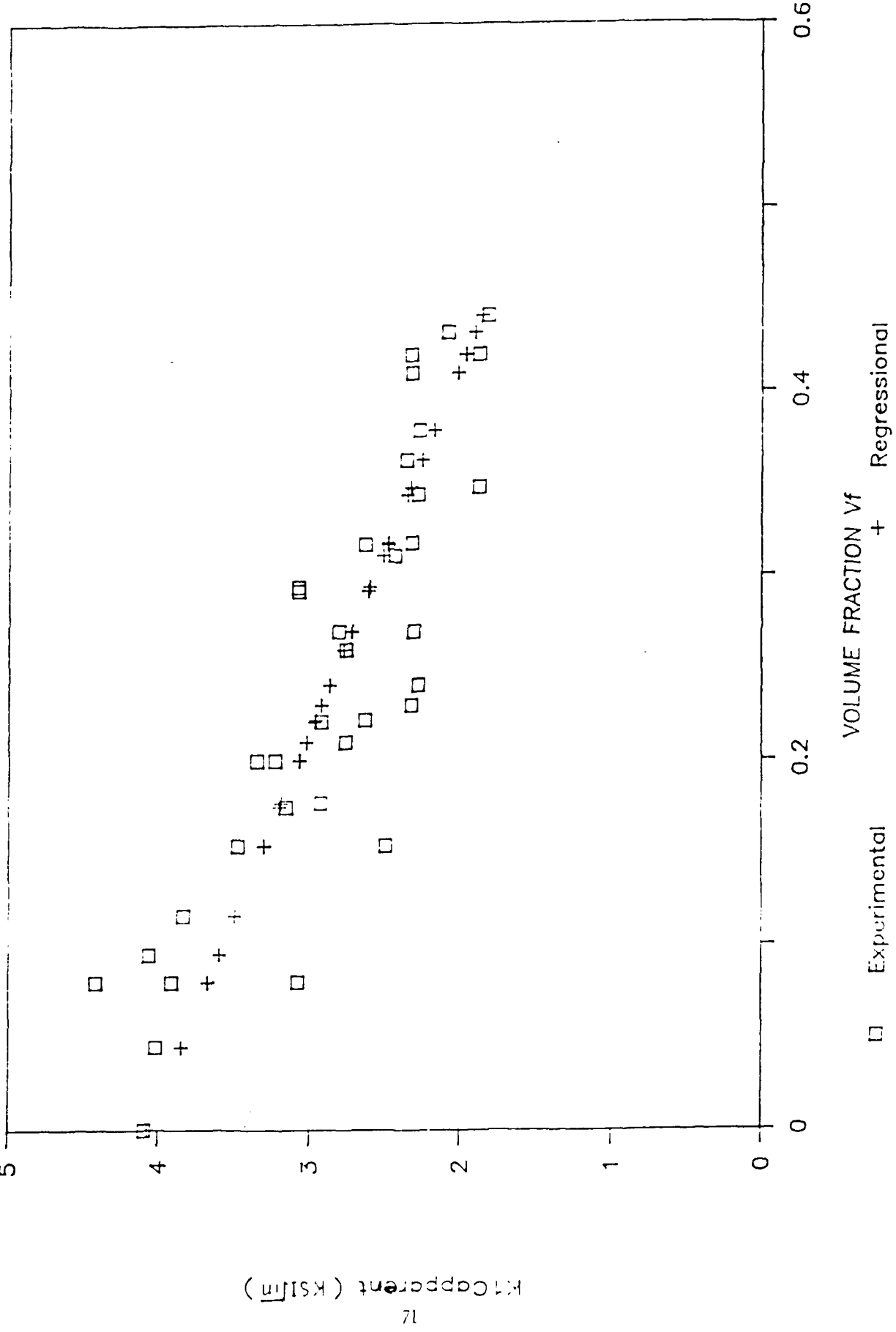
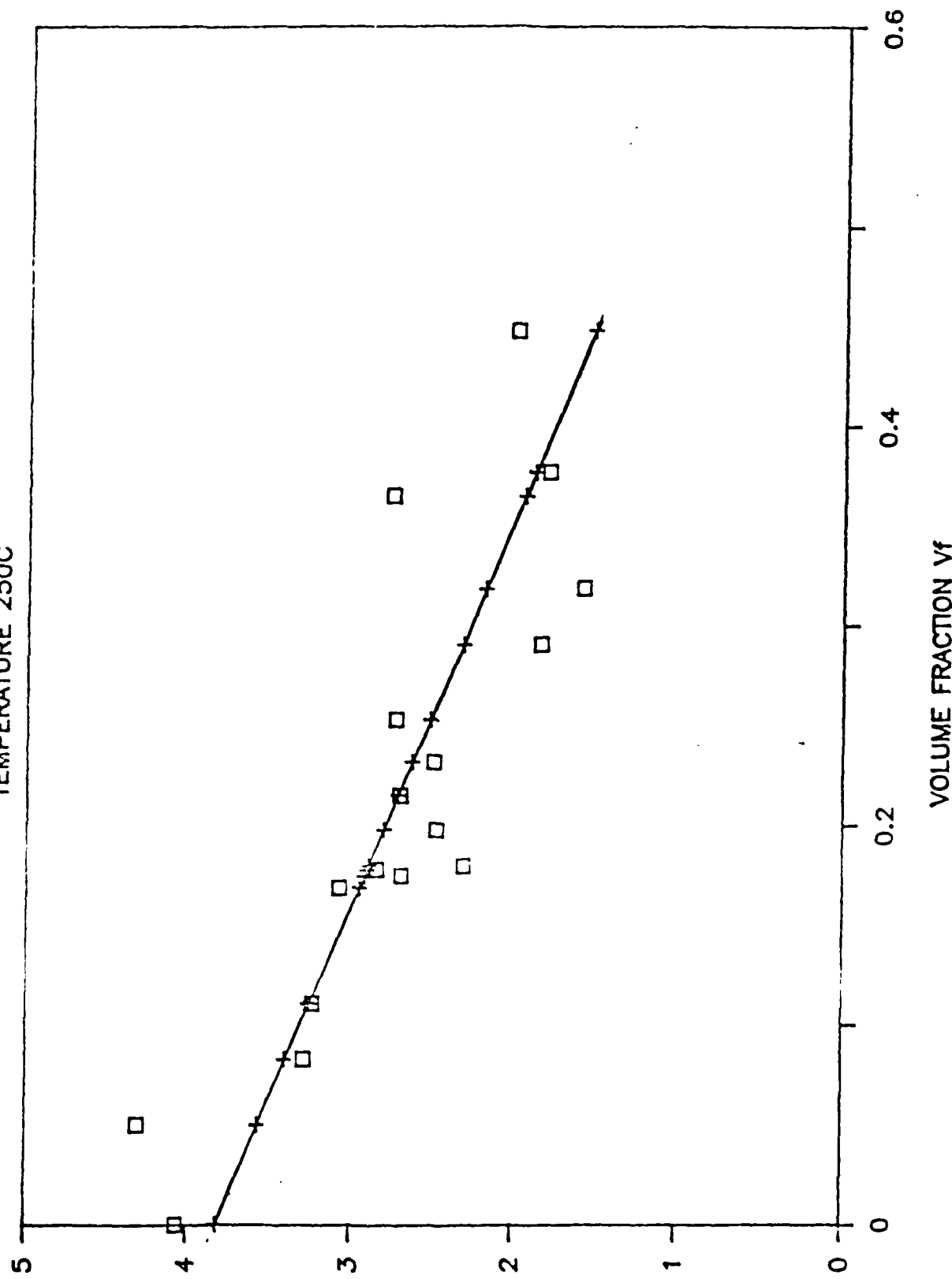


Fig. 40.

K_{1C} .vs. V_f
TEMPERATURE 250C



K_{1C} APPARENT (kN/mm)

Fig. 41.

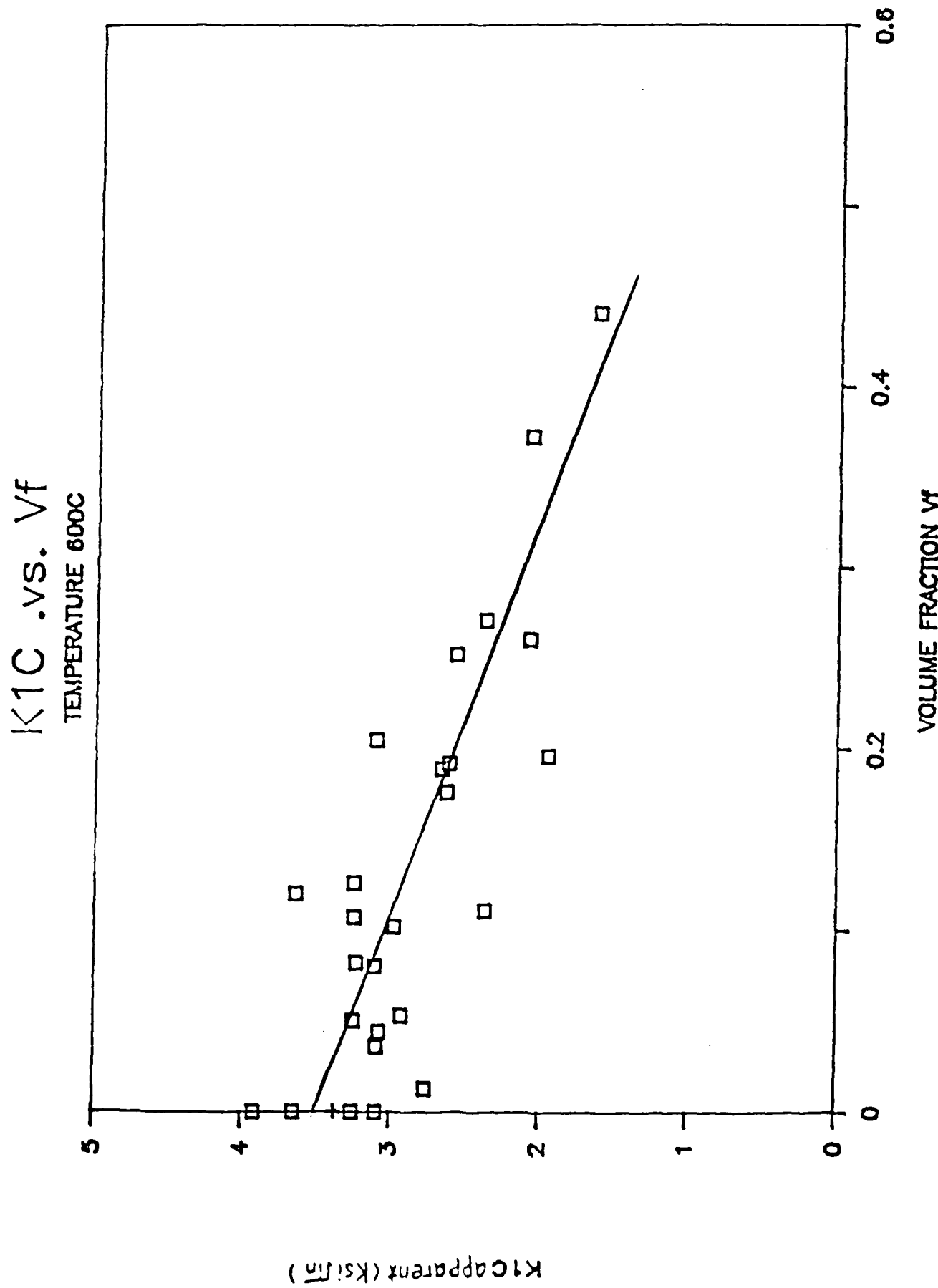


Fig. 42.

$K_1 C_{apparent}$.VS. V_f
TEMPERATURE 800C

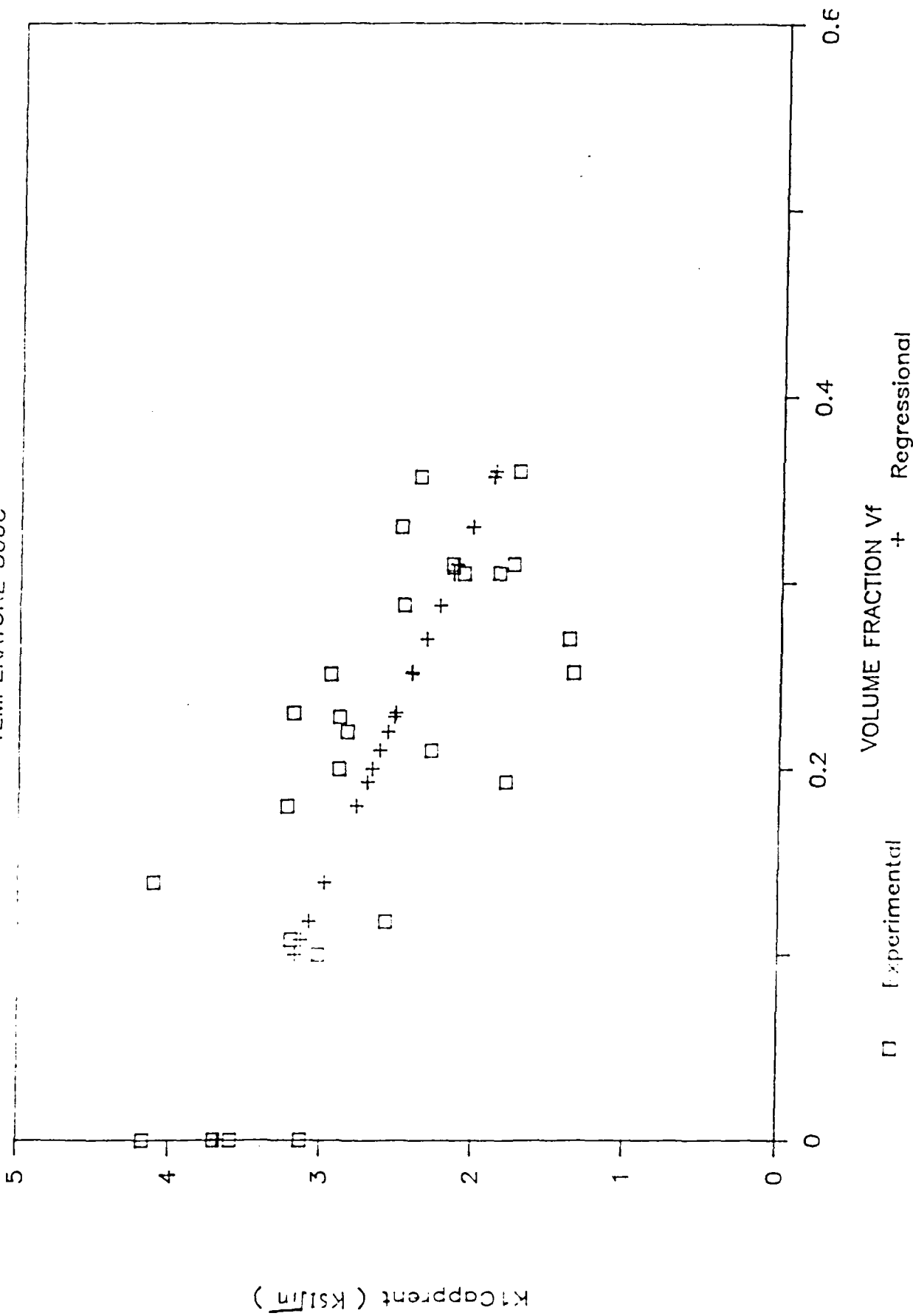
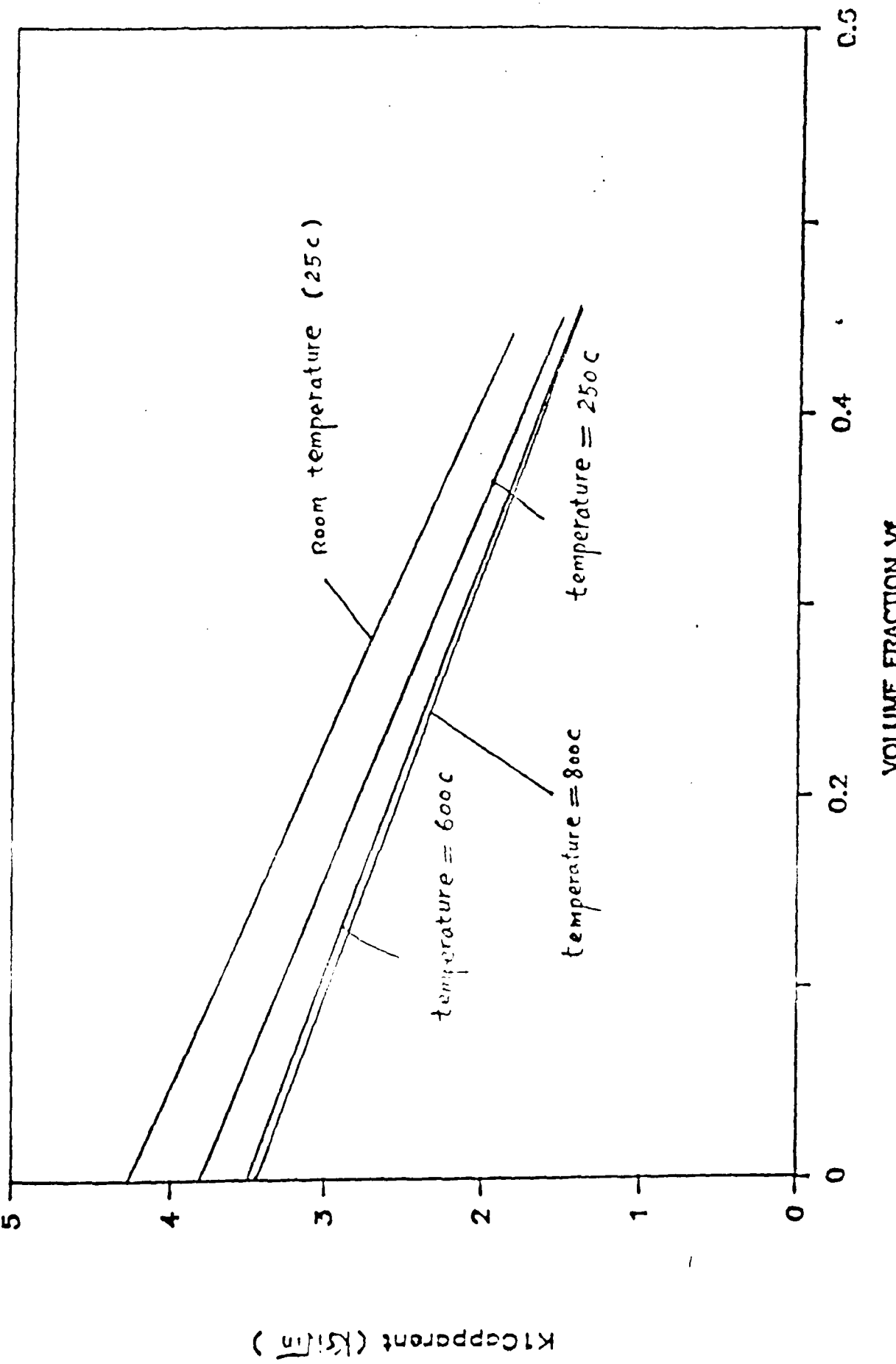


Fig. 43.

$K_1 C_{app.}$ vs. V_f
WITH TEMPERATURE EFFECT



$K_1 C_{apparent} (kg/l)$

Fig. 44.

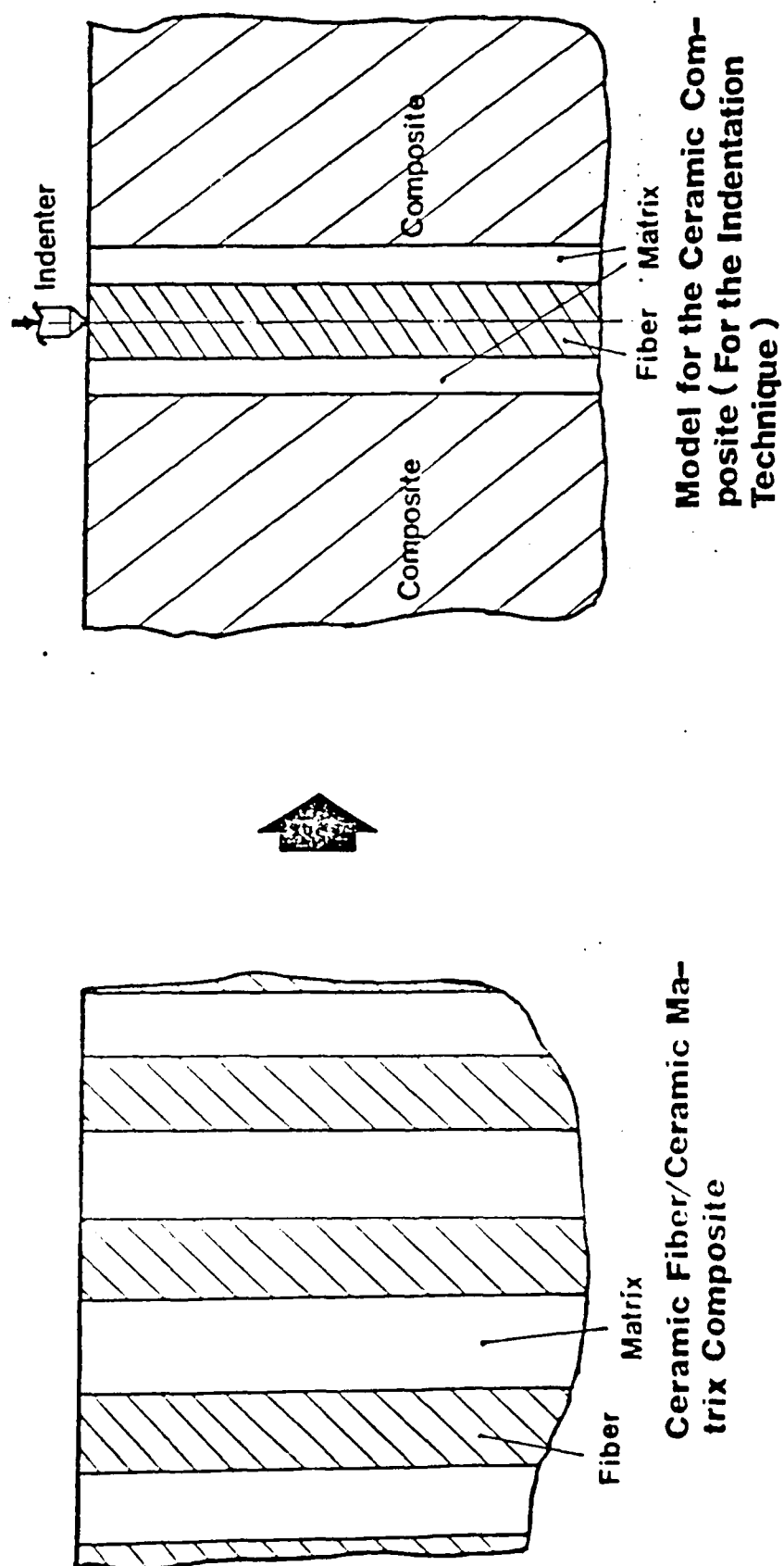


Figure 45.

Debonding load .vs. Fiber Area

77

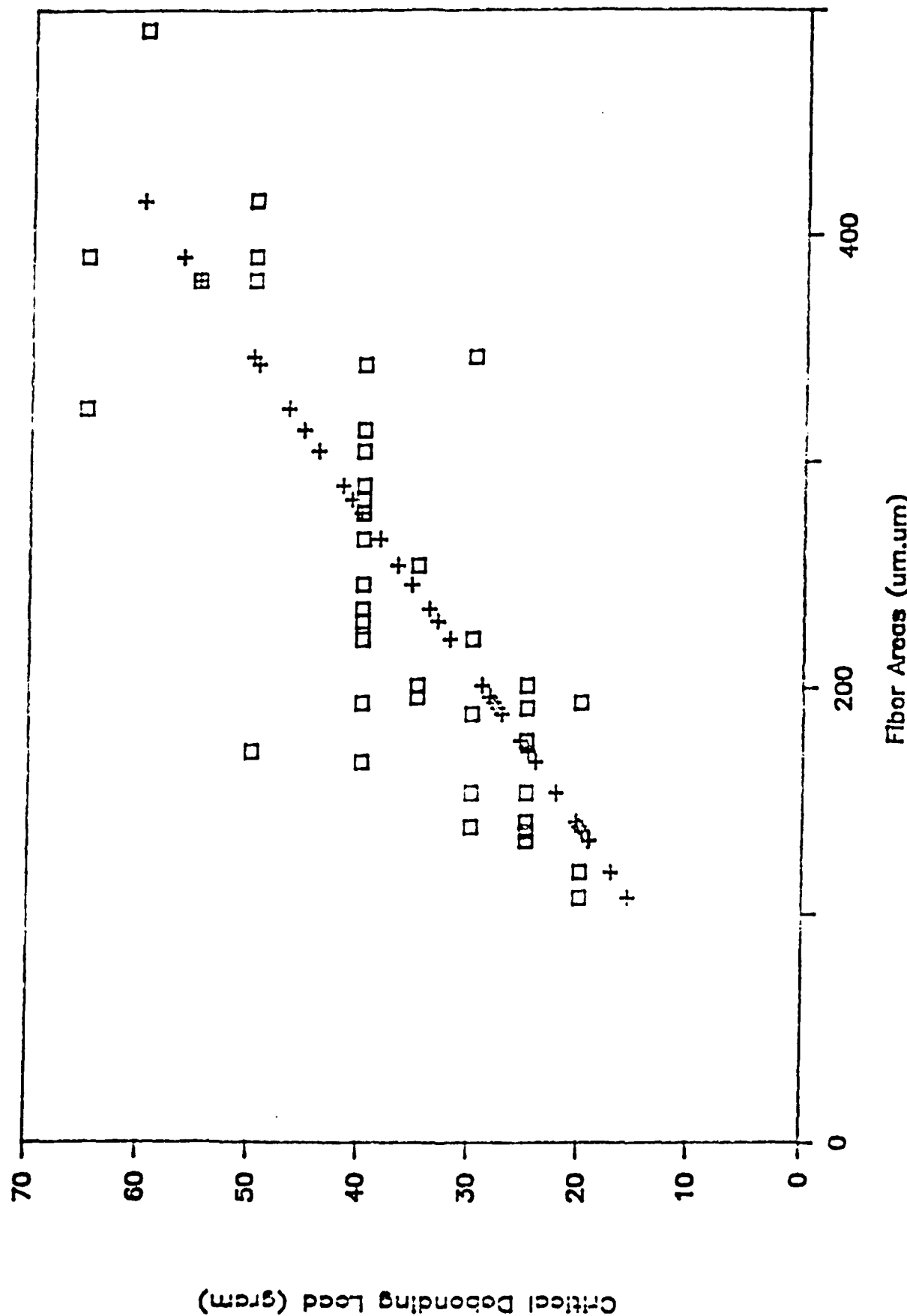


Fig. 46.

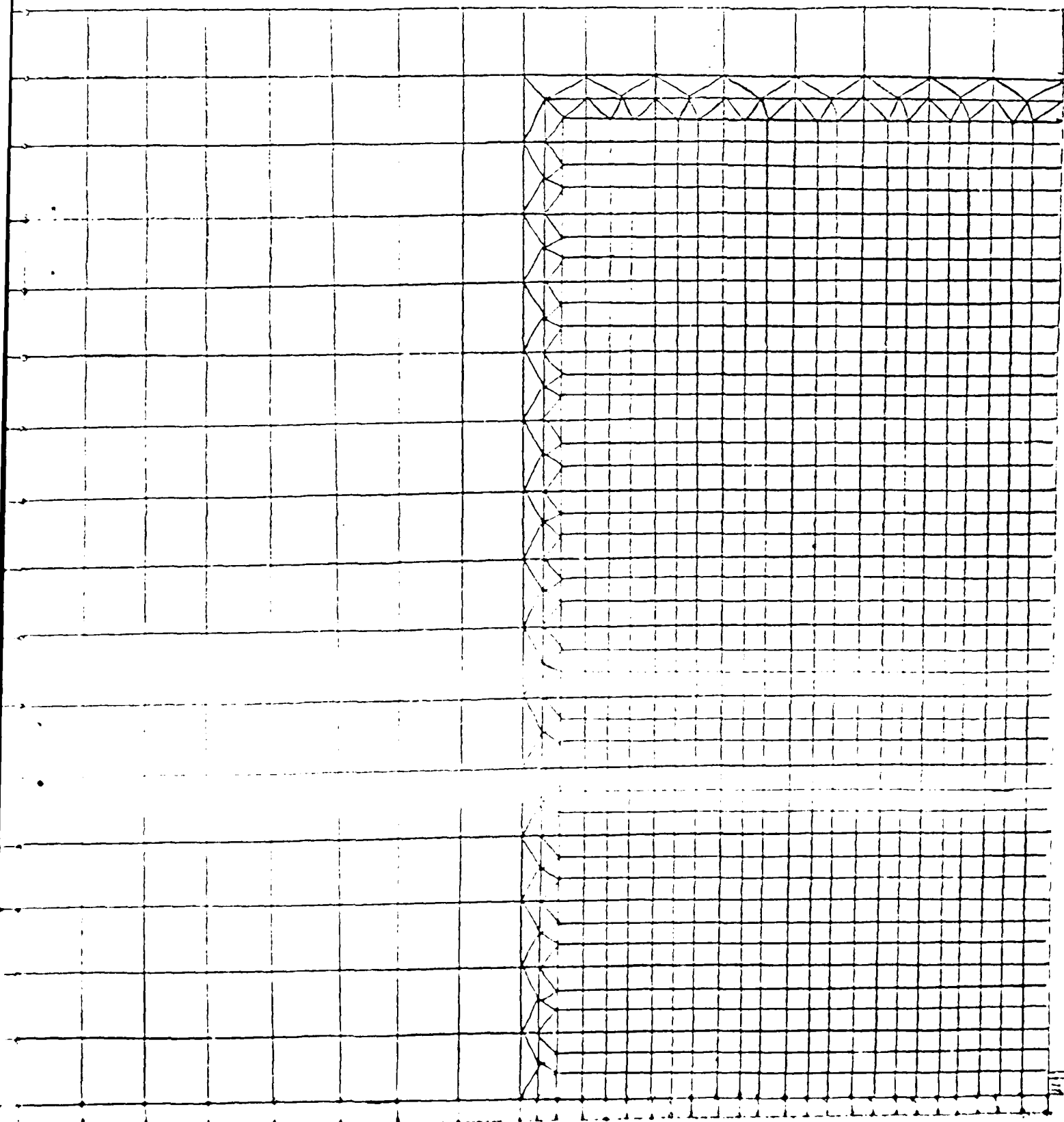


Fig. 46a Finite element model for calculation of bending strength at debonding initiation

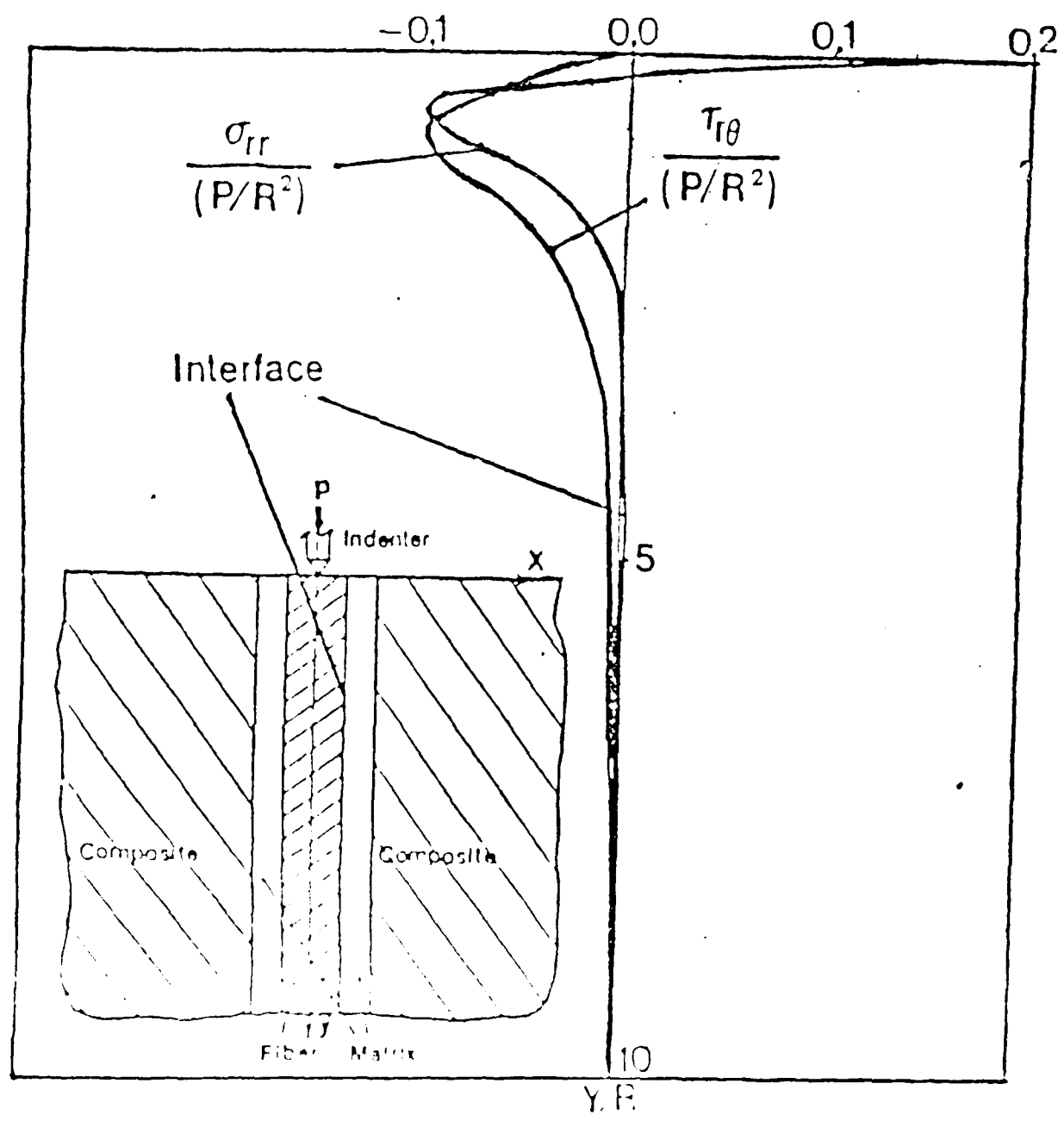


Fig. 47 .Stress distributions on the interface along the fiber axial direction under debonding loading

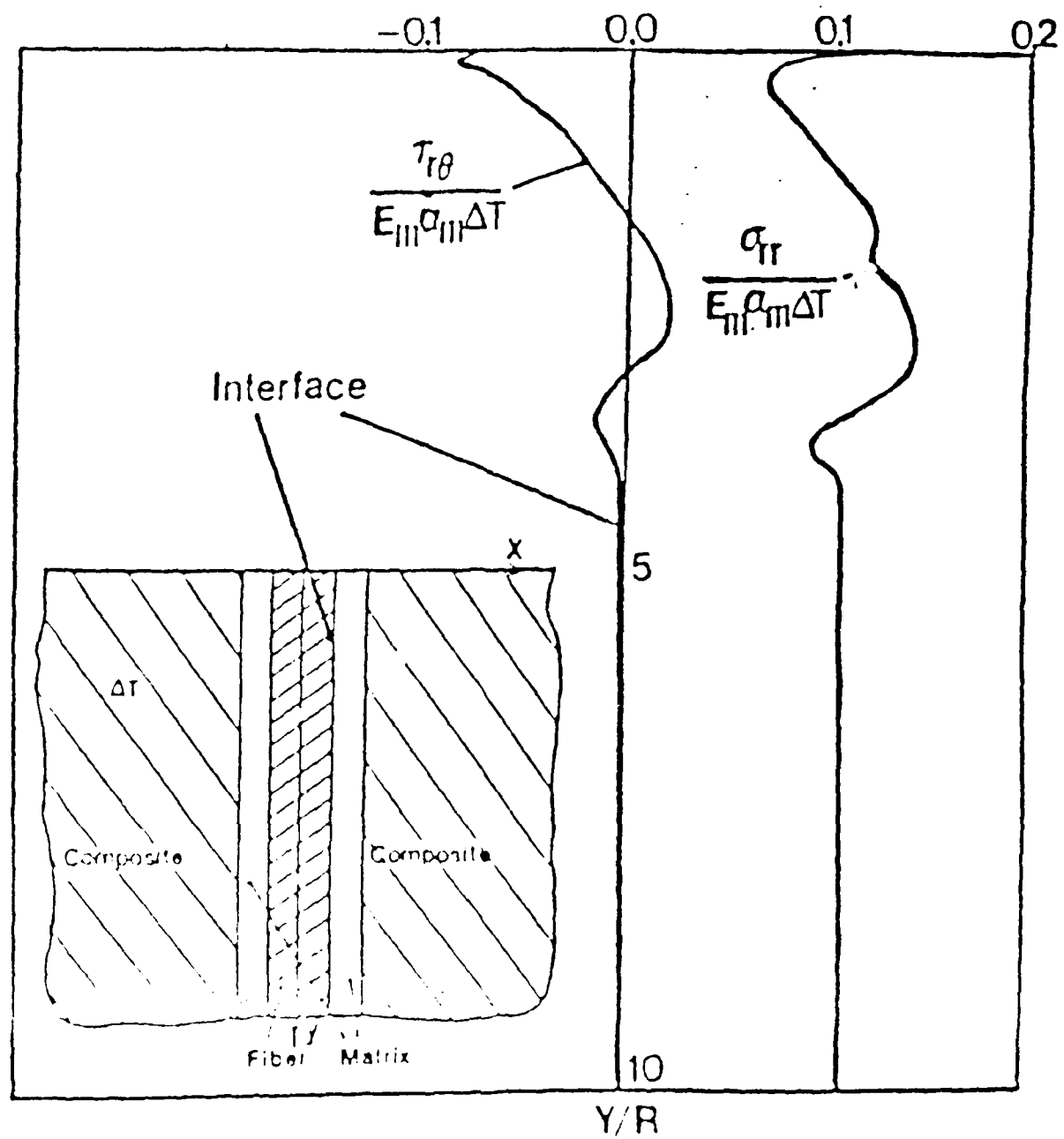
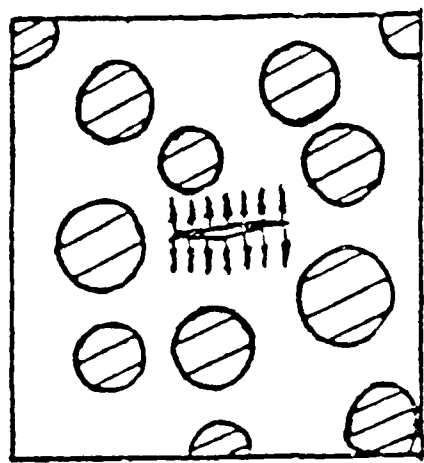
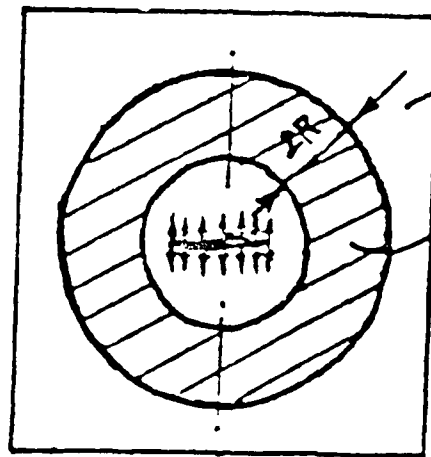


Fig 48. Stress distributions on the interface along the fiber axial direction under high temperature



(a) Actual distribution of fibers



(b) Model

Figure 19. The Theoretical Model

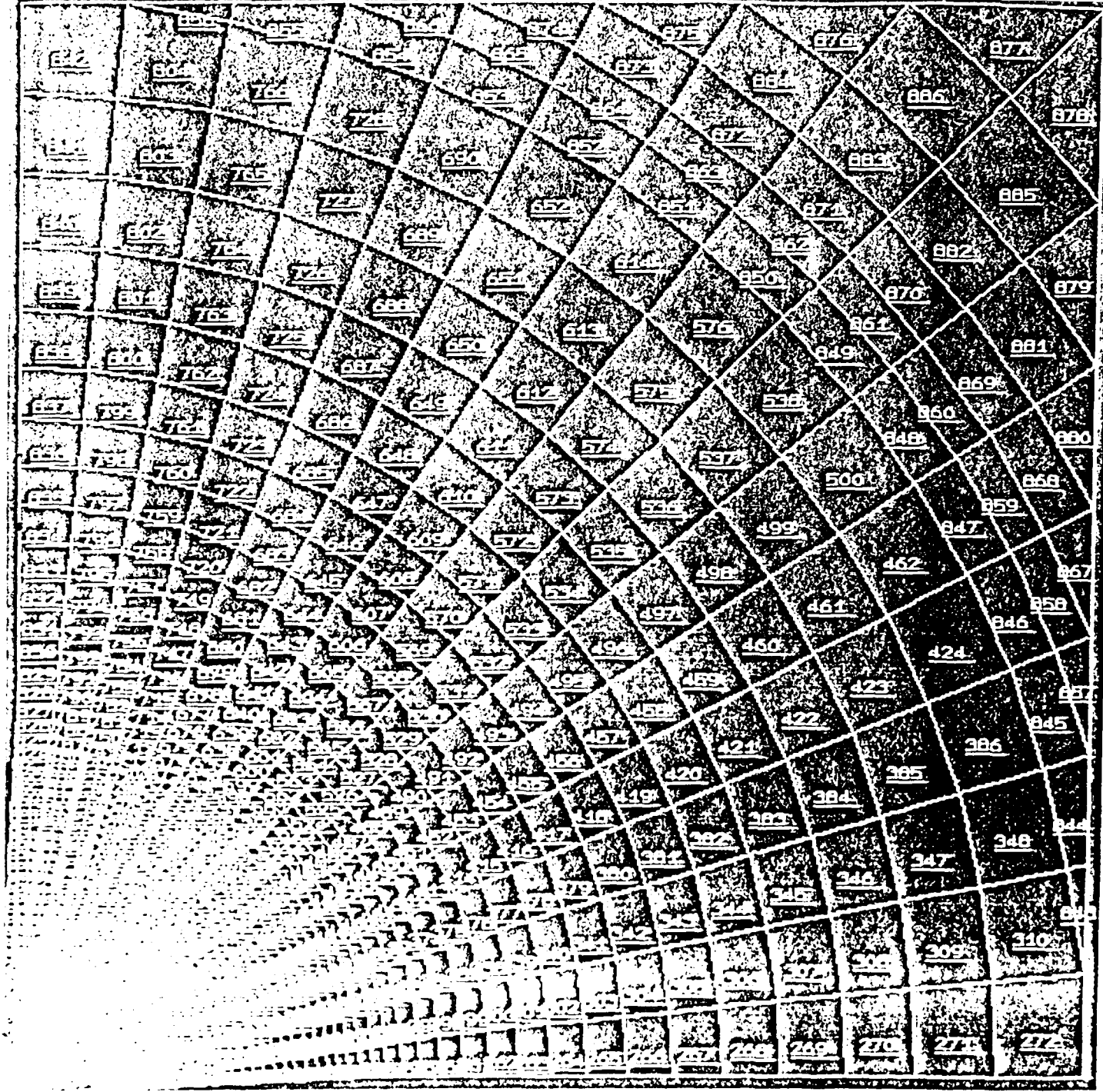


Fig. 50. Finite Element Model for Theoretical Prediction

K₁C_{apparent} .vs. V_f
ROOM TEMPERATURE 25C

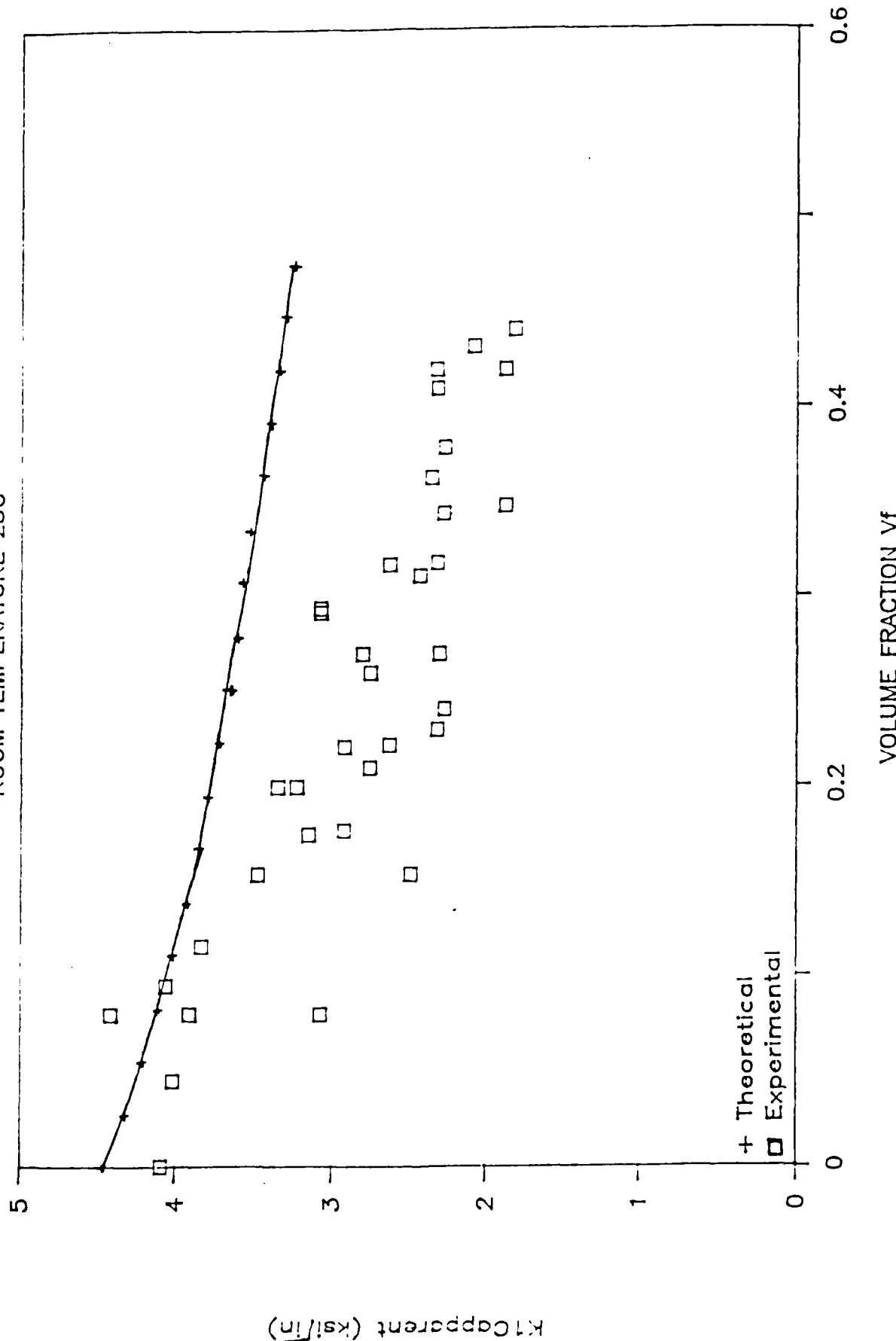


Fig. 51

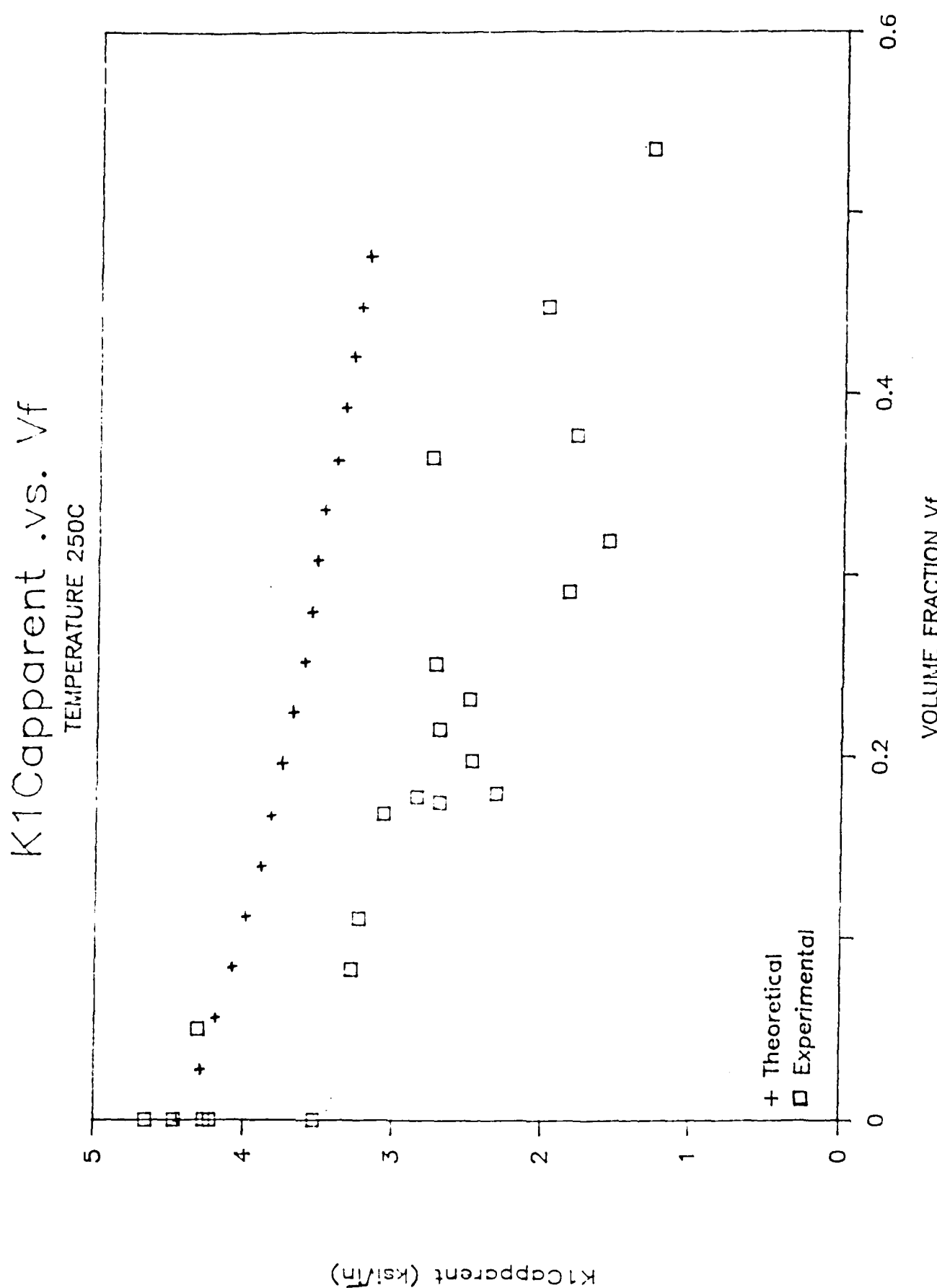


Fig. 52

K₁C_{apparent} .v.s. V_f
Temperature 600 C

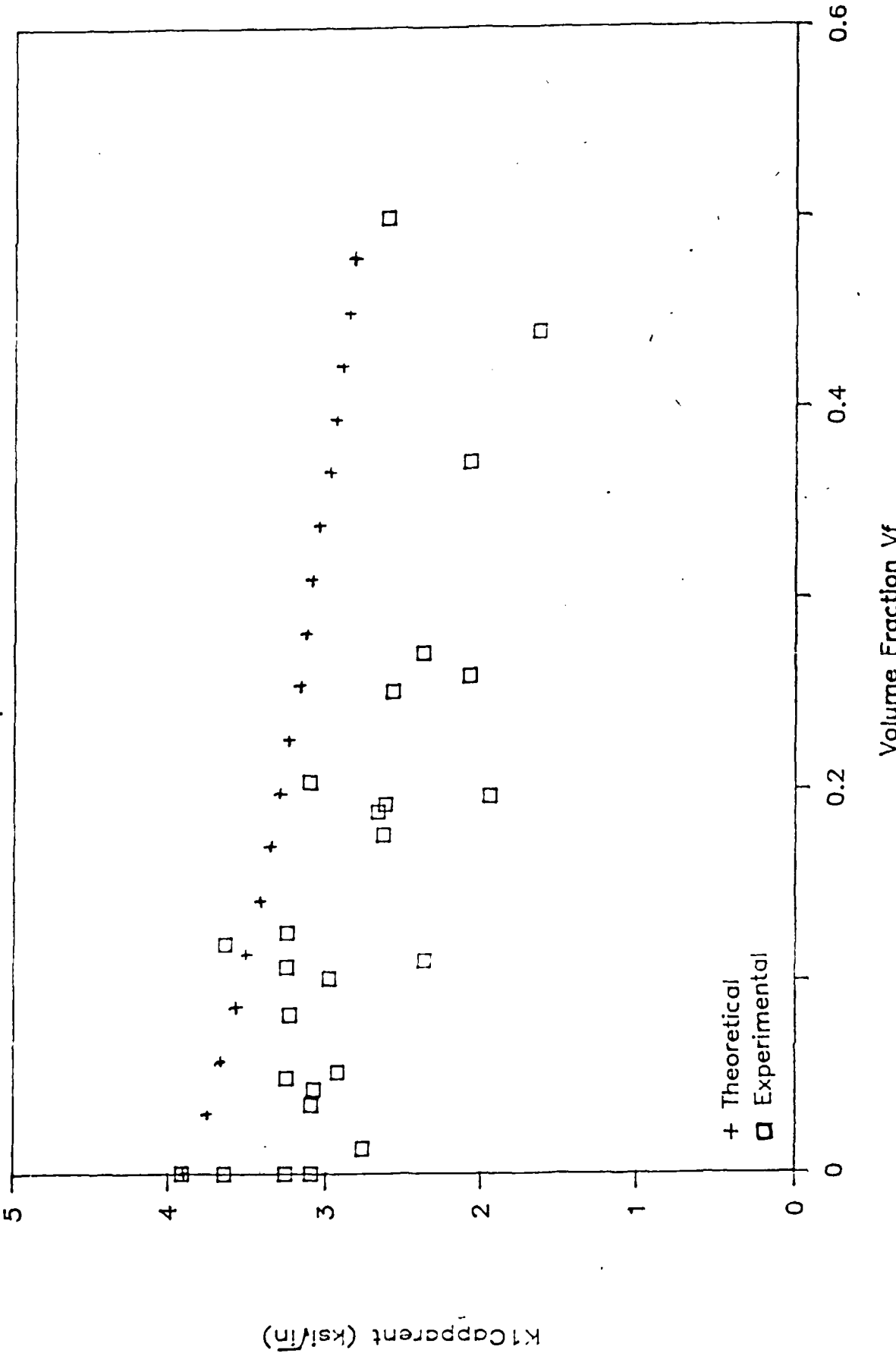


Fig. 53

K_1 APPARENT VS. V_f
TEMPERATURE 800C

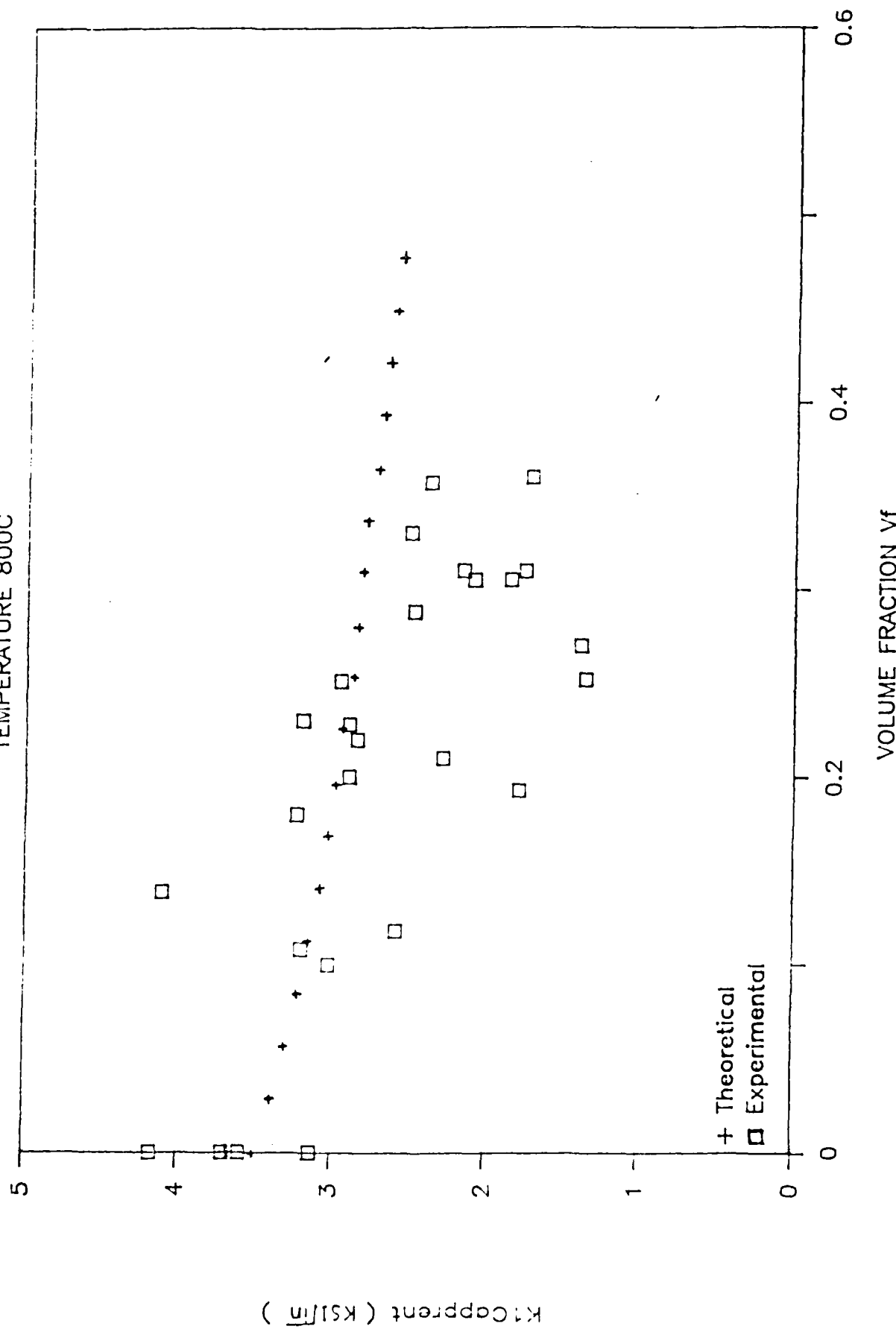


Fig. 54